COMPUTATIONAL ANALYSES OF THE UNSTEADY, THREE DIMENSIONAL MULTIPHASE FLOW IN A LIQUID RING VACUUM PUMP

A Dissertation

Submitted to the Faculty

of

Purdue University

by

Ashutosh Pandey

In Partial Fulfillment of the

Requirements for the Degree

of

Doctor of Philosophy

December 2019

Purdue University

West Lafayette, Indiana

THE PURDUE UNIVERSITY GRADUATE SCHOOL
STATEMENT OF DISSERTATION APPROVAL

Dr. Tom I-P. Shih, Chair

School of Aeronautics and Astronautics

Dr. Alina Alexeenko

School of Aeronautics and Astronautics

Dr. Gregory Blaisdell

School of Aeronautics and Astronautics

Dr. Andrea Vacca

School of Mechanical Engineering

Approved by:

Dr. Tom I-P. Shih, Chair

School of Aeronautics and Astronautics

To my family....

ACKNOWLEDGMENTS

I would like to first express my sincere gratitude to my adviser, Dr. Tom I-P. Shih. His continued support for me and my research throughout my MS and PhD has been invaluable. I would also like to thank my committee members Dr. Alina Alexeenko, Dr. Gregory Blaisdell and Dr. Andrea Vacca for their valuable inputs and insights regarding my work. In addition, I want to thank my lab mates for making my time at Purdue so enjoyable: Chien Shing, Kenny, Irsha, Jay, Sabina, Dominik, James, Yongkai, Wanjia, Adwiteey, and Jason. Lastly, I want to thank my family for their support.

I would also like extend my thanks to Purdue University's Indiana Next Generation Manufacturing Competitiveness Center (IN-MaC) and Dekker Vacuum Technologies, Inc. for the financial support during my doctoral program.

TABLE OF CONTENTS

Page

LIST OF FIGURES

Figure Page

Figure Page

Figure Page

NOMENCLATURE

r_i	impeller radius
r_h	minimum hub radius
e_x	eccentricity in x-direction
e_y	eccentricity in y-direction
r_c	casing radius
s_b	span of the blade
th_b	thickness of the blade
n_b	number of blades
δ	angle between tangents at leading and trailing edge of the blade
ω	rotational speed of the impeller
P_{in}	suction pressure
T_o	Inlet total temperature
TDC	Top dead center
BDC	Bottom dead center

ABSTRACT

Pandey, Ashutosh Ph.D., Purdue University, December 2019. Computational Analyses of the Unsteady, Three Dimensional Multiphase Flow in a Liquid Ring Vacuum Pump. Major Professor: Tom I-P. Shih.

Vacuum is needed in many applications and, there are many types of pumps that can provide the vacuum level needed. One widely used pump is the liquid-ring vacuum pump, which does not involve any solid-solid contacts at interfaces where moving and stationary parts meet. Though liquid-ring vacuum pumps are efficient and robust, manufacturers have aggressive goals on improving efficiency, performance, and range of operations.

In this research, time-accurate computational fluid dynamic (CFD) analyses were performed to study the flow mechanisms in a liquid-ring vacuum pump to understand how it works and how the design can be improved. Based on the understanding gained, a physics based reduced order model was developed for preliminary design of the liquid ring vacuum pumps.

In the CFD analyses, the liquid (water) was modeled as incompressible, the gas (air) as an ideal gas, and turbulence by the shear-stress transport model. The gas-liquid interface was resolved by using the volume-of-fluid method, and rotation of the impeller was enabled by using a sliding mesh. Parameters examined include the suction pressure (75, 300, and 600 Torr) and the impeller's rotational speed (1150, 1450 and 1750 rpm) with the temperature of the gas at the inlet of the suction chamber kept at 300 K and the pressure at the outlet of the exhaust chamber kept at one atmosphere. The CFD solutions generated were verified via a grid sensitivity study and validated by comparing with experimental data. When compared with experiments, results obtained for the flow rate of the gas ingested by the pump had

relative errors less than 6% and results obtained for the power consumed by the pump had relative errors less than 13%.

Results obtained show the shape of the liquid ring to play a dominant role in creating the expansion ratio or the vacuum needed to draw air into the pump through the suction port and the compression ratio needed to expel the air through the discharge ports. Results were generated to show how centrifugal force from rotation and how acceleration/deceleration from the difference in pressure at the pump's inlet and outlet along with the eccentricity of the impeller relative to the pump's housing affect the shape of the liquid ring. Results were also generated to show how the rotational speed of the impeller and the pressure at the suction port affect the nature of the gas and liquid flow in the pump and the pumps effectiveness in creating a vacuum.

With the knowledge gained from the CFD study, a physics-based reduced-order model was developed to predict air ingested and power consumed by the pump as well as the liquid ring shape and pressure of the gas and liquid in the pump as a function of design and operating parameters. This model was developed by recognising and demonstrating that the amount of air ingested and power consumed by the pump is strongly dependent on the shape and location of the liquid ring surface. The flow rates of the gas ingested by the pump and the power consumed by the pump predicted by the model were compared with experimental data and relative errors were less than 12% and 17% respectively.

1. INTRODUCTION

Low pressures are needed in many applications, and these include drying papers in papermaking [1], freeze drying of pharmaceuticals [2], composite plastic moulding [3], ion implantation in semiconductor processing [4], dry etch, physical and chemical vapor deposition in photolithography [5] [6], and uranium enrichment [7] as well as clean rooms [8] and environments with toxic material [9]. There are many types of pumps that can provide the low pressure needed, for example rotary vane [10], piston [11], screw [12] and scroll [13] [14]. These systems all involve solid-solid contacts with lubrication. One widely used pump is the liquid-ring vacuum pump (Fig. 1.1), which does not involve any solid-solid contacts at interfaces where moving and stationary parts meet. Consequently, the lifespan of such pumps increases considerably, and the cost of operation comes down significantly. Though liquid-ring vacuum pumps are efficient and robust, manufacturers have aggressive goals on improving efficiency, performance, and range of operations. One way to achieve this is to understand how design and operating parameters affect the flow physics of liquid ring vacuum pump and using that knowledge to improve design.

Relatively few investigators have studied the unsteady, multidimensional, gas-liquid flow in liquid-ring vacuum pumps, and nearly all are computational. Early attempts focused on modelling and computational issues in simulating liquid-ring vacuum pumps. Grohmann et al. [15], modelled the pump as two dimensional flow device. The computation starts with the impeller being intially positioned at zero eccentricity with respect to the casing to arrive at symmetric ring of water, after which center of impeller was shifted to the required eccentricity. Kakuda et. al. [16], while modelling the pump as two dimensional flow device, adopted a lagrangian approach for water with air being formulated as incompressible. Radle et. al. [17], while performing three-dimensional unsteady flow simulations to study cavitation, modeled

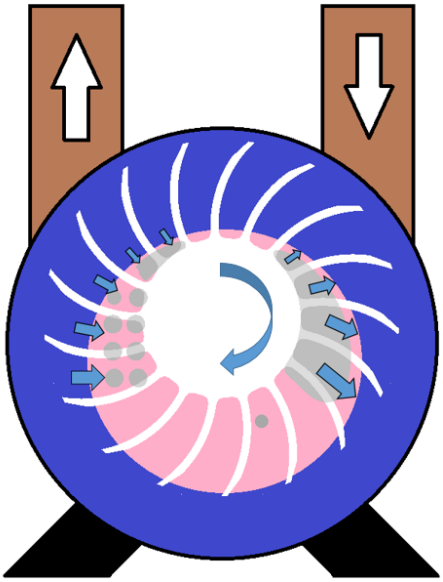

Fig. 1.1. Liquid Ring Vacuum Pump

air as incompressible. Huang et. al. [18] [19] did a three-dimensional simulation with air modeled as compressible. The study provided with an approximation for the liquid ring but did not provide any quantitative comparison with experiments. More recently, Ding et al. [20] performed time-accurate three-dimensional simulations that resolved the air-water interface to study the effects of suction pressure and the rotational speed of the impeller. Their predictions on the volumetric flow rates and power consumption compared well with experimental data. So far, no studies have reported on the flow mechanisms and details of the flow features inside liquid-ring vacuum pumps. Also, to date, no study examined the details of the temperature distribution and heat transfer inside liquid-ring vacuum pumps.

The objective of this study is twofold. The first is to use computational fluid dynamics (CFD) to understand the nature of the flow and heat transfer in a liquid-ring vacuum pump. Of particular interest are as follows:

1. What are the mechanisms that affect how the liquid ring distributes itself in the pump?

2. How design and operating parameters affect the liquid-ring shape?

3. How the liquid ring enables suction, compression, and ejection processes?

4. How heat transfer between the phases affect the suction and compression processes?

The second objective is to use the understanding gained from CFD study to develop a physics based reduced order model to predict the rate of air ingested and power consumed by the pump as a function of design and operating parameters to be used in preliminary design of liquid ring vacuum pumps.

The remainder of the dissertation is organized as follows: First, the liquid ring pump configuration studied is described. Next, its problem formulation for CFD analyses are given. Then, the description of the numerical method of solution employed in the CFD analyses as well as the verification and validation studies. This is followed by the results generated and the physics-based reduced order model developed.

2. PROBLEM DESCRIPTION

The liquid-ring vacuum pump studied is shown in the Fig. 2.1. It consists of a housing; an impeller which is eccentrically mounted in the housing; a port plate that is modelled as infinitely thin; and a suction/exhaust chamber. The port plate connects the suction/exhaust chamber to the housing. It also connects the inlet through which water enters the housing. In addition, the port plate has two sets of openings. One set is a single kidney-shaped hole that serves as the suction port where air from the suction chamber is ingested into the impeller. The other set consists of circular holes and an end collar that serve as the discharge ports where pressurized air is expelled from the impeller to the exhaust chamber.

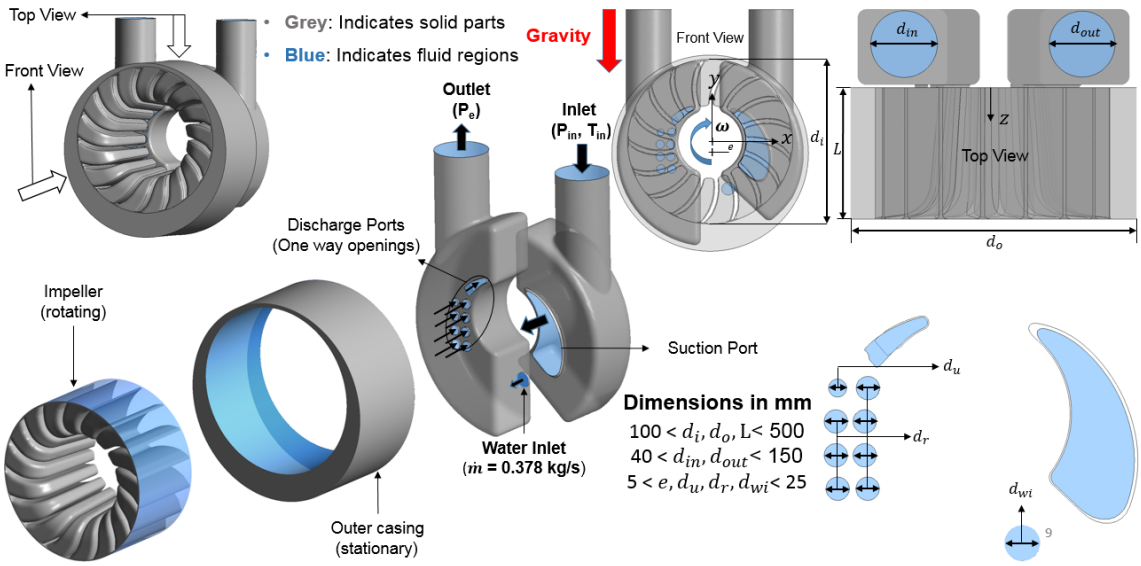

Fig. 2.1. Problem description.

The circular holes for discharge opens only when the pressure on the impeller side is higher than the pressure in the exhaust chamber (i.e., there can be no back flow

from the exhaust chamber into the pump chamber)(see Fig. 2.2). When the holes are closed, it is treated as a wall. On the volumes between successive blades in the impeller, they are sealed by the blades, the hub, the port plate, and the liquid ring that forms next to the housing. In this study, the clearance between the impeller and port plate is not considered so that there is no leakage across the blades. For this pump, it is noted that the eccentricity of the impeller with respect to the housing causes the radial distance from the blade tip to the housing to vary lowest when the blade tip is closest to the housing, referred to as top dead center (TDC) and highest when the blade tip is furthest away, referred to as bottom dead center (BDC).For the pump just described, three rotation speeds of the impeller (ω = 1150, 1450 and 1750 rpm) and three inlet pressures (P_{in} = 75, 300, 600 Torr) were studied. The total temperature at the inlet (T_o) of the pump was kept at 300 K, and the static pressure at the pumps outlet (P_e) was maintained at 760 torr. The gas ingested into the pump is taken to be dry air.

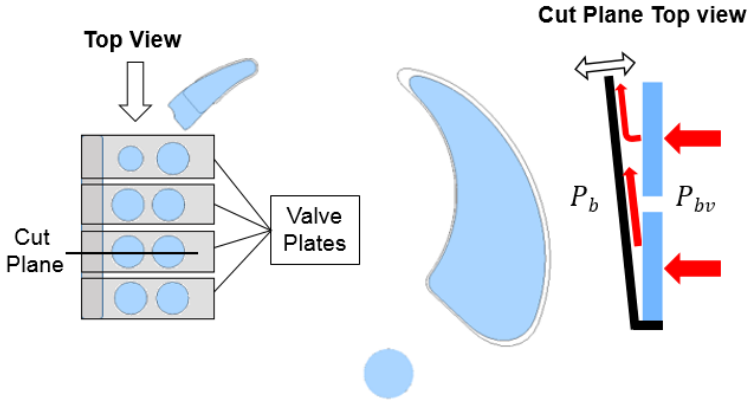

Fig. 2.2. Ports and valves.

The liquid in the pump is water, and its flow rate into the pump is 0.378 Kg/s. The turbulence intensity of the air and water that enter the pump is taken to be 3.07% and turbulent length scale is 0.0049 m. Fig. 2.3 summarizes all the cases studied.

Summary of Cases		
Case #	**P_{in} (Torr)**	**ω (RPM)**
1	600	1750
2	300	1750
3	75	1750
4	300	1450
5	300	1150

Fig. 2.3. Summary of Cases

3. FORMULATION AND NUMERICAL METHOD OF SOLUTION

In the CFD analyses, the flow and heat transfer in the pump with air and water were modeled by the unsteady form of the ensemble averaged continuity, momentum and total energy equations with air taken to be a thermally and calorically perfect gas and water as a constant density fluid. The interface between air and water is modelled by the Volume-of-Fluid (VOF) method. The turbulence is modelled by the Shear Stress Transport (SST) model of Menter [21] with curvature correction, and wall functions were used. The initial conditions for this problem is described later in this section. The boundary conditions employed are as follows. At the suction chamber inlet, the suction pressure (P_{in}) is imposed. At the outlet of the exhaust chamber, a back pressure (P_e) was imposed. At the inlet where water enters the pump, its mass flow rate was imposed. All solid surfaces were modeled as adiabatic and no-slip walls.

Solutions to the aforementioned governing equations and the corresponding initial and boundary conditions were obtained by using ANSYS-Fluent 17.1. Since time-accurate solutions are sought, the PISO scheme is used, and iterations where more than the standard two corrections were implemented to ensure convergence at each time step. On the time differencing, second-order three-point backward implicit scheme was used. On spatial differencing of the convective terms, second-order upwind scheme was used. All diffusion terms were approximated by second order central differencing schemes. The air-water interface was modelled by an implicit VOF scheme [22], where the body forces were treated implicitly. For the volume-fraction equation, required by VOF, the second-order compressive interface capturing scheme was used. Sliding mesh approach was used to transfer data between the rotating and non-rotating parts of the pump. Suction and discharge ports are fluid-fluid interface boundaries through which conservative interface flux interpolation is allowed. The

time-step-size, the number of iteration per time step, and the grid systems used are described in the section on verification.

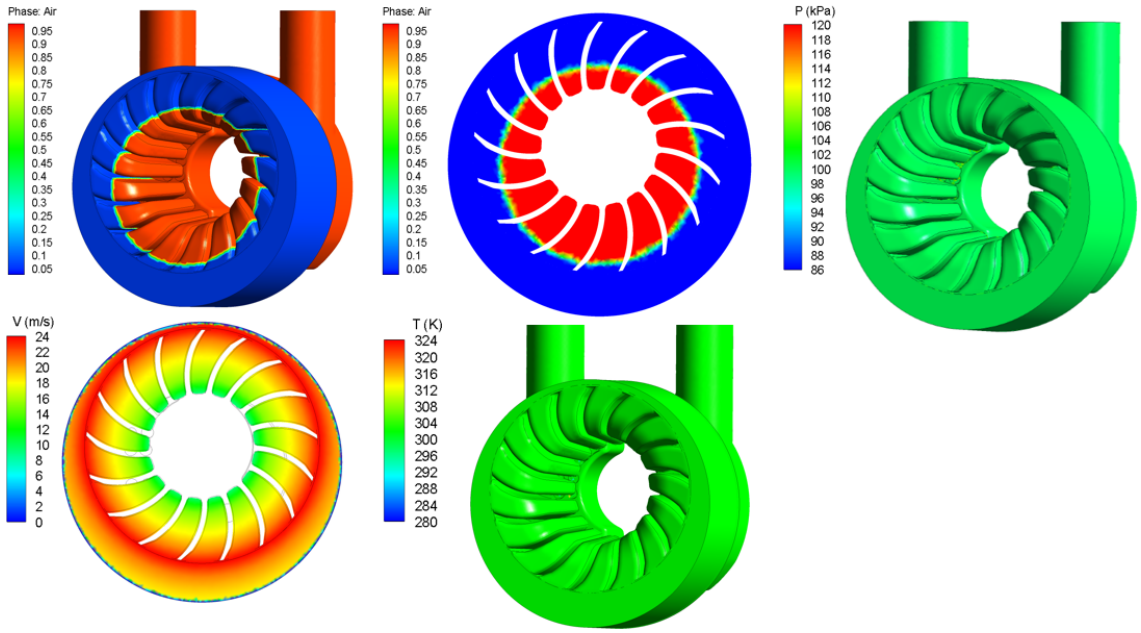

Fig. 3.1. Initial Conditions

Though time-accurate solutions are sought, the interest is in the time-periodic solution, not in the initial transients of the startup of the liquid-ring vacuum pump. Initial conditions strongly affect how quickly the solution can become periodic. The initial condition employed in this study (see Fig. 3.1) is as follows. The water in the housing is initialized as an annular ring with its inner radius determined by the amount of water intended to be in the housing. Under the condition of this study, the intended amount of water in the housing gives rise to an inner radius of 105 mm. The portion of the housing not filled with water is filled with air. For the air and water in the impeller region of the housing, a forced vortex rotating at the pumps operating RPM (ω) was imposed ($V_r = 0$, $V_\theta = \omega r$). At radii outside the impeller, the inviscid free vortex motion was imposed ($V_r = 0$, $V_\theta = \omega r$). Here, V_r and V_θ are the radial (perpendicular to the direction of rotation) and azimuthal (aligned with the direction

of rotation) velocities and r is the radial distance from the axis of rotation of the impeller. The circulation (Γ) of the free vortex was chosen so that the velocity at the location where the forced vortex and the free vortex meet (impellers blade tip which is at radial distance r_i) are the same ($\Gamma=2\pi\omega r_i^2$). The temperature and pressure of the air and water were set at 300 K and 101,325 Pa, respectively. It should be noted that the initial pressure is inconsistent with the initial velocity field and ring shape. However, the solver recovers the pressure distribution consistent with initial velocity field and ring shape within few time steps (see Fig. 3.2).

On the boundary condition at the inlet of the pump, though the desired suction pressure is P_{in}, it is not imposed right away. Instead, a mass flow-rate boundary condition is imposed at the inlet initially. The mass flow rate specified is extremely small (0.001 Kg/s), just large enough to ensure that reverse flow will not take place at the inlet. This mass-flow boundary condition is imposed until the pressure at the inlet boundary the housing near the suction port is 5% below P_{in}. Once that pressure is achieved, the pressure boundary condition is imposed at the inlet with the pressure set to P_{in}. With the aforementioned procedure, periodic solutions are achieved within three to four revolutions.

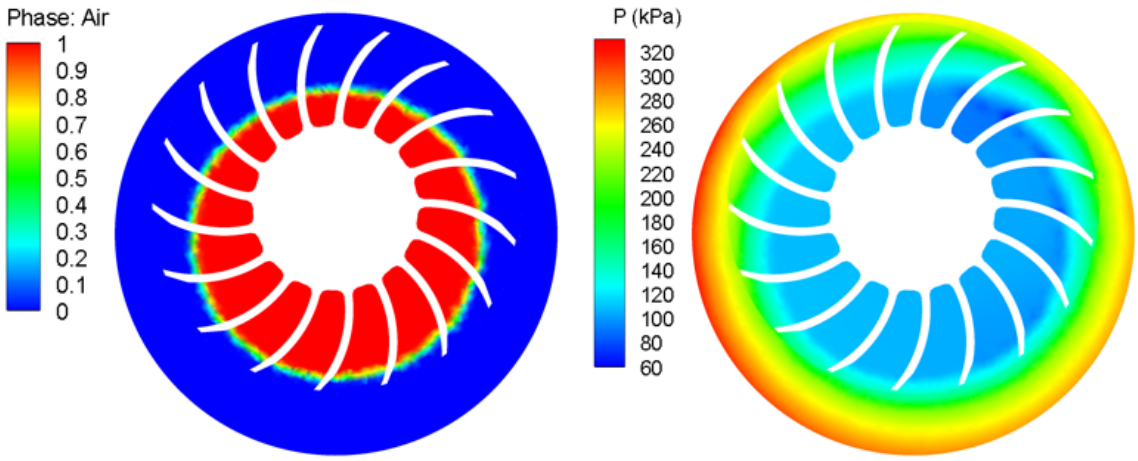

Fig. 3.2. Volume Fraction and Pressure Distribution after 43 time steps

4. RESULTS

In this section, the verification and validation studies performed for the CFD study are first described. Afterwards, the results obtained by the CFD on the nature of the flow and heat transfer are presented and discussed.

4.1 Verification

A representative grid system employed in the CFD study is shown in Fig. 4.1. The grids used between the blades of the impeller and in the outer casing are structured with hexahedral cells, and the grids used in the suction and exhaust chambers are unstructured with tetrahedral cells. To study the effects of the number of cells in the grid system used, results generated by three successively finer grid systems were examined.

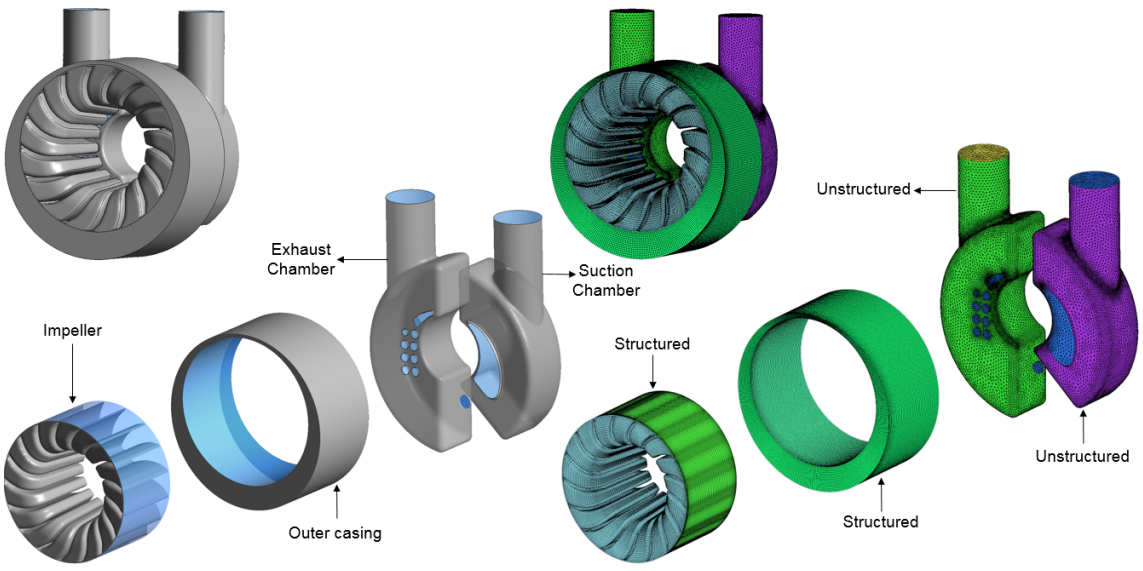

Fig. 4.1. Grid System

The coarsest, the baseline, and finest grid systems have 1.26, 3.42, and 6.7 million cells respectively. The number of cells between two successive blades is 35,416; 75,372; and 154,758 for the three grid systems (see Fig. 4.2). The grid system has cells that get smaller as they get closer to solid surfaces. The y+ of cells next to all solid surfaces is between 35 and 50, which places those cells in the log-law regions of the turbulent boundary layers next to all solid surfaces. Fig. 4.3 shows the baseline grids for the outer casing and suction/exhaust chambers. At the ports, prism layers were generated to resolve suction and discharge processes. To assess the resolution of the three grid systems, the predicted water ring as well as the pressure were compared. From the volume fraction contour, the grid independence was judged based on the location and thickness of the air-water interface. For pressure, values at points inside the domains were compared as the grid is refined. The study was conducted for the case with 300 Torr inlet pressure and operating rotational speed of 1750 rpm. Fig. 4.4 shows the volume fraction for the finest grid. From the figure, it can be seen that the air-water interface is resolved by two cells. Thus, the air-water interface is a region, and its thickness reduces as the grid is refined.

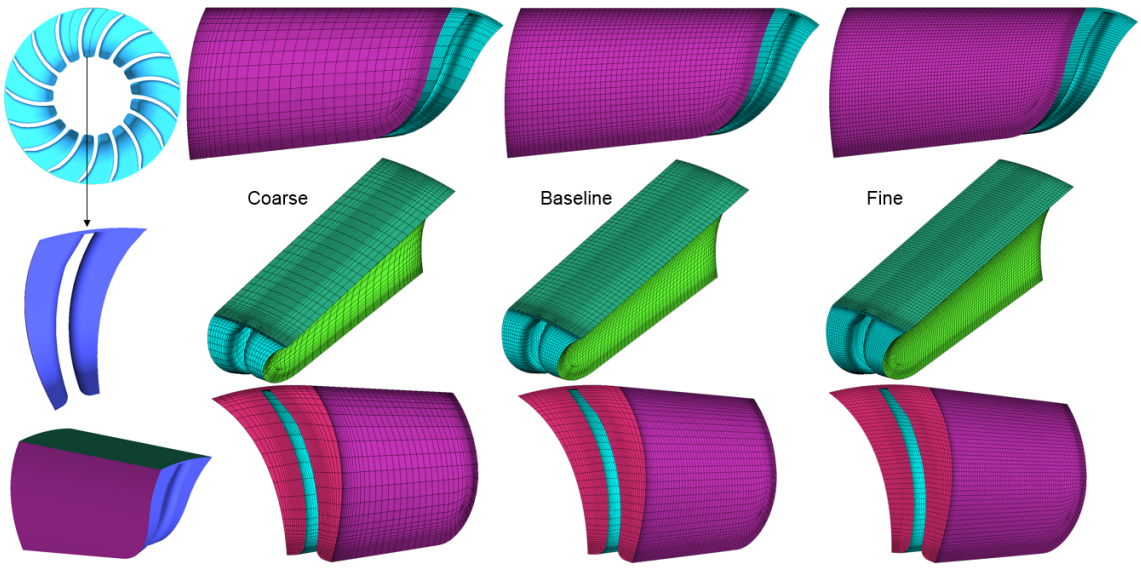

Fig. 4.2. Impeller Sector

From Fig. 4.5, it can be noted that all three grid systems predicted essentially the same water ring shape. The maximum relative difference in that shape (measured from the air surface of the air-water interface region) can be up to 8% for results from the coarsest and finest grids and 2% for results from the baseline and finest grids. The maximum relative difference occurs when the amount of air between two successive blades reaches its minimum. Fig. 4.6 shows the predicted pressure. 34 locations were chosen at the mid plane of the pump chamber to record the pressure data at all instances when they are midway between two successive impeller blades. First 17 points are in the air region and the remaining 17 points are in the water region. Since cell centers may not coincide with those monitor points at the time when pressure is being recorded, tri-linear interpolation is used. The pressure thus recorded was ensemble averaged. The largest relative difference in pressure between baseline and the finest grid within 2%. The maximum relative difference again occurs where there is the least amount of air.

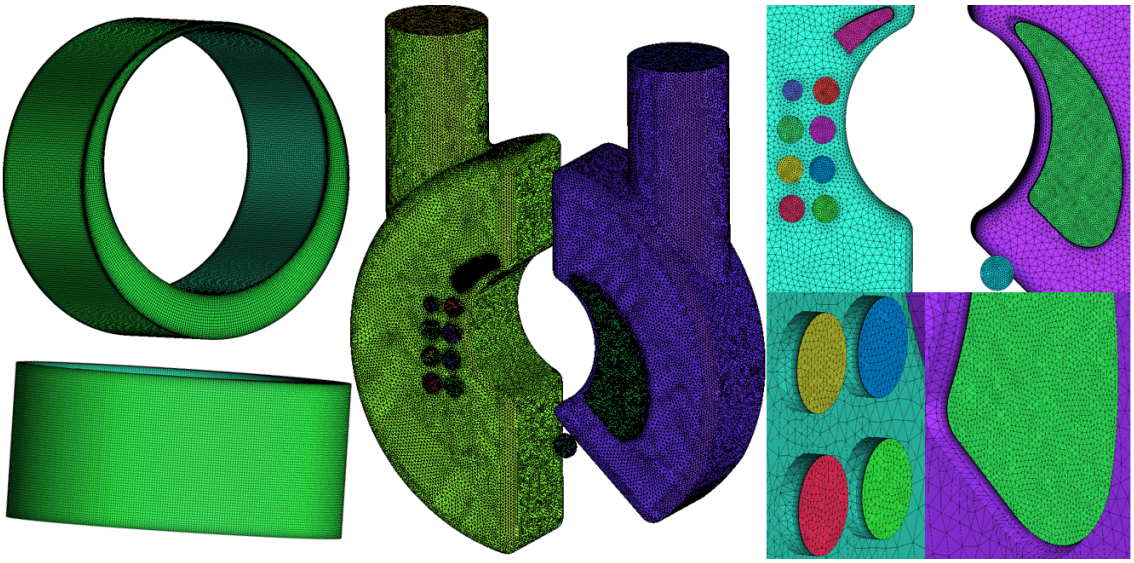

Fig. 4.3. Baseline mesh for Outer Casing and Suction/Exhaust Chamber

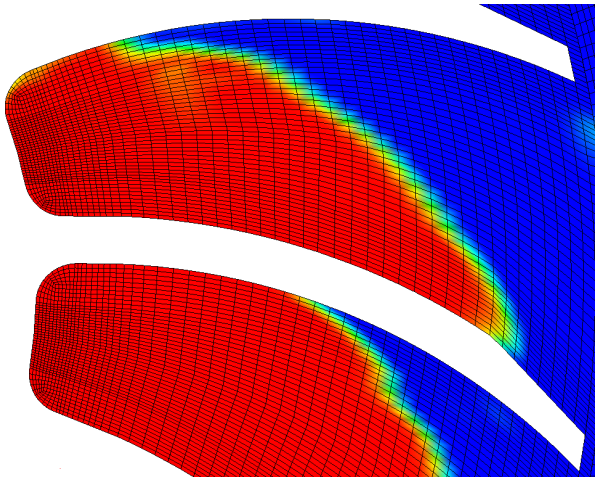

Fig. 4.4. Volume Fraction for the finest grid

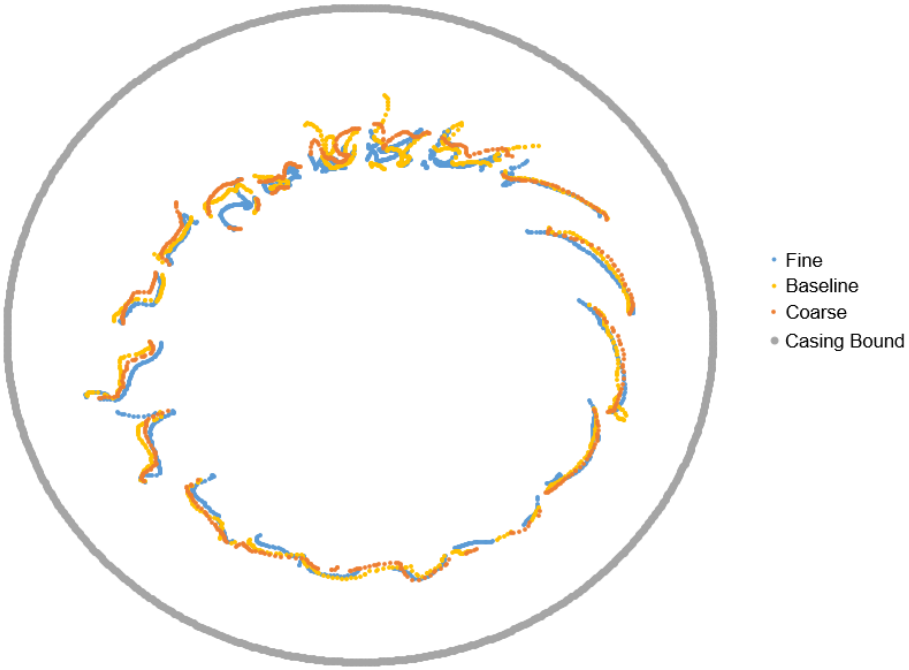

Fig. 4.5. Interface curve for three grids

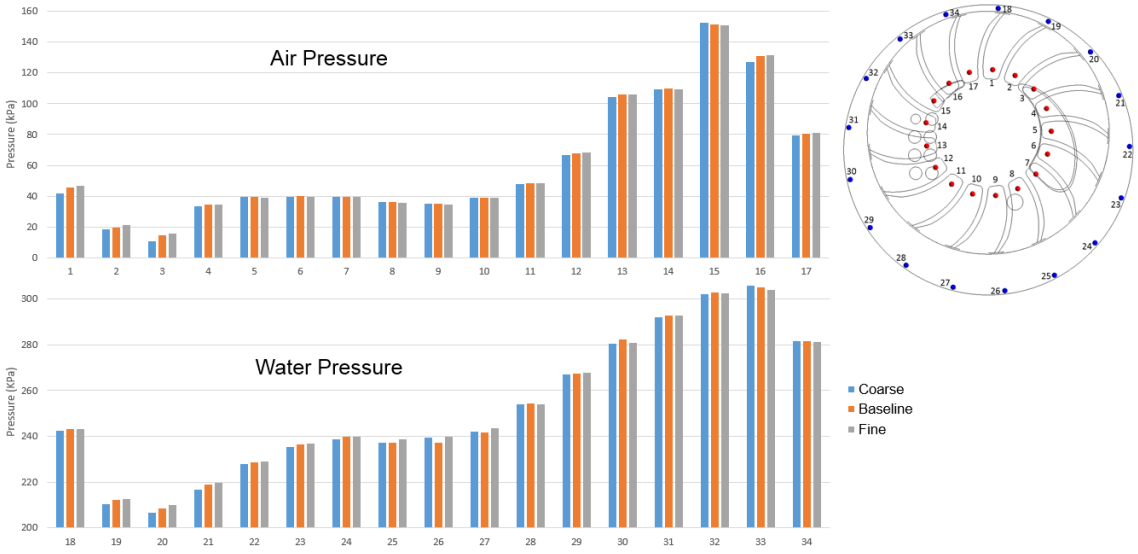

Fig. 4.6. Pressure verification

To ensure that the solutions generated are independent of the time-step size and the number of grids points or cells used, a sensitivity study was performed. The time-step size employed was estimated based on the time scales that are needed to be resolved. For this problem, the time scales that must be resolved from large to small are as follows: period of one revolution of the impeller, the duration of suction process, duration of discharge process through each of the 8 holes and the end collar, and the time scales of the fluid physics such as the shedding of vortices from the impellers blade tips. These time scales are determined by the rotational speed of the impeller as well as the position and size of the suction and discharge ports relative to the impeller. In this study, the following three time-step sizes were employed but stated in terms of degrees of impeller motion per time step so that the rotational speed of the impeller is accounted for: 0.105, 0.0525, and 0.02625 degrees per time step.

For the pump shown in Fig. 2.1 rotating at 1750 rpm, 0.0525 degree per time step corresponds to a time-step size of 5 x 10^{-6} seconds, which results in 6,960 time steps

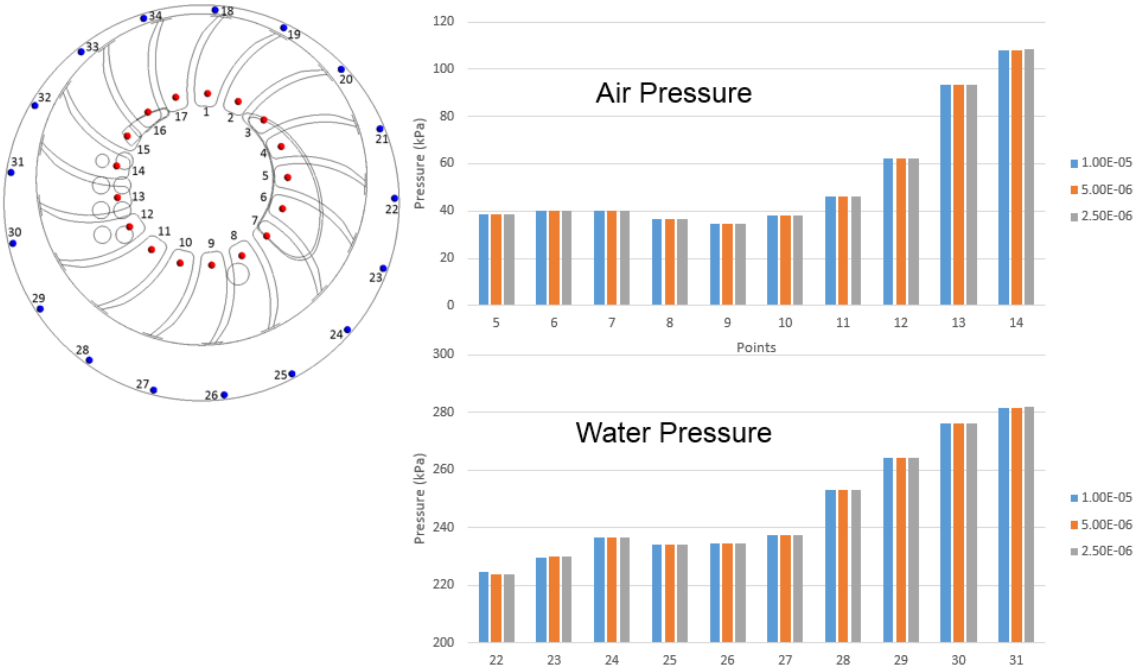

Fig. 4.7. Time step verification

for one revolution, 1,160 time steps to resolve the suction process, and 40 time steps to resolve the discharge through the hole that span the smallest angle measured from the impeller center of rotation. Fig. 4.7 shows the computed pressure at the monitor points after half a blade passing for the three time steps employed. The results of this study show that having a time-step size that produces 0.0525 degree per time step gives results that are within 1% of those obtained by halving the time-step size (i.e., one that produces 0.02625 degree per time step). In addition to the time-step size, the solution at each time step must converge. In this study, the convergence criteria for each time step is the scaled residuals (relative error) which was reduced to the level of 10^{-5} for continuity, 10^{-6} for the momentum, 10^{-9} for energy, 10^{-6} for turbulent kinetic energy equation, 10^{-5} for specific dissipation equation, and 10^{-7} for the volume fraction equation. Typically, 10 iterations per time step were needed.

Since the results from the baseline grid differ those from the finest grid by 5% at most, only results from the baseline grids are used.

4.2 Validation

This CFD study is validated by comparing computed and experimentally measured values of mass flow rates ingested through the suction port and the torque exerted on the pumps impeller. The experimental data include time-averaged measurements of the volumetric flow rate into the pump and the power consumption as a function of suction pressure and rotational speed of the impeller, where power consumption is torque times rotational speed. Fig. 4.8 and 4.9 show a typical time variation of volume-flow rate and power consumption from CFD. Fig. 4.10 shows the computed and measured time-averaged volume-flow rate and power consumption. From these tables, it can be seen that when ω = 1,750 rpm and P_{in} = 300 Torr, CFD over predicts the volume-flow rate by 2.2% and under predicts the power consumption by 3.90%.

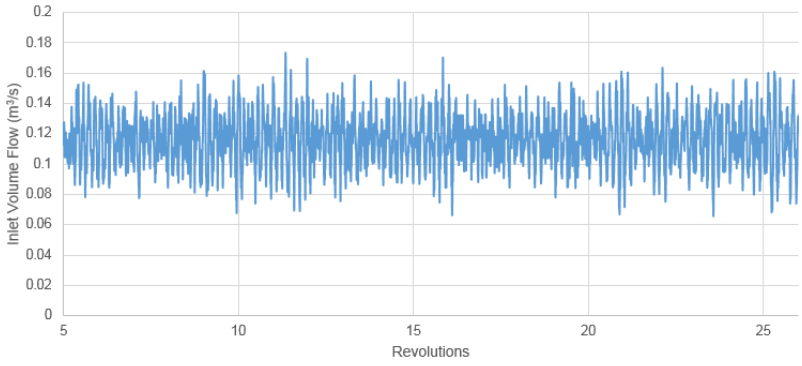

Fig. 4.8. Inlet Volume Flow Rate (Pump Capacity)

When ω = 1450 rpm and P_{in} = 300 Torr, CFD over predicts the volume-flow rate by 2.06% and under predicts the torque and power consumption by 2.81%. The discrepancy in the volume-flow rate can be attributed to inadequacies in the turbulence

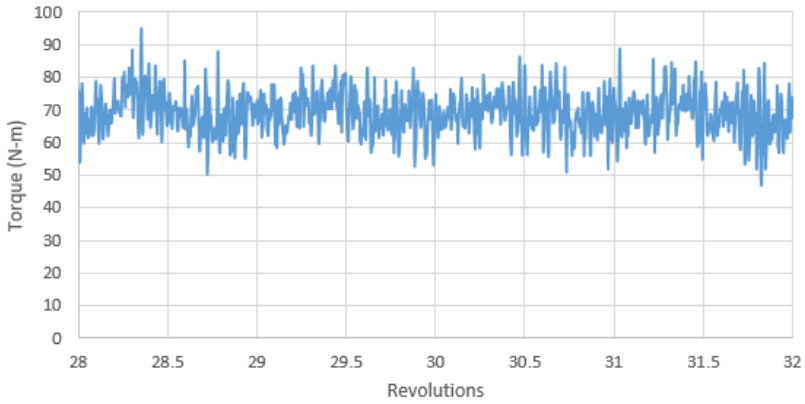

Fig. 4.9. Torque

Inlet Volume Flow Rate – m^3/s				Power Consumption – hp			
Case #	Computed	Measured	Error	Case #	Computed	Measured	Error
1	0.11760	0.12506	5.96%	1	15.819	16.632	4.88%
2	0.11970	0.11806	1.38%	2	17.201	17.905	3.93%
3	0.10614	0.10855	2.22%	3	14.499	16.605	12.68%
4	0.10027	0.09675	3.63%	4	12.819	14.013	8.52%
5	0.08036	-	-	5	8.407	-	-

Fig. 4.10. Comparison of CFD with Experiments

model used and in the modelling of the air-water interface by VOF. The discrepancy in the power consumption can be attributed to losses not accounted for in the CFD study such bearing losses and the torque needed to raise angular speed of the water that is continuously being fed into the pump. These comparisons give some confidence to the CFD method employed to study liquid-ring pumps.

4.3 Nature of Flow Field Induced by Pump

As noted, the objective of this study is to understand the nature of the flow and heat transfer that take place inside liquid-ring vacuum pumps. This section describes the role of the liquid ring and its shape on the suction, compression, and discharge processes and how design parameters affect the shape of the liquid ring. The discussion in this section is based on results from case 2 in Fig. 2.3 (P_{in} = 300 Torr, ω = 1,750 rpm).

4.3.1 Pressure Field

Fig. 4.11 shows the instantaneous flow field pressure, temperature, and the water-air interface in two axial planes (z = 0, L/4; origin on the plane containing suction and discharge port profiles) in the liquid-ring pump. Though instantaneous, it is fairly representative of the qualitative nature of the flow field at other instances of time. From this figure, it can be seen that at any azimuthal coordinate, the pressure increases radially outwards because of centrifugal force from rotation. That increase in pressure is a strong function of density so that the pressure variation in the radial direction is quite significant in the water ring and nearly negligible in the air. The actual magnitude of the pressure in the water and air is dominated by two mechanisms. The first is the pressure of the air about the suction and discharge ports, which are strongly affected by the suction and exhaust pressures (P_{in} and P_e). At azimuthal coordinates about the suction port, the air pressure is near P_{in}. The water's pressure at those coordinates rises in the radial direction due to rotation, and it rises from that air pressure at the air-water interface to some higher pressure at the housing ($P_{S,h}$). At azimuthal coordinates about the discharge ports, the air is near P_e. The water's pressure at those coordinates also rises in the radial direction to some higher pressure at the housing ($P_{D,h}$). Since the $P_e \gg P_{in}$, $P_{D,h} \gg P_{S,h}$. Thus, there is a favorable pressure gradient in the water ring from discharge ports to the

suction port, and an adverse pressure gradient from the suction port to the discharge ports.

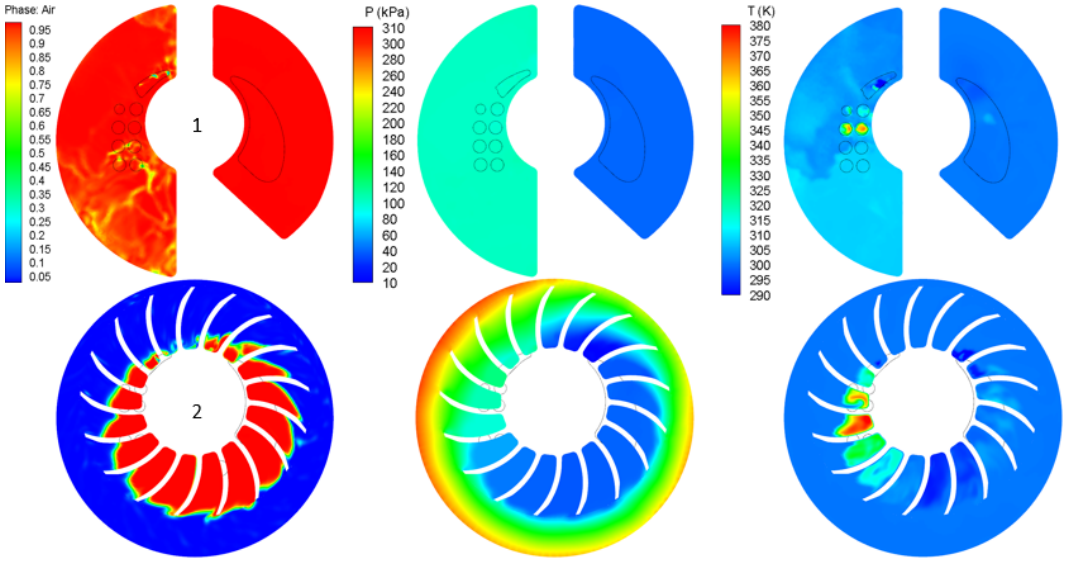

Fig. 4.11. Volume Fraction, Pressure, Temperature for P_{in}=300 Torr, ω=1750 RPM

In regions with a favorable pressure gradient, water speeds up so the water ring gets thinner to maintain continuity. In regions, with an adverse pressure gradient, water slows down so the water ring gets thicker to maintain continuity. This is one reason why the water ring is thinnest about the suction port and thickest about the discharge ports. The second mechanism that affect the pressure magnitude is the volume change between impeller blades and housing due to eccentricity. Because of the eccentricity, the total volume between the blades and the housing wall decreases after BDC, causing water to enter the region between the blades.

Similarly, because of eccentricity, the total volume between the blades and the housing wall increases after TDC, causing water to move radially out of the region between the blades because of centrifugal force from rotation. Thus, this is second reason why the liquid ring is thickest about the discharge ports and thinnest about

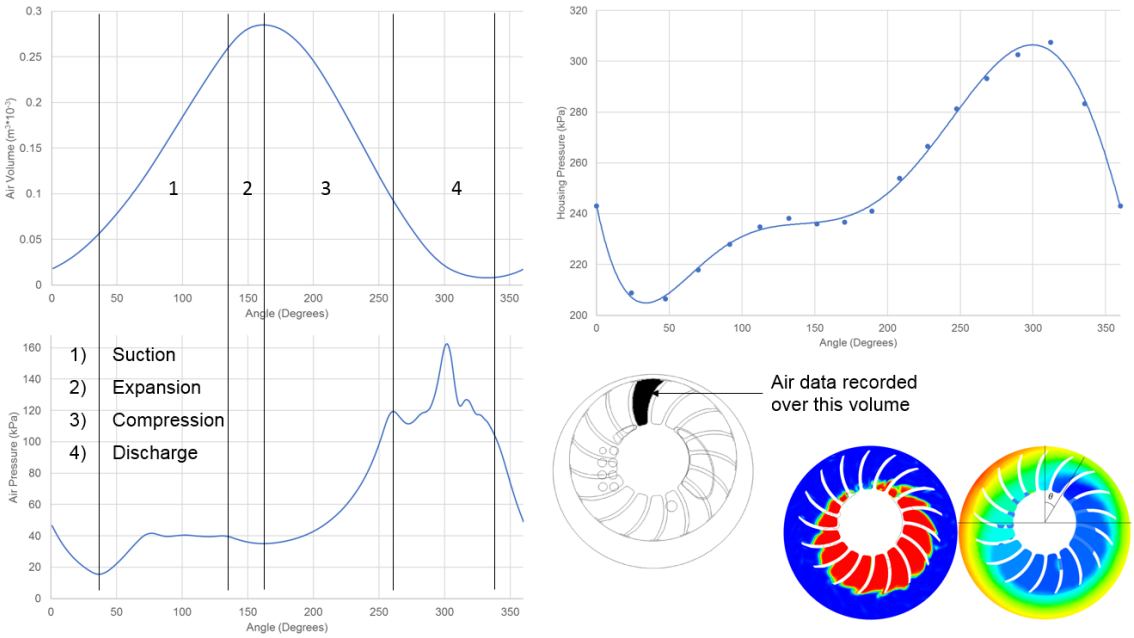

Fig. 4.12. Time averaged Volume and Pressure of Air between the Blades and Housing Pressure vs. rotor angle

the suction port. The thickening of the liquid ring causes the water to enter the region between the blades. This is the mechanism that compresses the ingested air.

4.3.2 Mechanisms driving ingestion, compression and discharge

The mechanisms by which the pump ingest, compress, and discharge air will be explained by starting with blades of the rotor at the BDC. At BDC, compression of the air between the blades starts. Compression occurs because of two reasons. First, the volume between the blades and the housing wall decreases after BDC. This causes the water to move into the region between the blades, which compresses the air. Second, there is an adverse pressure gradient from the suction port to the discharge ports.

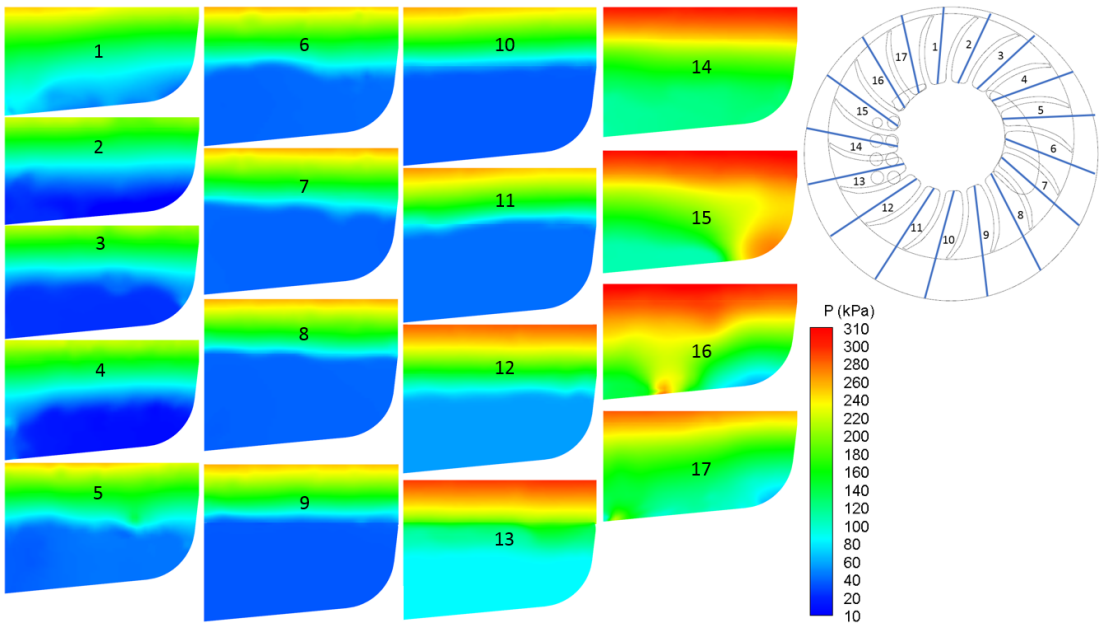

Fig. 4.13. Pressure on the given planes

This adverse pressure gradient decelerates the flow of the water, so continuity causes more water to move into the region between the blades, causing additional compression of the air. The compression continues as the impeller rotates until exposed to the first opened discharge port. Once the discharge ports open, air between the blades discharges into the exhaust chamber. During discharge, the volume occupied by air decreases steadily. Once the impeller blade passes by the last discharge port, typically just upstream of TDC, the discharge ends. Once discharge ends, the volume occupied by air starts to increase. This volume increases because the volume between the blades and the housing wall increases after TDC and there is a favorable pressure gradient from discharge ports to the suction port. This favorable pressure gradient accelerates the flow of the water, so continuity and centrifugal force cause the water to move out of the region between the blades to create more volume for the air. Thus, the pressure of the air in the region between the blades keeps dropping as the impeller rotates until the suction port opens. Once the suction port opens, two scenarios are possible, depending upon the pressure of the air between the blades just

before the suction port opens, denoted as $P_{S,i}$, and the pressure of the suction port, P_S (P_S is slightly below P_{in} because of losses in the suction chamber and increases in the flow velocity near the suction port). If $P_{S,i}$ is less than P_S, then suction starts right away. As impeller rotates, the volume available for air increases till BDC even though there is an adverse pressure gradient from the suction port to the discharge ports. This increase in the volume available for air causes air to be ingested into the region between the blades throughout the suction process. If $P_{S,i}$ is greater than P_S, then air discharges from the region between the blades into the suction chamber. Ingestion into the pump does not take place until the pressure of the air in the region between blades drops below P_S. Ingestion stops when the suction port closes. Once back at BDC, compression starts and the cycle repeats.

4.3.3 Pressure distribution of ingested air

In this section, the pressure distribution of the air in the liquid-ring vacuum pump as the impeller rotates is explained. Fig. 4.12 shows the time-average pressure of the air between the blades of the rotating impeller and on the housing wall. From this figure along with Fig. 4.11, it can be seen that in the latter portion of suction process (θ 70°), the pressure of the air between the blades is nearly constant and only slightly below Pin. The pressure variations in the earlier portion of the suction process is because the pressure in the air, $P_{S,i}$, just before the suction port opens may not equal to P_S. From the end of suction to BDC, the air experiences a slight expansion resulting in a small drop in pressure (the maximum relative difference in this drop is about 4%). From BDC to just before any of the discharge ports open, the pressure rises so the ingested air is compressed. From the first open discharge ports to the last, the air is ejected into the exhaust chamber, and its ejection rate depends on how many holes are open. If more holes are open, then the pressure of the air between the blades drops quickly in time. However, if too few holes are open, then the pressure of the air between the blades could actually increase in time. That

is the reason for the pressure oscillations seen in Figure 4.12 between $\theta = 260^{o}$ and 345^{o}. Once all discharge ports are closed to just before the suction port opens, the volume between the blades for the air increases, and this causes the pressure of the air to decrease from $P_{D,i}$ (pressure in the residual air just after the last discharge port closes) to $P_{S,i}$. When the suction port does open, it is noted that P_S may not equal to P_{in}. This explains the pressure variations in the early portion of the suction process. Fig. 4.13 shows the pressure at several planes. From this figure, it can be noted that the pressure varies primarily in the radial direction and is dominated by the location of the air-water interface. During discharge, water pushes the air out into the exhaust chamber and fills the space created by the discharged air. The filling-in of the water into lower radial locations further increased the pressure in the radial direction because of centrifugal force, which reinforces the discharge of the air. Since the radial position of the air-water interface is now a function of the axial coordinate, the pressure varies radially and axially. The pressure variation in the axial direction is less during the ingestion process because water moves towards the housing during that process. At this point, it is noted that there can be pockets of air embedded/trapped in the water as the air discharges. Depending upon how these air pockets are compressed by the water due to water's dynamic pressure, the pressure in these air pockets could increase.

4.3.4 Flow pattern of water and air

Fig. 4.14 to 4.19 show the flow patterns of the water and air in the pump. Fig. 4.14 shows the absolute and relative velocity of water and air with respect to the impeller in the form of streamlines in the r-θ plane at z = L/2. Fig. 4.16 shows the relative velocity of water and air with respect to the impeller in the form of streamlines colored with temperature at 17 planes. Fig. 4.17 shows the absolute velocity of the air in the form of streamlines in the suction and exhaust chambers. From Figure 4.14, it can be noted that circulations created by the flow physics in the r-θ planes do not

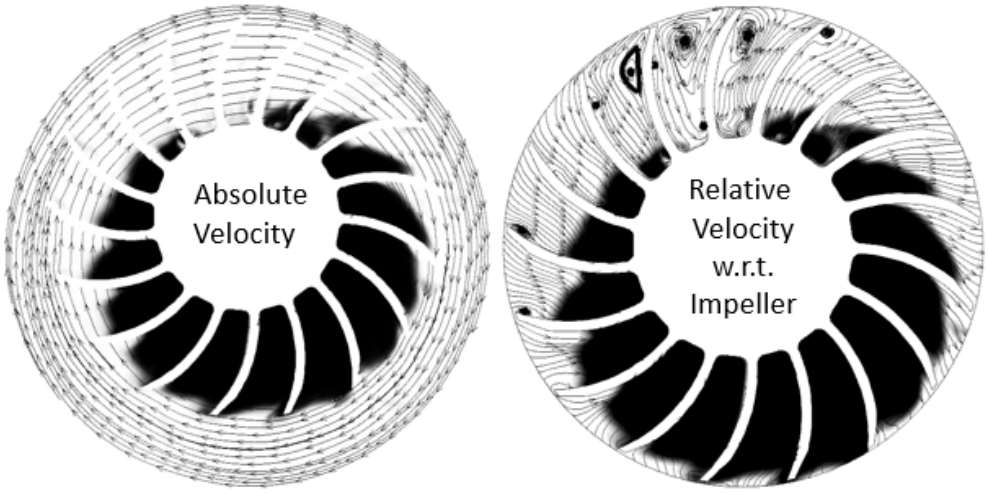

Fig. 4.14. Absolute and relative velocity streamlines(left and right); volume fraction in background (black fill-air; white-water)

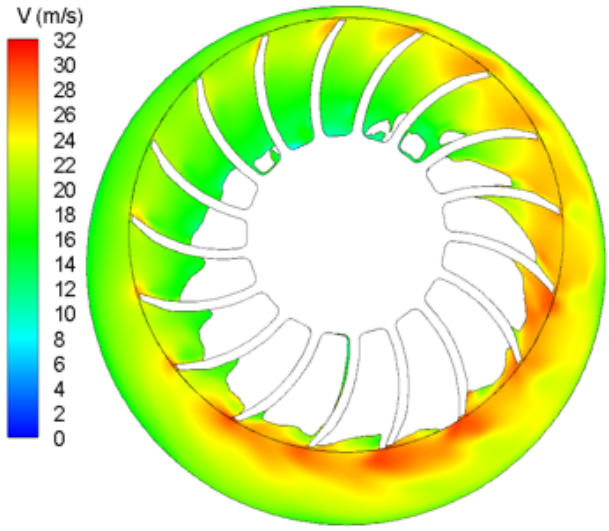

Fig. 4.15. Velocity magnitude in the water region

produce recirculating flows in the absolute frame and can only be seen in coordinate systems that move with the impeller. For the water, the recirculating flow observed in the frame relative to the impeller is due to changes in the direction of water flow in the radial direction. During compression, which occurs from BDC till end

of discharge, water generally flows radially inwards because of the adverse pressure gradient and because of eccentricity. However, once all discharge ports close, the favorable pressure gradient plus the opposite effect of eccentricity causes the water to flow radially outwards. On the air flow, Fig. 4.17 shows uniform flow entering the pipe that leads to the suction chamber. Once entering the suction chamber, the flow separates because of the sudden change in the geometry. The separation created a large toroidal vortical structure. When air enters the region between the blades through the suction port, additional vortical structures form because of two reasons. The first is flow separation at the edge of the suction port. The second is due to jet impingement on the impeller wall. These vortical structures can be seen in Fig. 4.16.

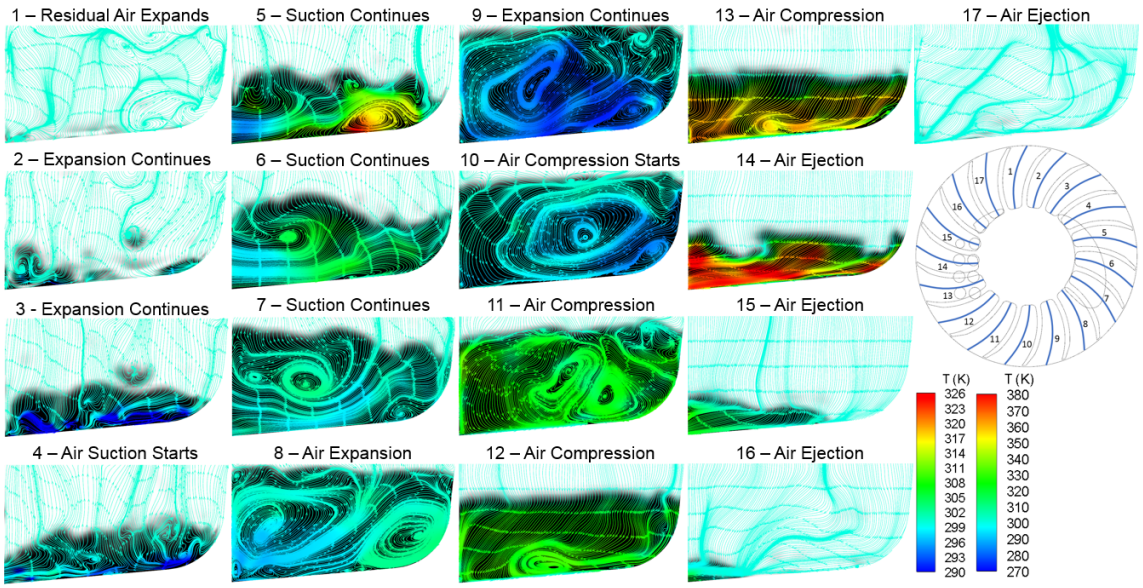

Fig. 4.16. Streamlines colored wit h temperature at given planes with volume fraction in background (black-air; white-water) Plane 1-11 follow legend on the left, Plane 12-17 follow legend on the right

When air enters the region between the blades through the suction port, the vortex formed due to flow separation is small at the start of ingestion. As the air volume increases, the size of this vortex increases till $\theta = 90^{o}$. From $\theta = 90^{o}$ till the end of suction, the size of this vortex remains almost constant. This is because this vortex is

confined between the air-water interface and the incoming air flow that is entering the region between the blades through suction port. In the last stages of suction, some smaller vortices are generated due to flow separation. As soon as the suction stops, this vortex entrains itself completely in the region between the blades causing its size to increase. This is because the incoming air is no longer confining this vortex. When the flow entry ceases, the region between the blades is left with significant recirculating flow. As the impeller progresses, the entrapped air experiences a small amount of volume increase resulting in a small increase in the size of this vortex. When the air starts to get compressed, this vortex decreases in size.

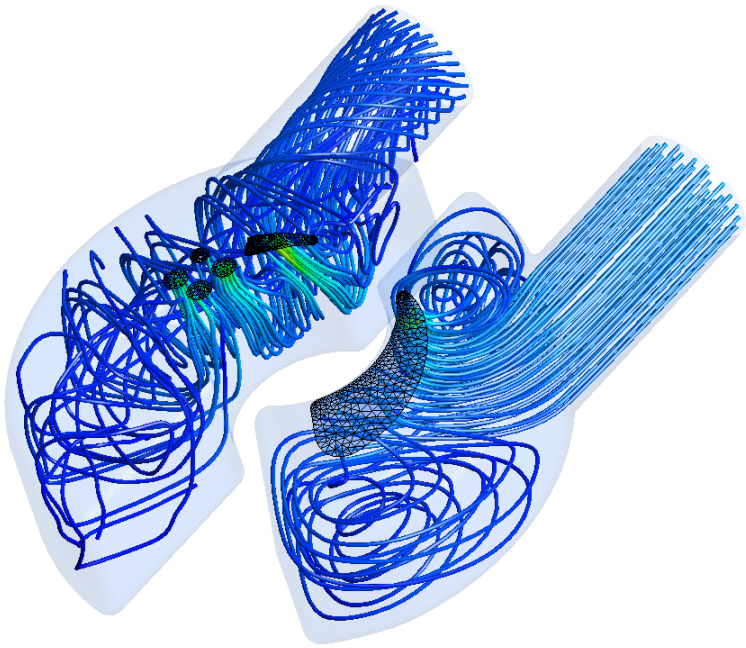

Fig. 4.17. Streamlines in suction (right) and exhaust (left) chambers

This is because volume available for the mixing gets reduced when air gets compressed. In the last stages of compression, the recirculating flow is confined to a very small region near the hub. When the discharge ports open, compression stops, and air gets ejected out of the region between the blades into the exhaust chamber. The ejection of air into the exhaust chamber also gives rise to an interesting flow pattern.

From the Fig. 4.18 and 4.19, it can be observed that the air ejection is almost axial to the impeller. When the air ejects out of the region between the blades into the exhaust chamber, it expands due to the sudden change in available volume which accelerates the flow considerably (see Fig. 4.20). This high-speed jet while coming out, decelerates due to presence of wall downstream. As the jet progresses, it impinges on back wall of exhaust chamber causing it to turn by 90° (see Fig. 4.19). The flow turning is repeated two more times resulting in an impingement of this circulating flow into the jet coming out of the region between the blades. This impingement pushes the jet coming out of the region between the blades slightly away from the axial line. This also results in turning of the impinged flow. Combined, these give rise to a tornado like flow pattern in the exhaust chamber (see Fig. 4.17).

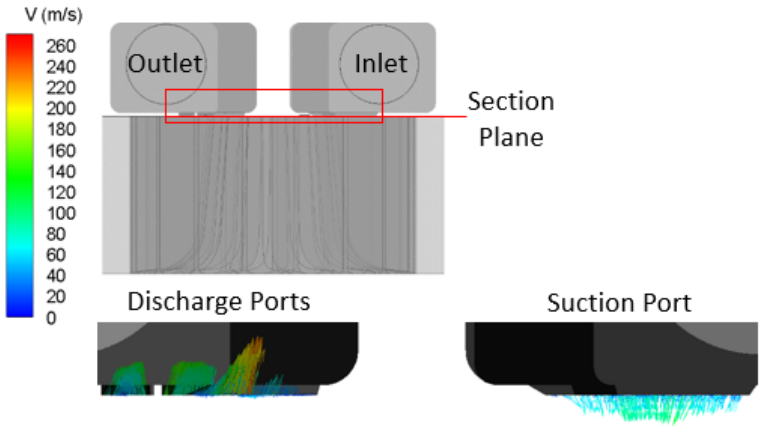

Fig. 4.18. Velocity vectors at suction and discharge ports

Evolution of Air Temperature

By examining the temperature in Fig. 4.11, it can be seen that ingestion of air between blades as the impeller sweeps across the suction port is nearly an isothermal process. From the time the suction port closes to BDC, the air experiences a slight expansion causing the temperature and density to drop. From BDC to the first set

of open discharge ports, the air experiences compression, so the temperature rises. During the compression process, the polytropic index of compression was found to be 1.2, which is not isentropic. The deviation from isentropic compression is because of heat transfer from air to water. During the discharge process, the temperature of the air decreases steadily due to ejection of air into the exhaust chamber. Once all discharge port closes, expansion starts, and its polytropic index was found to be 1.1. The deviation from isentropic expansion is again because of heat transfer, but this time it is from water to air, and it is lower than the compression index by 0.1 because of the higher surface-to-volume ratio available for heat transfer. From the first set of discharge ports till end of discharge, the temperature of air drops gradually due to ejection of air into exhaust chamber. Fig. 4.16 shows the variation of temperature along with streamlines projected in 17 planes. From this figure, it can be seen that at the end of the discharge process (plane 1), there is still some air left between the blades albeit a very small amount ($\leq$5%). This air experiences expansion once all discharge ports close because of the favorable pressure gradient in the water ring (Fig. 4.12). The temperature non-uniformities can be seen to occur in Fig. 4.16 about the suction port during ingestion, about the air-water interfaces during compression, throughout the core between the blades during exhaust, and about the impeller hub during expansion. These non-uniformities at the air-water interfaces are expected because that is where considerable heat transfer takes place. The non-uniformities in the core is because cooled air from the air-water interface gets convected there by different vortical structures.

Once the impeller blades reach the suction port, the air between the blades at pressure, $P_{S,i}$, is suddenly exposed to the pressure at the suction chamber, P_{in}. If $P_{S,i}$ is less than P_{in}, then air is immediately ingested into the region between the blades (plane 4). Typically, P_{in} is much larger than $P_{S,i}$, so that the ingestion process involves a high-speed jet entering into the region between the blades (planes 4 and 5). Because the air ingested from the suction chamber at temperature T_{in} and pressure P_{in} were greatly accelerated, the temperature and pressure of the ingested jet is considerably

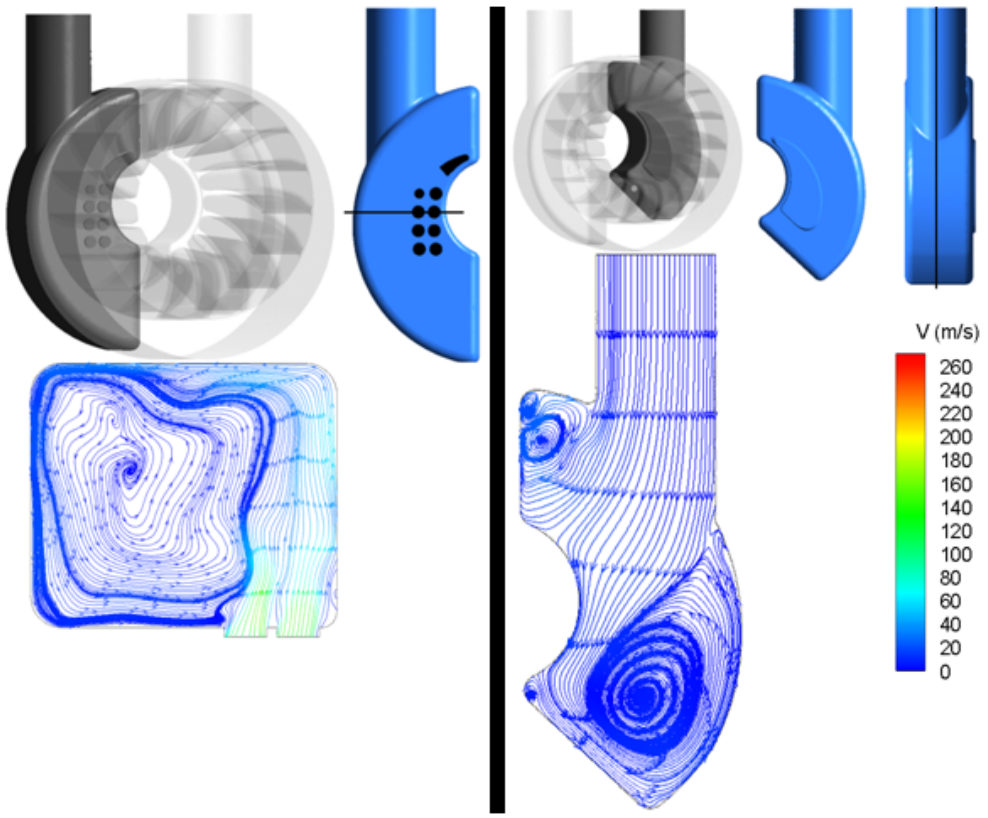

Fig. 4.19. Projected streamlines at a cut plane in suction (right) and exhaust (left) chambers

lower than T_{in} and P_{in}. During the discharge process, the velocity of the jet exiting the region between blades is also very high. Thus, the pressure and temperature in the jet region is considerably lower than pressure and temperature in the region between the blades just before discharge port opens. From the Fig. 4.16 (planes 11 to 13), it can be seen that there is a low temperature film near the hub. This is due to the water injected into the region between the blades through the water inlet. This injected water eventually flows to join the water ring that surrounds the impeller.

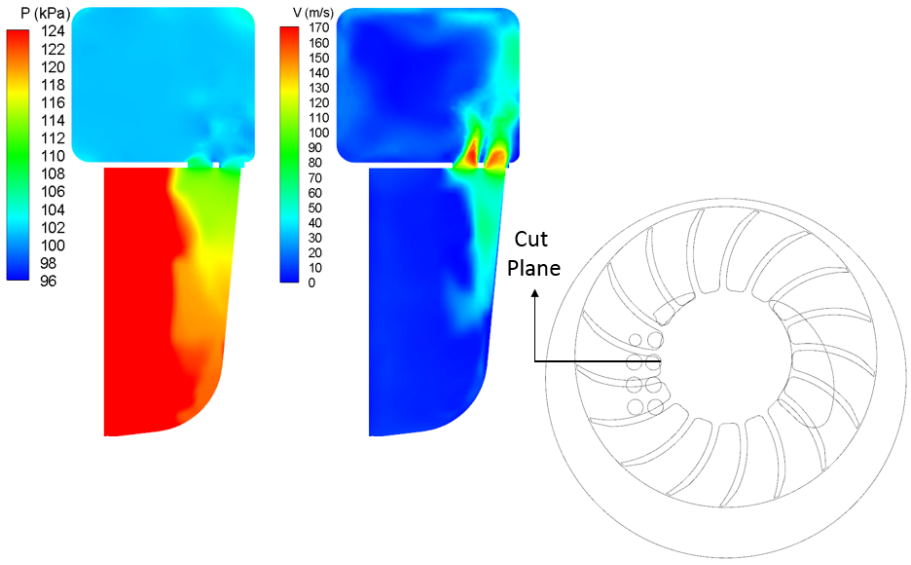

Fig. 4.20. Velocity and Pressure at a cut plane on the discharge side

4.4 Effects of Suction Pressure

In this section, the effect of the operating parameter, suction pressure (P_{in}) on the nature of flow in the liquid ring vacuum pump is discussed.

4.4.1 Ring Structure and Pressure distribution

Fig. 4.21 and 4.22 show how changes in the suction pressure (P_{in} = 600, 300, and 75 Torr) for a given exhaust pressure (P_e = 1 atm) and rotational speed (ω = 1750 rpm) affect the water-ring shape and the pressure distribution in the water ring and the ingested air. From Fig. 4.21, it can be seen that the water-ring shape changes when the shape of the water-air interface changes. The water-air interface is approximately elliptical with its major axis nearly vertical when P_{in} = 600 Torr, circular when P_{in} drops to 300 Torr, and elliptical again except with its major axis nearly horizontal when P_{in} drops further to 75 Torr. These changes occur because a decrease in P_{in} for a given P_e increases the pressure gradient from the discharge ports

to the suction port, which increases the acceleration of the water flow in the region between the blade tips and the housing. This increase in acceleration increases the velocity of the water there, which causes water in the region between the blades to get pulled into the region between the blade tips and housing to satisfy continuity. Thus, the volume between the blades available for air increases, and the air expands, and pressure drops. The increase in the adverse pressure gradient from the suction port to the discharge ports has the opposite effect because it increases the deceleration of water flow in the region between the blade tips and the housing. This deceleration slows the velocity there, which causes water in the liquid ring to enter into the region between the blades to satisfy continuity. With water entering into the region between the blades, the volume between the blades available for air decreases so air compresses and pressure rises.

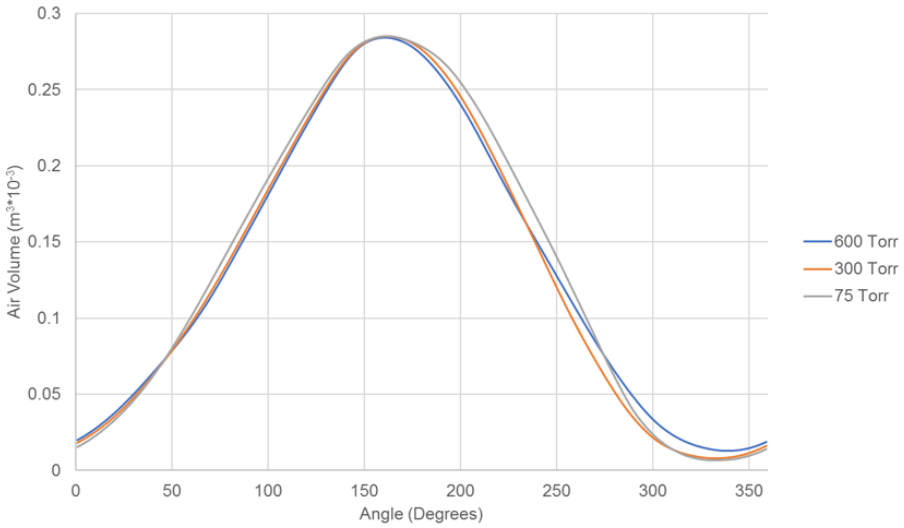

Fig. 4.21. Air volume in a region between the blades with angular coordinate (similar to Fig. 5.12) for P_{in}=600, 300, 75 Torr for ω=1750 RPM

To understand the pressure distribution for different P_{in}, it is important to note that the discharge ports will not open until the pressure of the air between the blades is higher than P_e though the end-collar is always open. Thus, though the pressure of

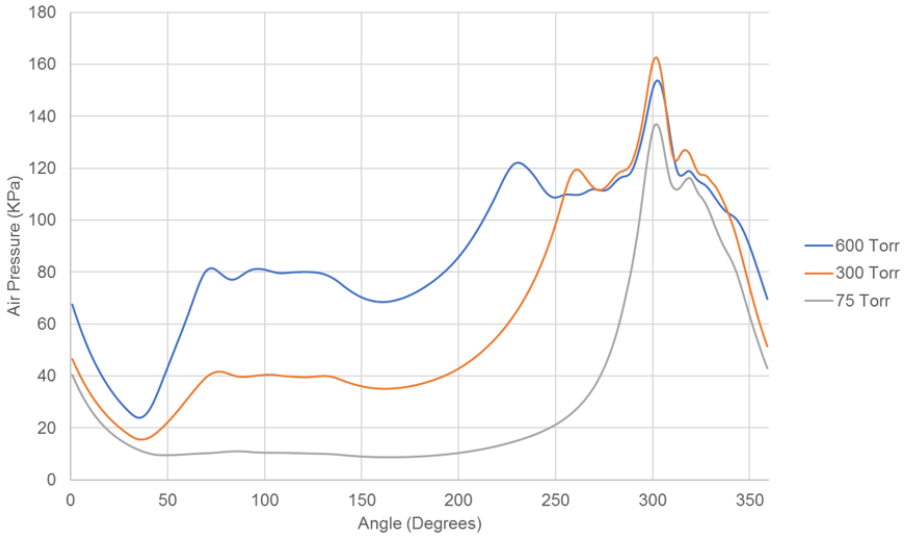

Fig. 4.22. Volume averaged air pressure in a region between the blades with angular coordinate (similar to Fig. 5.12) for P_{in}=600, 300, 75 Torr for ω=1750 RPM

the ingested air at the start of compression process is lower if P_{in} is lower, compression continues until its pressure exceeds P_e. Results obtained for this pump configuration show that discharge ports do not open until $\theta = 230^o$, 260^o, and 300^o, which corresponds to P_{in} = 600, 300, and 75 Torr, respectively (see Fig. 4.25). Since $\theta = 230^o$ is the earliest possible θ for any discharge port to open, all discharge ports are open when P_{in} = 600 Torr. For P_{in} = 300 Torr, the discharge ports open at $\theta = 260^o$. When P_{in} = 600 and 300 Torr, the flow through all opened discharge ports is always from the region between the blades to the exhaust chamber. Reverse flow never takes place. When P_{in} = 75 Torr, all circular discharge ports were never opened because the pressure of the air is still below P_e. However, when $\theta = 300^o$, the end-collar opens irrespective of whether the pressure of the air between the blades is higher or lower than P_e. When P_{in} = 75 Torr, the pressure of the air between the blades is less than P_e when it first reaches the end-collar. Thus, flow enters from the exhaust chamber into the region between the blades (see Fig. 4.23). Discharge does not occur until the pressure of the air between the blades exceed P_e, which occurs at approximately

$\theta = 312^{o}$. Thus, even at $P_{in} = 75$ Torr, the pump configuration at 1750 rpm can still ingest and expel air. One more observation is that as P_{in} decreases, the highest pressure in the pump, which occurs on the housing about the end-collar, decreases, and this is expected since compression of the ingested air started at a lower pressure. At the suction port, it always opens at $\theta = 35^{o}$ whether the pressure of the air between the blades ($P_{S,i}$) is higher or lower than Pin. For the pump studied, $P_{S,i}$ is always less than Pin when $P_{in} = 600$ and 300 Torr so that air always enters into the region between the blades; i.e., there is never any reverse flow at the suction port. When $P_{in} = 75$ Torr, $P_{S,i}$ is higher than P_e when it first reaches the suction port. Thus, air exits from the region between the blades into the suction chamber, which reduces the performance of the pump (see Fig. 4.23 and 4.24). Ingestion does not take place until $\theta = 55^{o}$ when $P_{S,i}$ starts to get lower than P_{in}. One way to address this problem is to delay the θ at which the suction port opens.

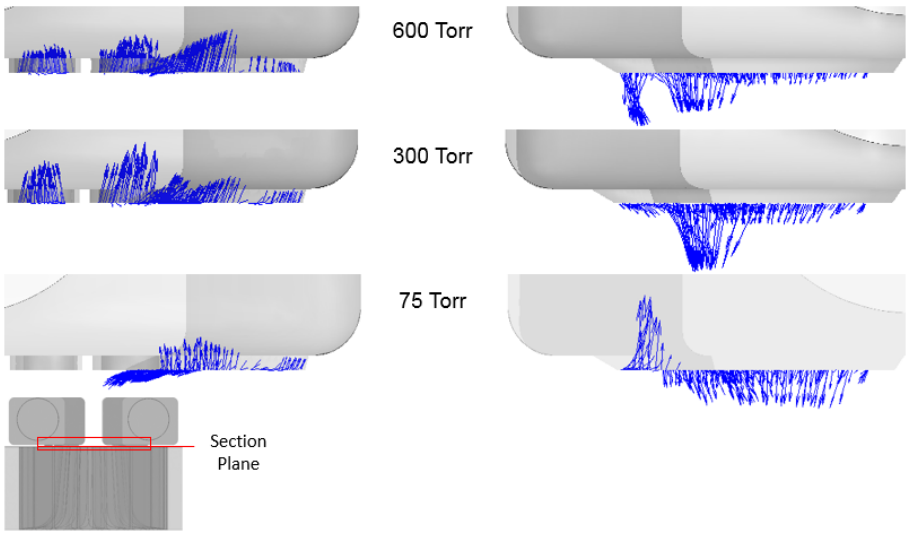

Fig. 4.23. Velocity vectors at suction port (right) and discharge ports (left) for P_{in}=600, 300, 75 Torr (top to bottom)

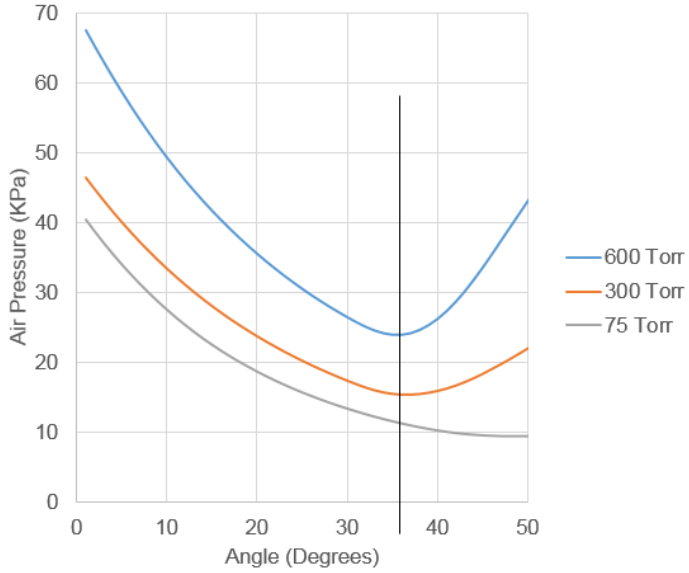

Fig. 4.24. Volume averaged air pressure near suction. The black line indicates the angular coordinate at the onset of suction

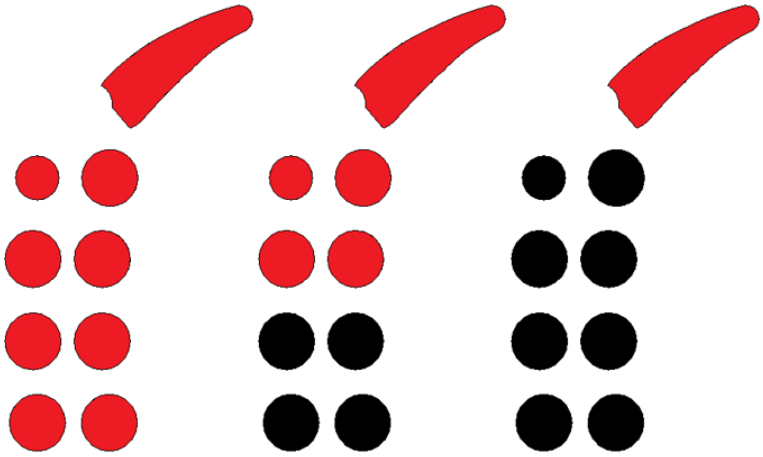

Fig. 4.25. Discharge port behavior for P_{in} = 600, 300, 75 Torr (Left to Right) Red indicates open ports, Black indicates closed ports

4.4.2 Temperature

Fig. 4.26 shows how the P_{in} affect the temperature of the air between the blades. As P_{in} decreases, the compression ratio - i.e., the ratio of maximum to the mini-

mum volume occupied by the air between the blades during the compression process increases. Since the compression ratio increases with decreasing P_{in} and the temperature of the air at the suction chambers inlet is kept constant, the temperature of the discharge air increases with decreasing P_{in}.

Fig. 4.26. Volume averaged air temperature in a region between the blades with angular coordinate (similar to Fig. 5.12) for P_{in}=600, 300, 75 Torr for ω=1750 RPM

4.5 Effects of Rotational Speed

In this section, the effect of the operating parameter, rotational speed (ω) on the nature of flow in the liquid ring vacuum pump is discussed. Fig. 4.27 and 4.28 shows how changes in the rotational speed (ω = 1750, 1450, 1150 rpm) for a given suction and exhaust pressure (P_{in} = 300 Torr and P_e = 1 atm) affect the water-ring shape and the pressure distribution in the water ring and the ingested air.

From Fig. 4.27, it can be seen that when the rotational speed decreases from ω = 1750 to 1150 rpm, the elliptical shape of the rings inner surface rotates in a direction opposite to that of the impeller. This is because the pressure gradient from

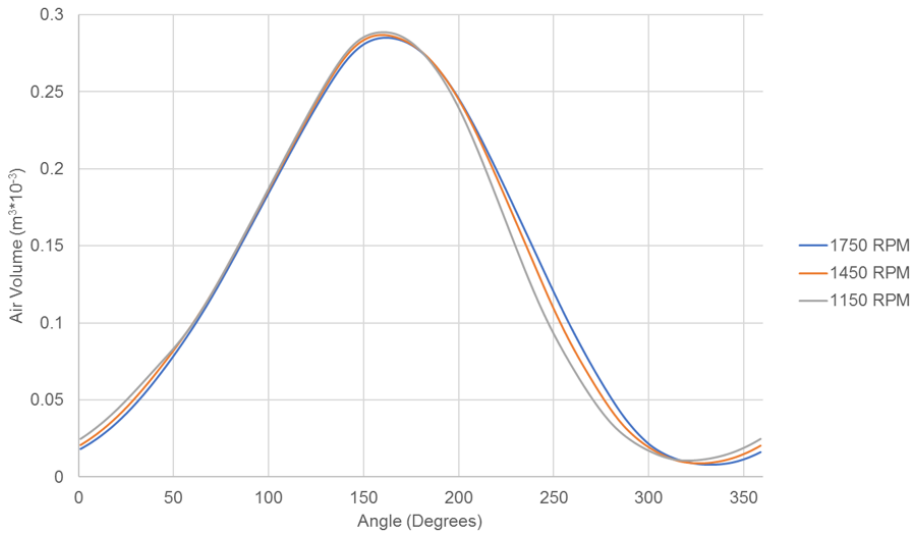

Fig. 4.27. Air volume in a region between the blades with angular coordinate (similar to Fig. 5.12) for ω=1750, 1450, 1150 RPM for P_{in}=300 Torr

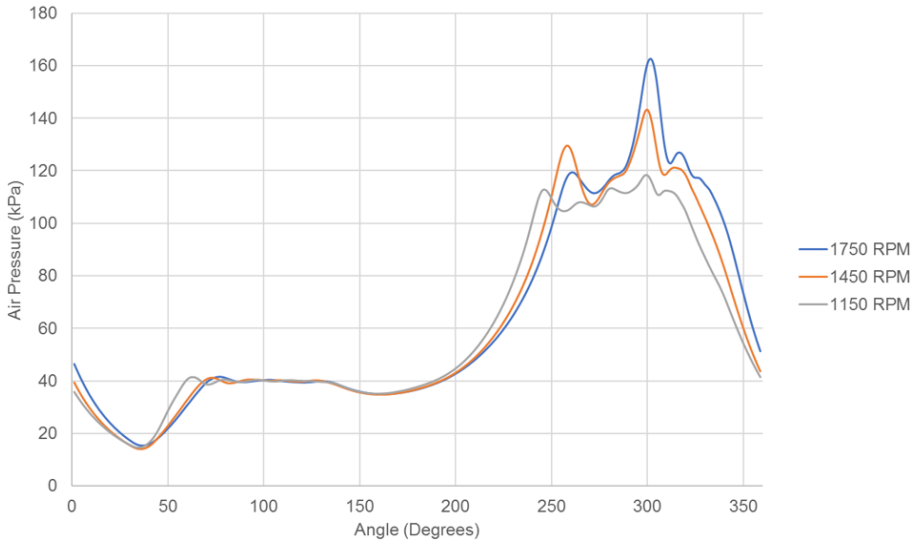

Fig. 4.28. Volume averaged pressure of air in a region between the blades with angular coordinate (similar to Fig. 5.12) for ω=1750, 1450, 1150 RPM for P_{in}=300 Torr

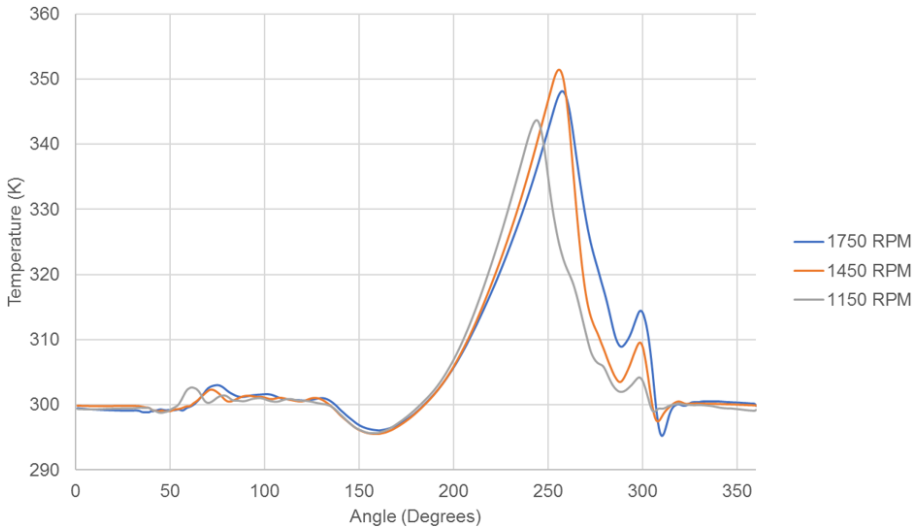

Fig. 4.29. Volume averaged temperature of air in a region between the blades with angular coordinate (similar to Fig. 5.12) for ω=1750, 1450, 1150 RPM for P_{in}=300 Torr

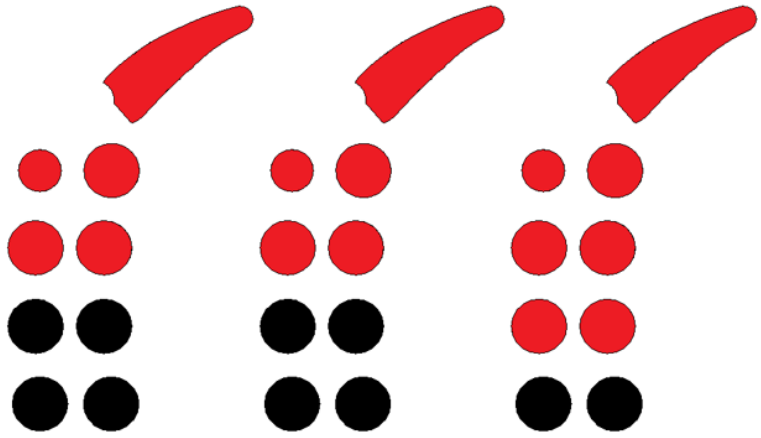

Fig. 4.30. Discharge port behavior for ω=1750, 1450, 1150 RPM (Left to Right) Red indicates open ports, Black indicates closed ports

the discharge port to the suction port is balanced by less resistance from the flow at lower rotational speeds. This change in shape is important because it affects the compression ratio from BDC to when the first discharge port opens. Lowering the

rotational speed was found to increase the compression ratio, which increases the pressure and temperature of the air between the blades as the impeller rotates (see Fig. 4.28 and 4.29). Since the discharge ports open only when the pressure of the air in the region between the blades is higher than P_e, the discharge ports open at lower θ when the rotational speed is lower (Fig. 4.30). This change in shape also affects the volume available for expansion from the end of discharge to when the suction port opens. Lowering the rotational speed was found to increase the volume available during the expansion process. Thus, $P_{S,i}$ reduces with decrease in rotational speed, which reduces the temperature and density of the air in the region between the blades when the suction port first opens.

5. PHYSICS BASED REDUCED ORDER MODEL FOR PREDICTING PERFORMANCE OF LIQUID RING VACUUM PUMPS

5.1 Introduction

As noted, although liquid-ring vacuum pumps are efficient and robust, manufacturers have aggressive goals on improving efficiency, performance, and range of operations. Improving design requires detailed understanding of the flow and heat transfer as a function of design and operating parameters. This knowledge could be obtained by CFD or experiments. However, both approaches require considerable time and resources. A physics-based reduced-order model that encapsulates the understanding gained from CFD and experiments would be most useful for preliminary design. This is because such models can provide the information needed with minimal time and resources. Pardeshi et al. [23] developed a semi-empirical reduced order model to predict the pump capacity, and the predictions were reasonable. However, the model was developed primarily by curve fitting the experimental data as a function of key dimensionless parameters. As a result, the model has limited range of applicability. Huang et al. [24] developed a model for predicting the performance of a liquid ring vacuum pump, and their predictions on pump capacity and power matched experimental data with reasonable accuracy. However, on pump capacity, their model assumes isentropic expansion after discharge which is not supported by the CFD study conducted in this work. In the model by Huang et al. [24], the variation of power due to suction pressure is attributed to changes in compression work of the gas, and the compression was also assumed to be isentropic. Again, this is not supported by the CFD study conducted in this work. The CFD study found the

changes in liquid content to be predominantly responsible for changes in power and the compression process to be polytropic.

Thus, the objective is to develop a physics based reduced order model based on the understanding gained from the CFD study. The proposed model allows to predict the rate of air ingested and power consumed by the pump as a function of design and operating parameters and can be used in preliminary design of liquid ring vacuum pumps.

In the subsequent sections, the development of physics based reduced order model is described. It's validation and range of applicability are also described.

5.2 Problem Description for the Physics Based Reduced Order Model

The liquid ring vacuum pump problem studied is the same as that described in Chapter 2. Some of the key features are repeated as housing (radius = r_c); an impeller (tip radius = r_i, hub radius = r_h, blade thickness = th_b, blade angle = δ, number of blades = n_b, eccentricity = e) and rotating at rotational speed ω; and a suction/exhaust chamber. At the inlet boundary, pressure level of P_{in} is applied. At the outlet boundary, pressure level of P_{out} is applied (see Fig. 5.1).

Five different configurations of the liquid ring vacuum pump were used to validate the model developed. The details of these configurations are described in Fig. 5.2. Of these configurations, CFD analyses were performed only for configuration 1. Experimental data however is available for all five configurations.

5.3 Model Development

This section describes the development of the reduced order model. The CFD study showed that a certain volume of air (residual air) gets left behind in the region between the blades after discharge. Since this residual air is at near discharge pressure, the volume of the residual air increases when it reaches the suction port. This decreases the effective volume available in the region between the blades for the pump

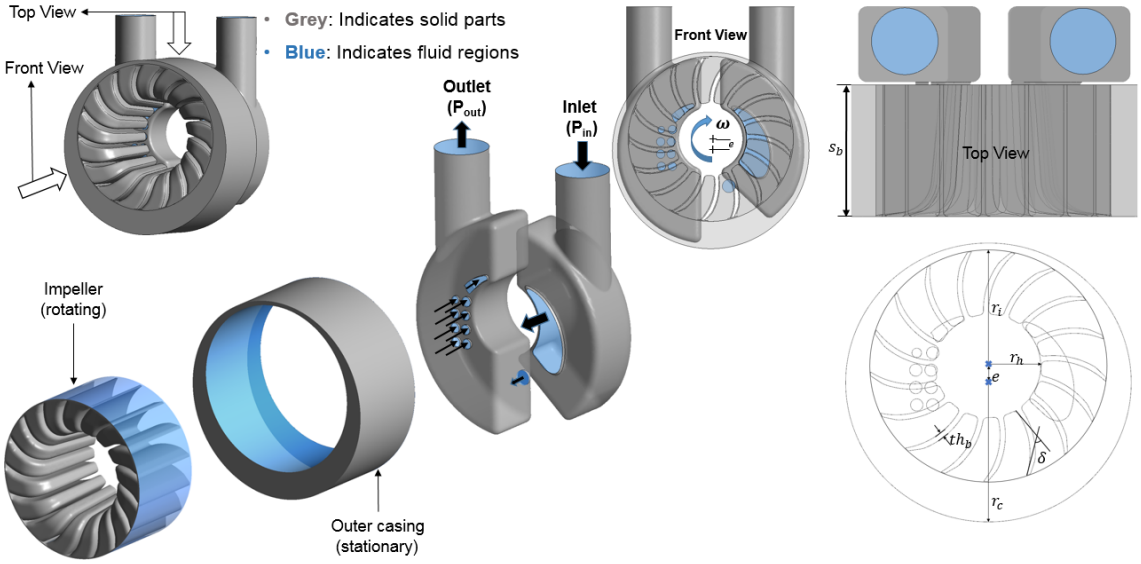

Fig. 5.1. Problem Description

Configuration	#1	#2	#3	#4	#5
$r_c\ (m)$	∅	0.21	0.1365	0.3145	0.407
$s_b\ (m)$	∅	0.368	0.215	0.5	0.708
$r_i\ (m)$	∅	0.18	0.105	0.25	0.36
$r_h(m)$	∅	0.09	0.0535	0.125	0.177
$e\ (m)$	∅	0.023	0.0136	0.0316	0.04
$th_b\ (m)$	∅	0.008	0.008	0.01	0.012
κ	∅	0.12	0.1	0.1	0.09
n_b	17	18	12	15	18
δ	∅	56	40	42	45
ω (RPM)	1750, 1450, 1150	1170, 980, 790	1450, 1300, 1170	920,740, 590	590, 490, 372
P_{in} (Torr) range for all ω	25 - 680	25 - 680	25 - 680	25 - 680	25 - 680

Fig. 5.2. Configurations studied. Configuration 1 is proprietary

to ingest air thereby reducing the pump capacity. As the suction pressure decreases, this volume change (in this case, volume increase) of residual air increases assuming the volume of residual air does not change with suction pressure. But if the liquid ring changes, the volume of residual air left after discharge will also change. So the

effects of polytropic expansion of the gas and the change of the liquid ring shape must be accounted for in predicting the pump capacity. On the power consumption, the shape of the liquid ring is in direct correlation with the amount of water that the impeller has to rotate inside the pump chamber. The water in the pump chamber acts as resistance to the impeller in rotation. This is the predominant source of power consumption in a liquid ring vacuum pump. Therefore, the change of the liquid ring shape must be accounted for in predicting the power consumption as well.

The CFD study showed that the shape of the liquid ring primarily depends on the centrifugal force from rotation, acceleration/deceleration from differences in the pumps pressure at its inlet and outlet, and impellers eccentricity relative to the pumps housing. As the suction pressure decreases, the air-water interface goes from approximately elliptical with its major axis nearly vertical to circular to elliptical again except with its major axis nearly horizontal. These changes occur because a decrease in P_{in} for a given P_{out} increases the pressure gradients in the liquid ring between the discharge ports and the suction port. On the other hand, when the rotational speed decreases, the elliptical shape of the rings inner surface rotates in a direction opposite to that of the impeller. This is because the pressure gradient from the discharge port to the suction port is balanced by less resistance from the flow at lower rotational speeds. These effects must be taken into account to predict the shape of the liquid ring.

To incorporate the insights gained from CFD to predict the performance parameters, the model involves eight key stages which are as follows:

1. Develop a model for the prediction of rate of gas ingested assuming the shape of the liquid ring is known.

2. Develop a model for prediction of torque exerted by the fluids on the impeller assuming the shape of the liquid ring is known.

3. Develop a procedure for prediction of shape of the liquid ring. Through this, the volume of air between the blades as a function of angular position is calculated.

4. Using the information on volume of air between the blades as a function of angular position, develop a model for prediction of pressure of air between the blades as a function of angular position. At this point, all the variables required to predict the pump capacity are known. The information on volume and pressure of air between the blades is used to calculate the rate of air ingested by the pump.

5. Using the information on velocity profile of liquid flow at BDC location from CFD study, develop a model for the flow rate of liquid in the liquid-ring.

6. Using the information on flow rate of liquid in the liquid-ring and the shape of the liquid ring, develop a model for prediction of rotational speed distribution in the liquid-ring.

7. Using the information on rotational speed distribution and pressure of air between the blades, develop a model for prediction of pressure distribution in the liquid-ring

8. Using the information on pressure distribution in the liquid-ring, develop a model for prediction of pressure on the blade surfaces. At this point, all the variables required to predict the torque exerted by the fluids on the impeller are known. The information on pressure on the blade surfaces is used to get the torque exerted by the fluids on the impeller.

In the subsequent sections, the aforementioned stages in the model are described.

5.3.1 Rate of Gas Ingested by the Pump (Pump Capacity)

The CFD study conducted showed that the shape of the liquid ring decides on how much air the pump can ingest since that shape was found to play a dominant role in creating the expansion ratio or the vacuum needed to draw air into the pump through the suction port and the compression ratio needed to expel the air through

the discharge ports. By applying continuity to the control volume marked by thick black lines (1 and 2 in Fig. 5.3), the impeller's hub surface on one side and the liquid ring surface on the other side for the rate of air ingested by the pump yield,

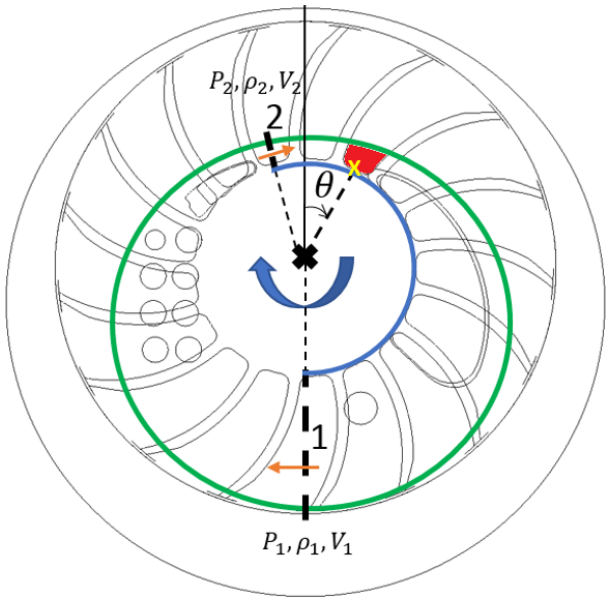

Fig. 5.3. Control volume for application of continuity

$$\dot{m}_{in} = \dot{m}_1 - \dot{m}_2 \tag{5.1}$$

This could be written as,

$$\rho_{in} Q_{in} = \rho_1 Q_1 - \rho_2 Q_2 \tag{5.2}$$

Rearranging yields,

$$Q_{in} = \frac{\rho_1}{\rho_{in}} Q_1 - \frac{\rho_2}{\rho_{in}} Q_2 \tag{5.3}$$

Since the air experiences polytropic processes between end of suction to BDC and from ed of discharge to start of suction, the above equation becomes,

$$Q_{in} = \left(\frac{P_{a1}}{P_{in}}\right)^{1/\gamma_1} Q_1 - \left(\frac{P_{a2}}{P_{in}}\right)^{1/\gamma_2} Q_2 \tag{5.4}$$

where the volume flow rate Q_1 and Q_2 are given as:

$$Q_1 = \frac{V_{a1}}{t_{blps}};\ Q_2 = \frac{V_{a2}}{t_{blps}};\ t_{blps} = \frac{2\pi}{\omega n_b} \tag{5.5}$$

In the above equation, V_{a1} is the volume of air between the blades at surface 1 and V_{a2} is the volume of air between the blades surface 2 and t_{blps} is time per blade passing. Since V_{a1} and V_{a2} can vary with time, the V_{a1} and V_{a2} are the ones when the "X" (see Fig. 5.3) coincides with surface 1 and 2 where "X" is a location on surface of the impeller midway between the blades.

5.3.2 Torque Exerted by the Fluids on the Impeller (Power Consumption)

The CFD study conducted also showed that the shape of the liquid ring decides on the power consumption since that shape is in is in direct correlation with the amount of water the impeller has to rotate inside the pump chamber and the resistance offered by the water to the impeller in its rotation is a predominant source of power consumption in a liquid ring vacuum pump. Each blade is partitioned into a finite number of elements as shown in Fig. 5.4. The total number of blade elements is N_e. Application of a force balance to a blade element in a non-inertial reference frame gives,

$$\vec{F} - \int_V \vec{a}_{rel}\, dm = \sum \vec{F}_B + \sum \vec{F}_S \tag{5.6}$$

The CFD data shows that the force due to shear stress by the fluids is less than 0.2% of the total force on the impeller. So, surface forces due to friction ($\vec{F}_{S3}$ and $\vec{F}_{S4}$) can be neglected. So the net surface force is given by,

$$\sum \vec{F}_S = \vec{F}_{S1} + \vec{F}_{S2} = \int_S P(-\hat{n})\, dA = (P_i - P_b) A_e \hat{n} \tag{5.7}$$

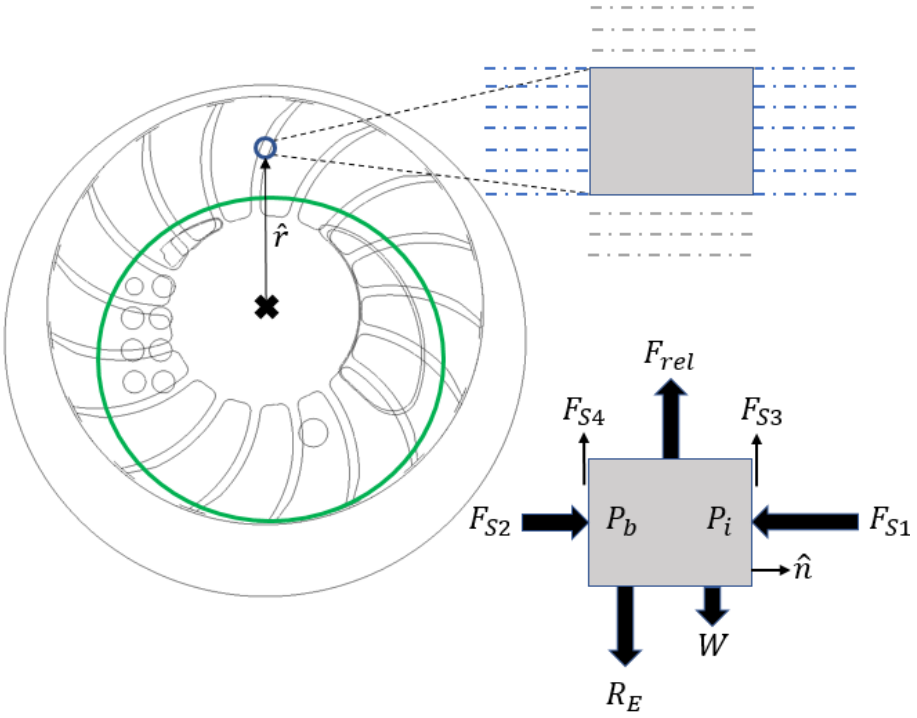

Fig. 5.4. An element on impeller blade with its free body diagram; grey indicates solid regions; blue indicates fluid regions

The acceleration of the non-inertial frame, $\vec{a}_{\text{rel}}$ can be written as,

$$\vec{a}_{rel} = \frac{d^2\vec{R}}{dt^2} + \frac{d\vec{\omega}}{dt} \times \vec{r} + 2\vec{\omega} \times \vec{r} + \vec{\omega} \times (\vec{\omega} \times \vec{r}) \tag{5.8}$$

Linear acceleration of the frame's origin is zero. So,

$$\frac{d^2\vec{R}}{dt^2} = 0 \tag{5.9}$$

Angular acceleration is zero. So,

$$\frac{d\vec{\omega}}{dt} \times \vec{r} = 0 \tag{5.10}$$

Coriolis acceleration is zero. So,

$$2\vec{\omega} \times \vec{r} = 0 \tag{5.11}$$

Centrifugal acceleration is non-zero. So,

$$\vec{\omega} \times (\vec{\omega} \times \vec{r}) = \omega^2 r\hat{r} \tag{5.12}$$

So, The acceleration of the non-inertial frame, $\vec{a}_{\mathrm{rel}}$, becomes,

$$\vec{a}_{rel} = \omega^2 r\hat{r} \tag{5.13}$$

Using the lowest rotational speed tested (1150 RPM) for configuration 1 at lowest possible radius ($\mathrm{r_h}$), it can be found that the gravity is less than 1% of centrifugal acceleration for the case. So, force due to gravity (W) can be neglected. This results in,

$$\sum \vec{F}_B = \vec{R}_E \tag{5.14}$$

Here, $\vec{R}_{\mathrm{E}}$ is the reaction on the blade element shown in Fig. 5.4 by the blade elements in its vicinity. So total force on the blade element becomes,

$$\vec{F} = (P_i - P_b)A_e\hat{n} + m_e\omega^2 r\hat{r} + \vec{R}_E \tag{5.15}$$

Equilibrium in radial direction (assuming inelastic material) mandates:

$$\vec{R}_E = -m_e\omega^2 r\hat{r} \tag{5.16}$$

So total force on the blade element is approximately,

$$\vec{F} = (P_i - P_b)A_e\hat{n} \tag{5.17}$$

With the force on the blade element known, the torque on the blade element can is,

$$\vec{T_j} = \vec{r} \times \vec{F} \tag{5.18}$$

Putting the force in the equation for torque given,

$$\vec{T_j} = \vec{r} \times ((P_i - P_b)A_e\hat{n}) \tag{5.19}$$

Rearranging:

$$\vec{T_j} = r(P_i - P_b)A_e(\hat{r} \times \hat{n}) \tag{5.20}$$

The cross product comes out as:

$$\hat{r} \times \hat{n} = \sin\beta\hat{k} \tag{5.21}$$

where β is the angle between $\hat{r}$ and $\hat{n}$. So, the final equation for torque becomes:

$$\vec{T_j} = r(P_i - P_b)A_e \sin\beta\hat{k} \tag{5.22}$$

The total torque is the vector summation of the torque over all the blade elements which is given by,

$$\vec{T} = \sum_{j=1}^{N_e} \vec{T_j} \tag{5.23}$$

While summing, note that some of the blade elements are exposed to gas only while some are exposed to liquid only. Once the torque is known, the power (PW) can be calculated as follows:

$$PW = T\omega \tag{5.24}$$

Now, power (PW) and torque (T) can be used interchangeably for analysis since they differ only by a scaling factor ω (rotation speed).

Equations (5.6)-(5.23) calculates torque exerted by the fluid on the impeller at one angular position. Since the torque is function of its angular position it needs to be calculated at a series of positions of impeller and then averaged. In this study, $\vec{T}$ is computed at N angular positions with each position separated by one degree, where N=360/n_b.

5.3.3 Procedure to Construct the Ring

In this section, shape of the liquid ring is modelled. The CFD study conducted showed that the shape and location of the liquid ring to strongly depend on centrifugal force from rotation and acceleration/deceleration from the difference in the pressure at the discharge and suction ports along with the eccentricity of the impeller relative to the pump housing. Variation in suction pressure changes the pressure gradient in the azimuthal direction. This causes liquid ring to change shape accordingly. The liquid ring is approximately elliptical with its major axis nearly vertical when P_{in} = 600 Torr, circular when P_{in} drops to 300 Torr, and elliptical again except with its major axis nearly horizontal when P_{in} drops further to 75 Torr. Variation in rotational speed changes the balance between centrifugal acceleration and pressure gradient in azimuthal direction. So, when the rotational speed decreases from ω = 1750 to 1150 rpm, the elliptical shape of the rings inner surface rotates in a direction opposite to that of the impeller. This says that the liquid ring is a strong function of design and operating parameters.

One approach to model the liquid ring's inner surface is to separate the effects of geometry and operating conditions. The geometry effects are embedded in a curve referred to as the base curve and the effects of operating conditions are embedded as correction to the base curve. The base curve is chosen to be a circle and is constructed with the help of the following information: impeller radius, hub radius and eccentricity as shown below,

$$(x - x_{cb})^2 + (y - y_{cb})^2 = r_1^2 \tag{5.25}$$

where:

$$x_{cb} = k_{\mathrm{x}} e_x \tag{5.26}$$

$$y_{cb} = k_{\mathrm{y}} e_y \tag{5.27}$$

$$r_1 = \frac{r_\mathrm{i} + r_\mathrm{h}}{2} \tag{5.28}$$

$$k_x = 0.95\left(\frac{r_i - r_h}{2e_x}\right)^{0.9} \tag{5.29}$$

$$k_y = 0.95\left(\frac{r_i - r_h}{2e_y}\right)^{0.9} \tag{5.30}$$

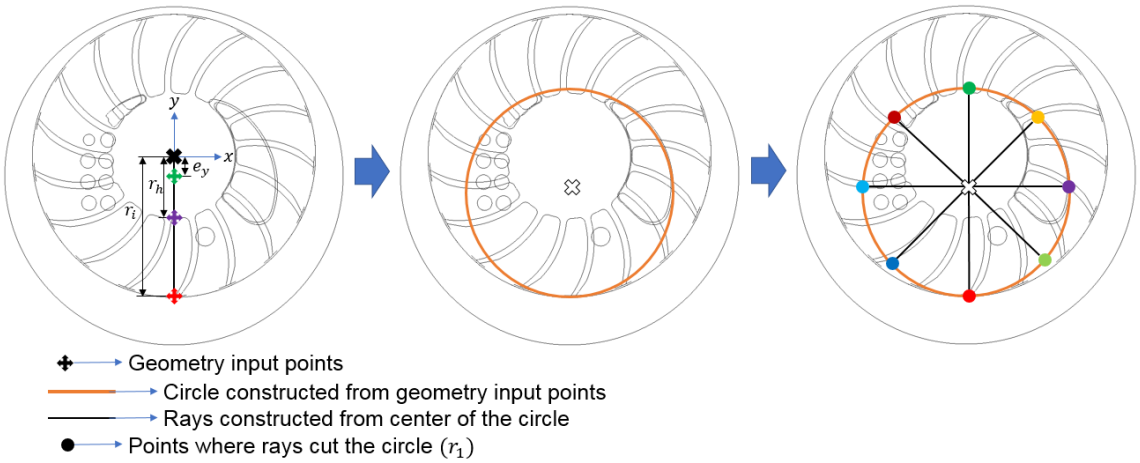

Fig. 5.5. Construction of base curve

The coefficients that describe the center of the base curve (k_x, k_y) were determined to ensure that at BDC the liquid and the impeller will not have a gap for the gas to flow past blades. With the base curve defined, geometry of the liquid ring's inner surface can be developed as a correction to the radius of the base curve (see Fig. 5.6) as follows:

$$\mathbf{r_2} = r_1 * \boldsymbol{\phi} \tag{5.31}$$

where $\mathbf{r_2}$ is the radial distance from the center of the base curve to the inner surface of the liquid ring and ϕ, which is function of the angular position, is the correction

factor. To get ϕ, eight points are chosen at equal angular intervals on the base curve as shown in Fig. 5.5, so that Eq. (5.31) becomes,

$$\mathbf{r_2} = \begin{bmatrix} r_{21} \\ r_{22} \\ r_{23} \\ r_{24} \\ r_{25} \\ r_{26} \\ r_{27} \\ r_{28} \end{bmatrix} = \begin{bmatrix} r_1\phi_1 \\ r_1\phi_2 \\ r_1\phi_3 \\ r_1\phi_4 \\ r_1\phi_5 \\ r_1\phi_6 \\ r_1\phi_7 \\ r_1\phi_8 \end{bmatrix} \tag{5.32}$$

To get $\boldsymbol{\phi}$, it is noted that in the CFD analysis conducted, it was observed that the liquid ring surface is approximately elliptical. The general equation for an ellipse is,

$$x^2 + Axy + By^2 + Cx + Dy + E = 0 \tag{5.33}$$

From the above equation, it can be seen that five points are required to define an ellipse. Via trial and error, it was found that five points are too few to capture the effects of the operating conditions on the liquid ring geometry. However, eight points were found to be adequate capturing the effects of operating conditions on the liquid-ring geometry. So, another type of closed curve is used to represent the inner surface of the liquid ring and it is given by,

$$Ax^4 + By^4 + Cx^2y + x^2 + Dxy + Ey^2 + Fx + Gy + H = 0 \tag{5.34}$$

The eight points are equally spaced and have following angular position:

$$\boldsymbol{\theta} = \begin{bmatrix} \theta_1 \\ \theta_2 \\ \theta_3 \\ \theta_4 \\ \theta_5 \\ \theta_6 \\ \theta_7 \\ \theta_8 \end{bmatrix} = \begin{bmatrix} 0^{\text{o}} \\ 45^{\text{o}} \\ 90^{\text{o}} \\ 135^{\text{o}} \\ 180^{\text{o}} \\ 225^{\text{o}} \\ 270^{\text{o}} \\ 315^{\text{o}} \end{bmatrix} \tag{5.35}$$

The $\boldsymbol{\phi}$ at each of those points were found to depend on,

$$F_{\text{P}_{\text{in}}} = \frac{P_{\text{in}}}{P_{\text{out}}} \tag{5.36}$$

$$F_{\omega} = \frac{1}{2}\frac{\rho\omega^2 {r_{\text{i}}}^2}{P_{\text{out}}} \tag{5.37}$$

Details on how $\boldsymbol{\phi}$ depends on $\text{F}_{\text{P}_{\text{in}}}$ and F_{ω} will be given later in this section. Once the $\boldsymbol{\phi}$ is defined, a system of linear equations is solved to find the coefficients in Eq. (5.34) as follows:

$$\begin{bmatrix} x_1^4 & y_1^4 & x_1^2y_1 & x_1y_1 & y_1^2 & x_1 & y_1 & 1 \\ x_2^4 & y_2^4 & x_2^2y_2 & x_2y_2 & y_2^2 & x_2 & y_2 & 1 \\ x_3^4 & y_3^4 & x_3^2y_3 & x_3y_3 & y_3^2 & x_3 & y_3 & 1 \\ x_4^4 & y_4^4 & x_4^2y_4 & x_4y_4 & y_4^2 & x_4 & y_4 & 1 \\ x_5^4 & y_5^4 & x_5^2y_5 & x_5y_5 & y_5^2 & x_5 & y_5 & 1 \\ x_6^4 & y_6^4 & x_6^2y_6 & x_6y_6 & y_6^2 & x_6 & y_6 & 1 \\ x_7^4 & y_7^4 & x_7^2y_7 & x_7y_7 & y_7^2 & x_7 & y_7 & 1 \\ x_8^4 & y_8^4 & x_8^2y_8 & x_8y_8 & y_8^2 & x_8 & y_8 & 1 \end{bmatrix} \begin{bmatrix} A \\ B \\ C \\ D \\ E \\ F \\ G \\ H \end{bmatrix} = \begin{bmatrix} x_1^2 \\ x_2^2 \\ x_3^2 \\ x_4^2 \\ x_5^2 \\ x_6^2 \\ x_7^2 \\ x_8^2 \end{bmatrix} \tag{5.38}$$

where,

$$x_{\mathrm{n}} = r_{2n}\cos\theta_{\mathrm{n}} + x_{\mathrm{cb}}\ ; n = 1 \text{ to } 8 \tag{5.39}$$

$$y_{\mathrm{n}} = r_{2n}\sin\theta_{\mathrm{n}} + y_{\mathrm{cb}}\ ; n = 1 \text{ to } 8 \tag{5.40}$$

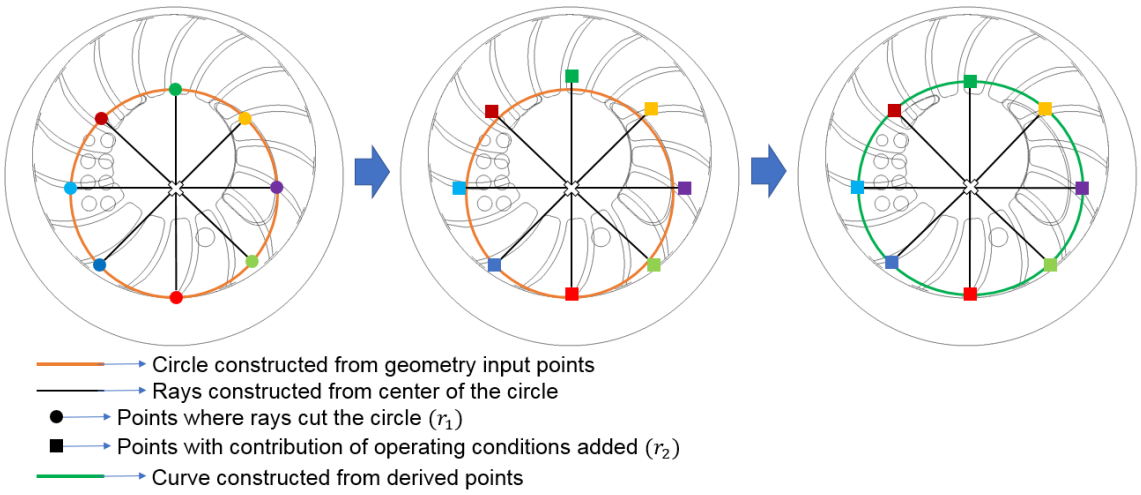

Fig. 5.6. Construction of liquid ring inner surface curve

5.3.4 Effects of Operating Conditions

To get $\boldsymbol{\phi}$, four steps are performed:

1. Develop model for the geometry of the blade.
2. Develop a model for the air volume as a function of the liquid ring shape (account for the variation in the hub radius)
3. Determine $\boldsymbol{\phi}$ for CFD cases.
4. Generalize $\boldsymbol{\phi}$ as a function of operating conditions.

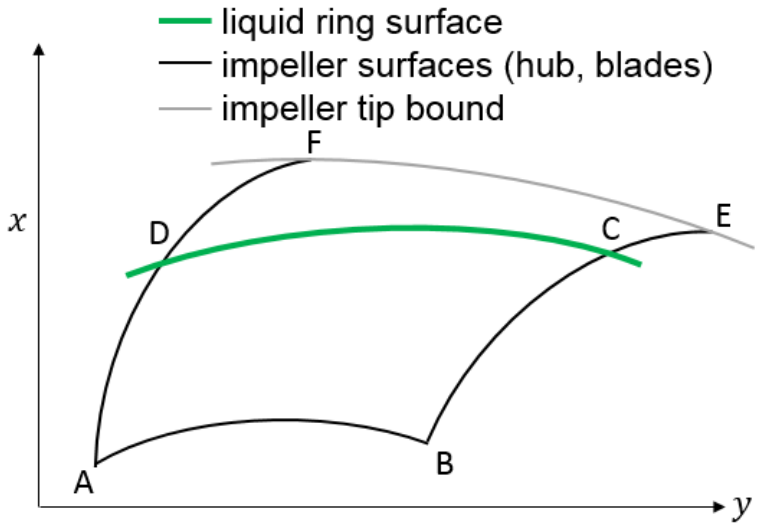

Fig. 5.7. Schematic of region between the blades with liquid ring and impeller tip bound

Model for Blade Geometry

The equation for blade contour needs to be derived. In the present approach, the blade is assumed to be a circular arc. Using this and the available geometric parameters (impeller radius, hub radius, number of blades, blade angle and thickness of the blades), an equation for the blade contour can be derived.

Fig. 5.8 shows schematic of blade contour. From this figure, it can be noticed that the center of the circular arc is at (r_h, -r_b) and the radius of the circular arc is r_b. So the equation of the circular arc can be given as:

$$(x - r_h)^2 + (y + r_b)^2 = r_b^2 \tag{5.41}$$

In the above equation, r_b is unknown and needs to be calculated. Since the impeller tip is located at T, applying distance formula between O and T gives,

$$\sqrt{(r_b \sin\delta + r_\mathrm{h})^2 + (r_b \cos\delta - r_b)^2} = r_\mathrm{i} \tag{5.42}$$

Squaring both sides,

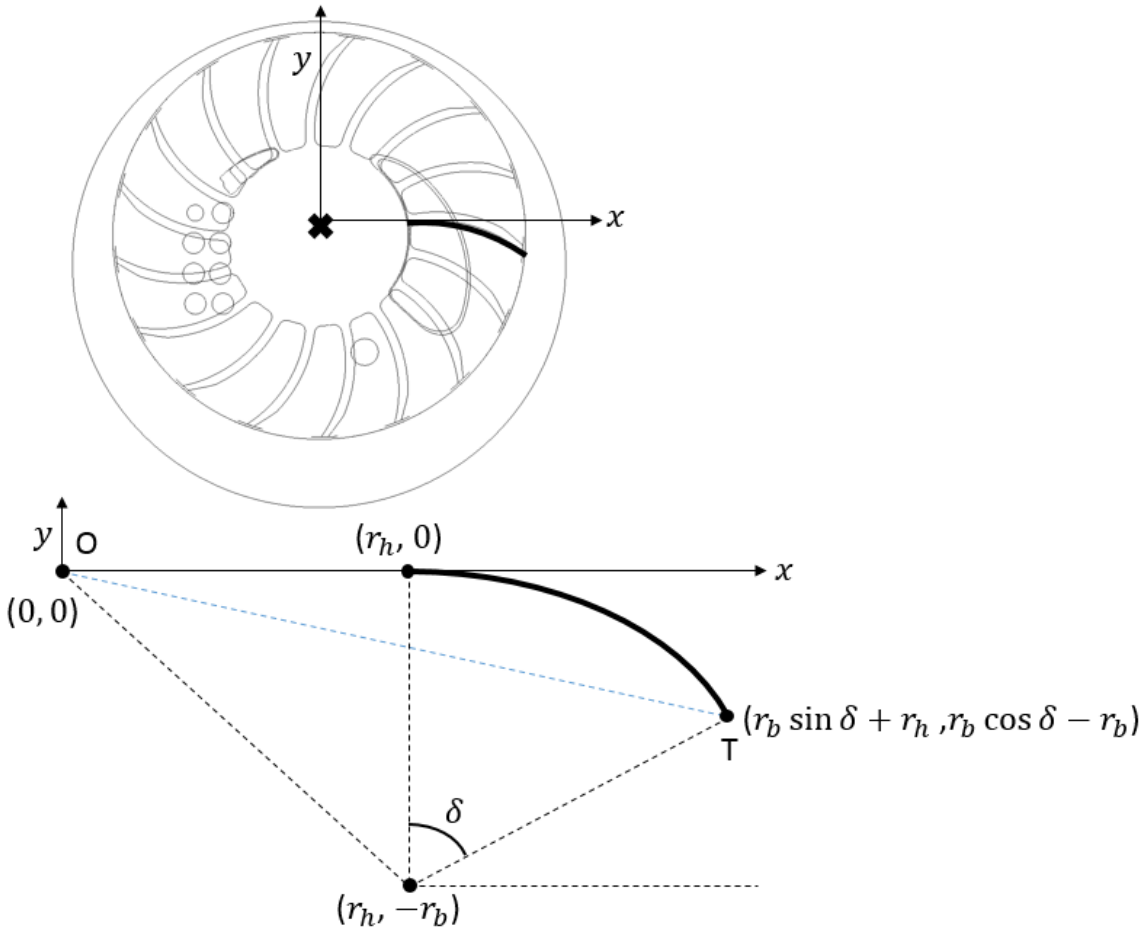

Fig. 5.8. Schematic of blade contour

$$(r_b \sin\delta + r_\mathrm{h})^2 + (r_b \cos\delta - r_b)^2 = r_i^2 \tag{5.43}$$

Rearranging,

$$r_b^2(1-\cos\delta) + r_b(r_\mathrm{h}\sin\delta) - \frac{r_i^2 - r_h^2}{2} = 0 \tag{5.44}$$

This is a quadratic equation in r_b. The positive root of the equation is the solution of interest, which is:

$$r_b = \frac{\sqrt{r_h^2\sin^2\delta + 2(1-\cos\delta)(r_i^2 - r_h^2)} - r_\mathrm{h}\sin\delta}{2(1-\cos\delta)} \tag{5.45}$$

Equation (5.41) and (5.45) defines the equation of the blade contour.

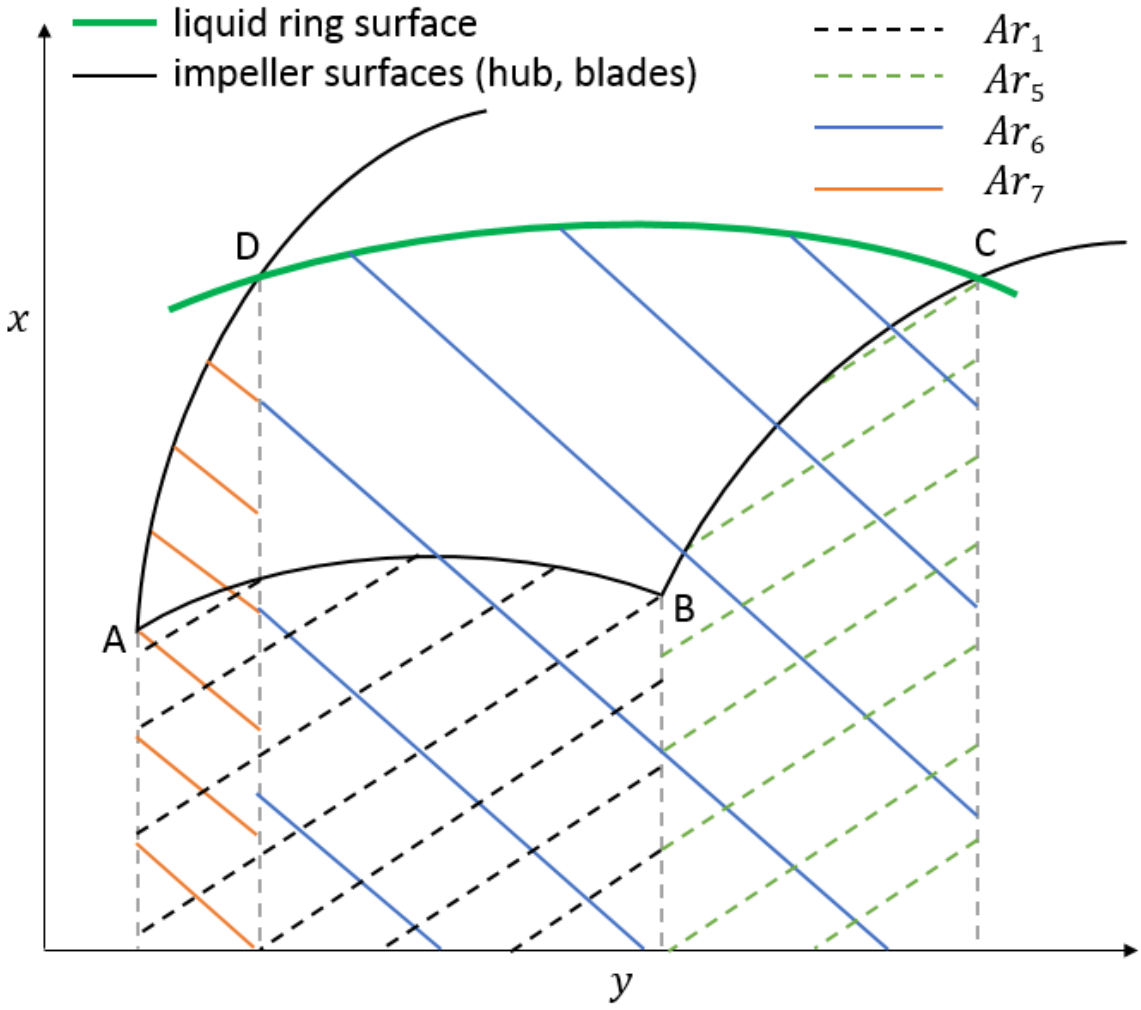

Fig. 5.9. Schematic of volume of air between the blades

Model for Air Volume Between the Blades

To calculate, the air volume between the blades, $\mathrm{Ar_{ABCD}}$ needs to be calculated (see Fig. 5.7). To get $\mathrm{Ar_{ABCD}}$, $\mathrm{Ar_1}$, $\mathrm{Ar_5}$, $\mathrm{Ar_6}$ and $\mathrm{Ar_7}$ are required (see Fig. 5.9). To get $\mathrm{Ar_1}$, equation for AB is needed, which is:

$$x^2 + y^2 = r_h^2 \tag{5.46}$$

Then the area becomes:

$$Ar_1 = \int_{y_A}^{y_B} f_1(y)dy \tag{5.47}$$

where:

$$f_1(y) = \sqrt{r_h^2 - y^2} \tag{5.48}$$

This can be analytically integrated between points A and B. Points A and B can be arrived at from geometrical information of pump configuration. To get Ar_5, equation for BC is needed, which is:

$$(x - x_{cr})^2 + (y - y_{cr})^2 = (r + th_{bl})^2 \tag{5.49}$$

where:

$$x_{cr} = r_h \cos\delta - r \sin\delta \tag{5.50}$$

$$y_{cr} = -(r_h \sin\delta + r \cos\delta) \tag{5.51}$$

$$r = \frac{\sqrt{r_h^2 \sin^2\delta + 2(1 - \cos\delta)(r_i^2 - r_h^2)} - r_{\mathrm{h}} \sin\delta}{2(1 - \cos\delta)} \tag{5.52}$$

Then the area becomes:

$$Ar_5 = \int_{y_B}^{y_C} f_2(y)dy \tag{5.53}$$

where:

$$f_2(y) = \sqrt{(r + th_{bl})^2 - (y - y_{cr})^2} + x_{cr} \tag{5.54}$$

This can be analytically integrated between points B and E. Point C is the intersection point between liquid ring surface curve and curve BC and is arrived at by solving a system of non-linear equations containing equation for curve BC and liquid ring surface curve for every discrete position of impeller section. To get Ar_6, equation for CD is needed, which is:

$$Ax^4 + By^4 + Cx^2y + x^2 + Dxy + Ey^2 + Fx + Gy + H = 0 \tag{5.55}$$

Then the area becomes:

$$Ar_6 = \int_{y_C}^{y_D} f_3(y)dy \tag{5.56}$$

$\mathrm{f_3(y)}$ is an implicit function so analytical integration cannot be performed. To integrate, numerical integration is employed.

$$Ar_6 = \int_{y_C}^{y_D} f_3(y)dy = \sum_{i=1}^{N} f_3(y_i)\Delta y \tag{5.57}$$

where, $y_1 = y_C$ and $y_N = y_D$. To find $\mathrm{f_3(y_i)}$, root finding at the corresponding discrete $\mathrm{y_i}$ is employed. Point D is the intersection point between liquid ring surface curve and curve AB and is arrived at by solving a system of non-linear equations containing equation for curve AB and liquid ring surface curve for every discrete position of impeller section. To get Ar_7, equation for DA is needed, which is:

$$(x - r_h)^2 + (y + r)^2 = r^2 \tag{5.58}$$

where:

$$r = \frac{\sqrt{r_h^2 \sin^2\delta + 2(1 - \cos\delta)(r_i^2 - r_h^2)} - r_\mathrm{h} \sin\delta}{2(1 - \cos\delta)} \tag{5.59}$$

Then the area becomes:

$$Ar_7 = \int_{y_A}^{y_D} f_4(y)dy \tag{5.60}$$

where:

$$f_4(y) = \sqrt{r^2 - (y+r)^2} + r_h \tag{5.61}$$

This can be analytically integrated between points A and D. So, now all the the elements to get $\mathrm{Ar_{ABCD}}$ are available. So, the area becomes:

$$Ar_{\mathrm{ABCD}} = Ar_6 + Ar_7 - Ar_5 - Ar_1 \tag{5.62}$$

With this area, assuming axial symmetry, the total volume between the blades becomes:

$$V_c = Ar_{\mathrm{ABCD}} * s_b \tag{5.63}$$

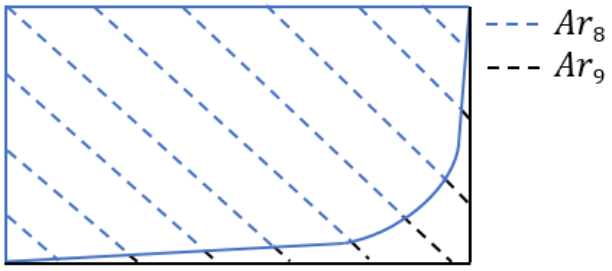

Fig. 5.10. Schematic of impeller blade in axial direction. $\mathrm{Ar_8}$ corresponds to actual design

Since the hub is not axially symmetric, the blade configuration is not axially symmetric (see Fig. 5.10). To account for this, the calculated volume $\mathrm{V_c}$ needs to be corrected. To arrive at the corrected air volume, a fraction of total available volume between the blades ($\mathrm{V_b}$) is subtracted from $\mathrm{V_c}$. So, the expression becomes:

$$V_a = V_c - \kappa V_b \tag{5.64}$$

For the configurations studied, κ was found to be between 0.09 and 0.12. With the above calculation the volume of air between the blades can be found for every discrete position of impeller.

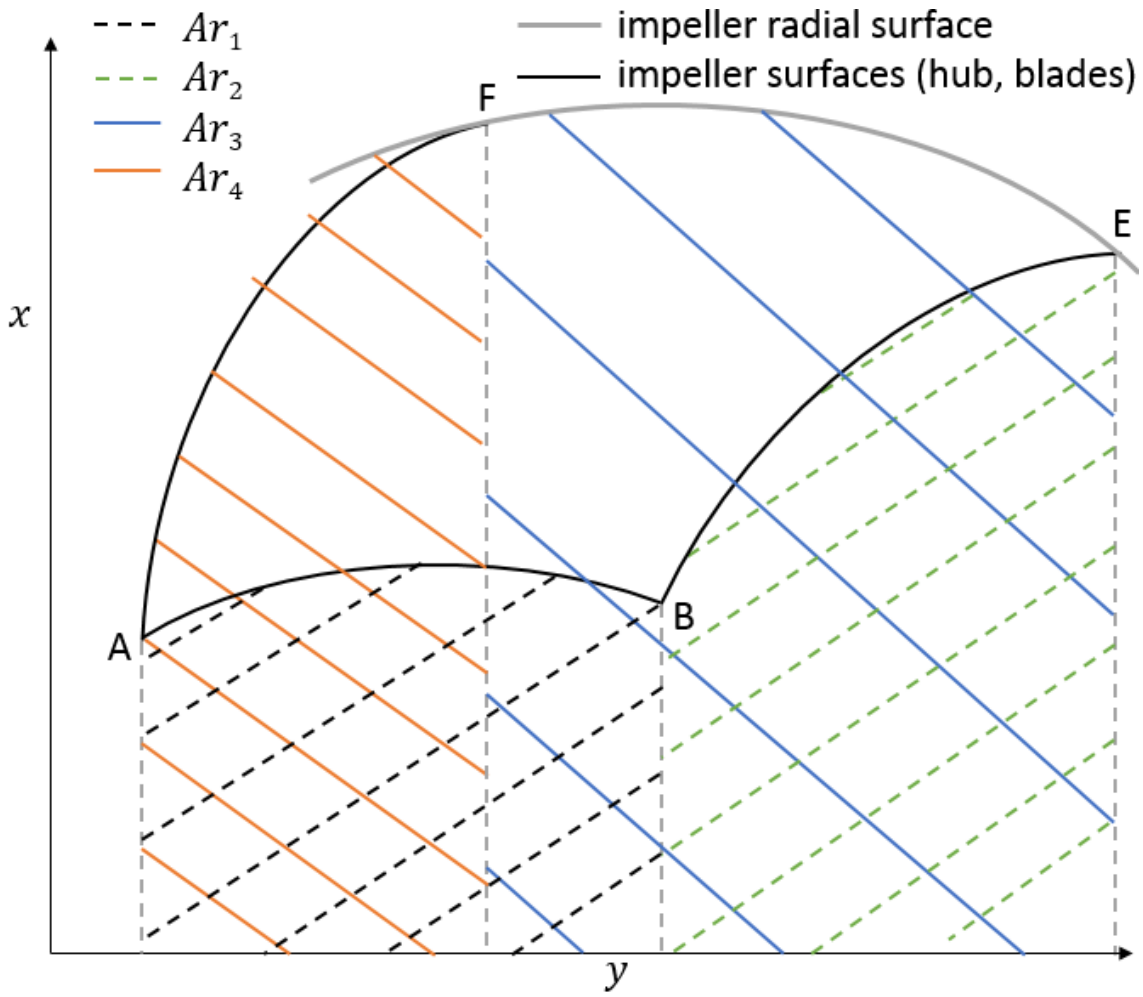

Fig. 5.11. Schematic of total volume available between the blades

To calculate the total available volume between the blades, area under ABEF needs to be calculated (see Fig. 5.7). To get $\mathrm{Ar_{ABEF}}$, $\mathrm{Ar_1}$, $\mathrm{Ar_2}$, $\mathrm{Ar_3}$ and $\mathrm{Ar_4}$ are required (see Fig. 5.11). To get $\mathrm{Ar_1}$, equation for AB is needed, which is:

$$x^2 + y^2 = r_h^2 \tag{5.65}$$

Then the area becomes:

$$Ar_1 = \int_{y_A}^{y_B} f_1(y)dy \tag{5.66}$$

where:

$$f_1(y) = \sqrt{r_h^2 - y^2} \tag{5.67}$$

This can be analytically integrated between points A and B. Points A and B can be arrived at from geometrical information of pump configuration. To get Ar_2, equation for BE is needed, which is:

$$(x - x_{cr})^2 + (y - y_{cr})^2 = (r_b + th_{bl})^2 \tag{5.68}$$

where:

$$x_{cr} = r_h \cos\delta - r_b \sin\delta \tag{5.69}$$

$$y_{cr} = -(r_h \sin\delta + r_b \cos\delta) \tag{5.70}$$

$$r_b = \frac{\sqrt{r_h^2 \sin^2\delta + 2(1-\cos\delta)(r_i^2 - r_h^2)} - r_{\mathrm{h}} \sin\delta}{2(1-\cos\delta)} \tag{5.71}$$

Then the area becomes:

$$Ar_2 = \int_{y_E}^{y_B} f_2(y)dy \tag{5.72}$$

where:

$$f_2(y) = \sqrt{(r_b + th_{bl})^2 - (y - y_{cr})^2} + x_{cr} \tag{5.73}$$

This can be analytically integrated between points B and E. Point E can be arrived at from geometrical information of pump configuration. To get Ar_3, equation for EF is needed, which is:

$$x^2 + y^2 = r_i^2 \tag{5.74}$$

Then the area becomes:

$$Ar_3 = \int_{y_F}^{y_E} f_3(y)dy \tag{5.75}$$

where:

$$f_3(y) = \sqrt{r_i^2 - y^2} \tag{5.76}$$

This can be analytically integrated between points F and E. Point F can be arrived at from geometrical information of pump configuration. To get Ar_4, equation for FA is needed, which is:

$$(x - r_h)^2 + (y + r_b)^2 = r_b^2 \tag{5.77}$$

where:

$$r_b = \frac{\sqrt{r_h^2 \sin^2\delta + 2(1 - \cos\delta)(r_i^2 - r_h^2)} - r_\mathrm{h} \sin\delta}{2(1 - \cos\delta)} \tag{5.78}$$

Then the area becomes:

$$Ar_4 = \int_{y_A}^{y_F} f_4(y)dy \tag{5.79}$$

where:

$$f_4(y) = \sqrt{r_b^2 - (y + r_b)^2} + r_h \tag{5.80}$$

This can be analytically integrated between points A and F. So, now all the the elements to get $\mathrm{Ar}_{\mathrm{ABEF}}$ are available. So, the area becomes:

$$Ar_{\mathrm{ABEF}} = Ar_3 + Ar_4 - Ar_1 - Ar_2 \tag{5.81}$$

With this area, assuming axial symmetry, the total volume between the blades becomes:

$$V_b = Ar_{\text{ABEF}} * s_b \tag{5.82}$$

ϕ from CFD data

The dependence of ϕ on operating conditions can be written as:

$$\phi(F_{\text{P}_{\text{in}}}, F_\omega) \tag{5.83}$$

To get this, CFD data for the volume of air between the blades for operating conditions studied in this work (see Fig. 2.3) are used to get ϕ(F_{300},F_{1750}), ϕ(F_{300},F_{1450}), ϕ(F_{300},F_{1150}), ϕ(F_{600},F_{1750}) and ϕ(F_{75},F_{1750}). In Fig. 5.12, the values for ϕ for all eight points for the cases analyzed in the CFD study is given.

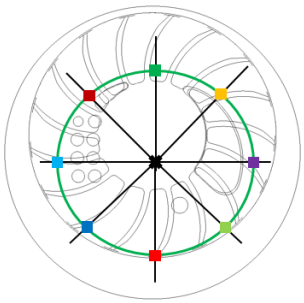

	$\varphi(F_{300}, F_{1750})$	$\varphi(F_{300}, F_{1450})$	$\varphi(F_{300}, F_{1150})$	$\varphi(F_{600}, F_{1750})$	$\varphi(F_{75}, F_{1750})$
φ_1	1.142	1.142	1.142	1.130	1.160
φ_2	1.030	1.030	1.030	1.020	1.020
φ_3	1.035	1.018	0.998	1.065	1.028
φ_4	1.200	1.205	1.210	1.200	1.200
φ_5	1.065	1.066	1.068	1.050	1.050
φ_6	1.030	1.010	0.990	1.012	1.025
φ_7	1.020	0.990	0.950	1.032	1.030
φ_8	1.125	1.135	1.150	1.135	1.112

Fig. 5.12. ϕ for eight points considered for cases analyzed in the CFD study

Through the values given in Fig. 5.12, following functions can be found:

$$\phi(F_{300}, F_\omega) \tag{5.84}$$

$$\phi(F_{\text{P}_{\text{in}}}, F_{1750}) \tag{5.85}$$

These function are of the following form:

$$\phi_{n1} = \phi(F_{300}, F_\omega) = 0.05487^2\ a_1 F_\omega^2 + 0.05487\ b_1 F_\omega + c_1 + 1 \tag{5.86}$$

$$\phi_{n2} = \phi(F_{P_{\text{in}}}, F_{1750}) = a_2 F_{P_{\text{in}}}^2 + b_2 F_{P_{\text{in}}} + c_2 + 1 \tag{5.87}$$

The coefficients (a_1,b_1,c_1) and (a_2,b_2,c_2) for all eight points are given in the Fig. 5.13.

φ_{n1}	a_1	b_1	c_1
φ_{11}	0	0	0.1420
φ_{21}	0	0	0.0300
φ_{31}	-1.5569	0.7624	-0.0486
φ_{41}	0.2359	-0.1622	0.2204
φ_{51}	0.2988	-0.1028	0.0738
φ_{61}	-0.9436	0.6487	-0.0516
φ_{71}	-3.9315	1.6763	-0.1498
φ_{81}	1.7298	-0.6760	0.1895

φ_{n2}	a_2	b_2	c_2
φ_{12}	0.0440	-0.0825	0.1677
φ_{22}	-0.0856	0.0760	0.0133
φ_{32}	0.0758	-0.0138	0.0286
φ_{42}	0	0	0.2000
φ_{52}	-0.1284	0.114	0.0400
φ_{62}	-0.0905	0.0615	0.0198
φ_{72}	0.0929	-0.0796	0.0370
φ_{82}	-0.0269	0.0572	0.1066

Fig. 5.13. Coefficients for Equations 5.86 and 5.87

Fig. 5.14 show the comparison of model and CFD data for volume of air between the blades for the cases studied. Maximum relative error for the fit was found to be within 10%. Fig. 5.15 liquid ring's inner surface curve calculated through the air volume fit respectively.

General Relations for ϕ

One approach to get the general relations for ϕ is to separate the effects of suction pressure and rotation speed which yields,

$$\phi(F_{\text{P}_{\text{in}}}, F_\omega) = \mathbf{g}(F_{\text{P}_{\text{in}}})\ \mathbf{h}(F_\omega) \tag{5.88}$$

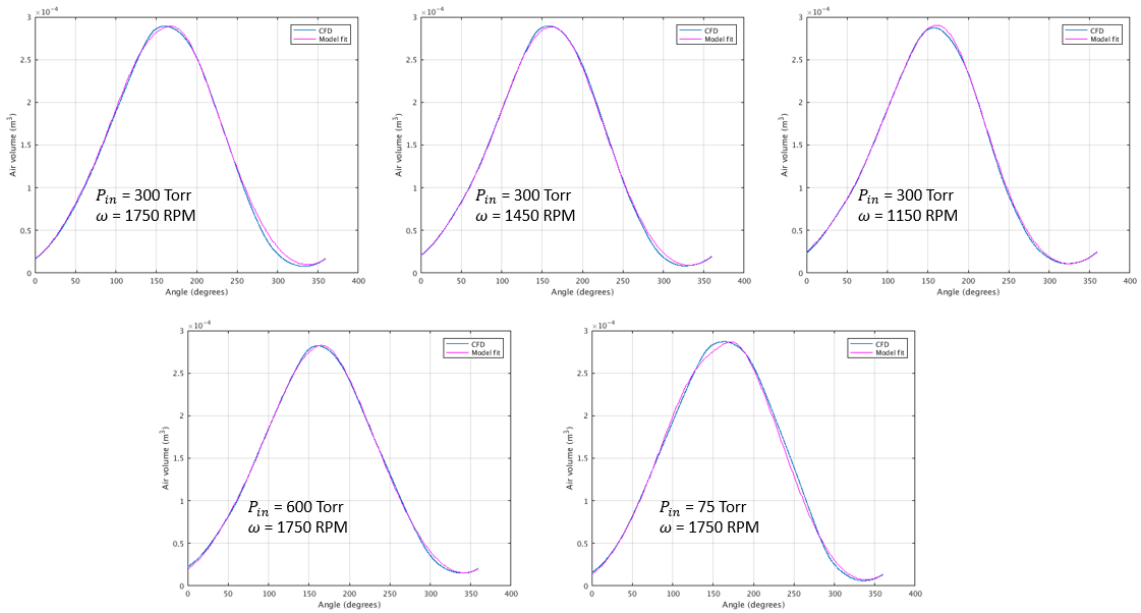

Fig. 5.14. Comparison of model and CFD for volume of air between the blades for the cases analyzed in the CFD study

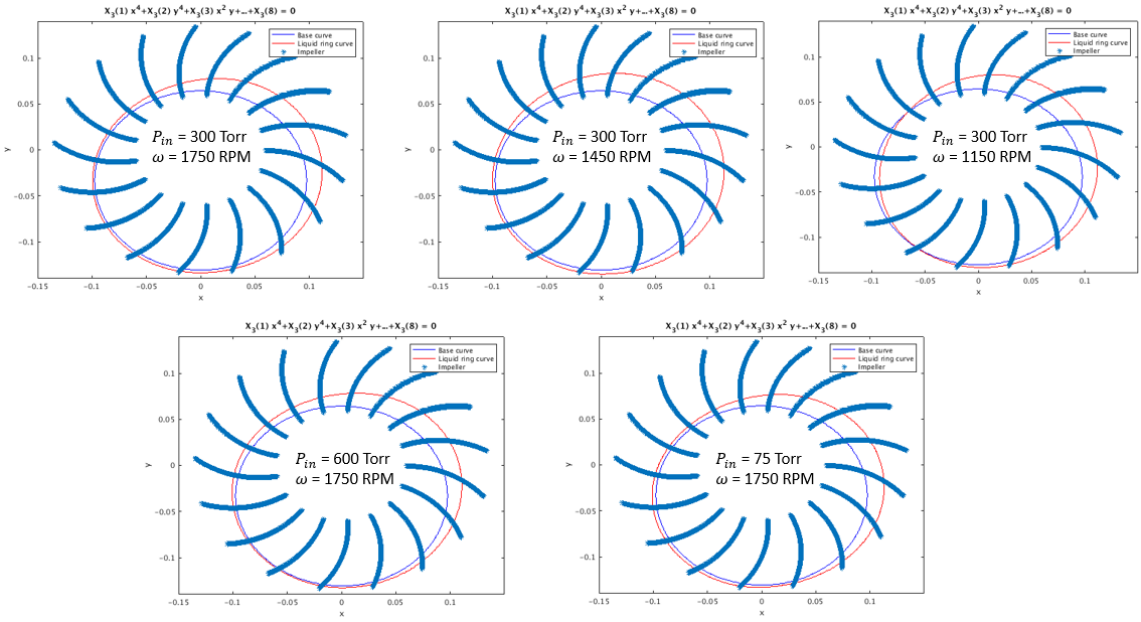

Fig. 5.15. Liquid ring's inner surface curve calculated through the air volume fit

Using this, $\boldsymbol{\phi}(\mathrm{F}_{300},\mathrm{F}_{\omega})$ and $\boldsymbol{\phi}(\mathrm{F}_{\mathrm{P_{in}}},\mathrm{F}_{1750})$ can be written as follows:

$$\boldsymbol{\phi}(F_{300}, F_{\omega}) = \mathbf{g}(F_{300})\ \mathbf{h}(F_{\omega}) \tag{5.89}$$

$$\boldsymbol{\phi}(F_{\mathrm{P_{in}}}, F_{1750}) = \mathbf{g}(F_{\mathrm{P_{in}}})\ \mathbf{h}(F_{1750}) \tag{5.90}$$

Multiplying Eq. (5.89) and (5.90) yields,

$$\boldsymbol{\phi}(F_{300}, F_{\omega})\ \boldsymbol{\phi}(F_{\mathrm{P_{in}}}, F_{1750}) = \mathbf{g}(F_{300})\ \mathbf{h}(F_{\omega})\ \mathbf{g}(F_{\mathrm{P_{in}}})\ \mathbf{h}(F_{1750}) \tag{5.91}$$

Rearranging yields,

$$\boldsymbol{\phi}(F_{300}, F_{\omega})\ \boldsymbol{\phi}(F_{\mathrm{P_{in}}}, F_{1750}) = \{\mathbf{g}(F_{\mathrm{P_{in}}})\ \mathbf{h}(F_{\omega})\}\{\mathbf{g}(F_{300})\ \mathbf{h}(F_{1750})\} \tag{5.92}$$

Using Eq. (5.88), Eq. (5.92) becomes:

$$\boldsymbol{\phi}(F_{300}, F_{\omega})\ \boldsymbol{\phi}(F_{\mathrm{P_{in}}}, F_{1750}) = \boldsymbol{\phi}(F_{\mathrm{P_{in}}}, F_{\omega})\ \boldsymbol{\phi}(F_{300}, F_{1750}) \tag{5.93}$$

Rearranging yields,

$$\boldsymbol{\phi}(F_{\mathrm{P_{in}}}, F_{\omega}) = \frac{\boldsymbol{\phi}(F_{300}, F_{\omega})\ \boldsymbol{\phi}(F_{\mathrm{P_{in}}}, F_{1750})}{\boldsymbol{\phi}(F_{300}, F_{1750})} \tag{5.94}$$

Equation (5.94) gives the relation between $\boldsymbol{\phi}(\mathrm{F}_{\mathrm{P_{in}}},\mathrm{F}_{\omega})$ and $\boldsymbol{\phi}(\mathrm{F}_{300},\mathrm{F}_{\omega})$ and $\boldsymbol{\phi}(\mathrm{F}_{\mathrm{P_{in}}},\mathrm{F}_{1750})$. $\boldsymbol{\phi}(\mathrm{F}_{300},\mathrm{F}_{\omega})$ and $\boldsymbol{\phi}(\mathrm{F}_{\mathrm{P_{in}}},\mathrm{F}_{1750})$ are given in Eq. (5.86) and (5.87). Using 5.94, general expressions for $\boldsymbol{\phi}(\mathrm{F}_{\mathrm{P_{in}}},\mathrm{F}_{\omega})$ at all eight points can be derived.

5.3.5 Air Pressure Calculation

Air Pressure from CFD data

To calculate the pressure from the fitted volume data, the revolution of the impeller section needs to be broken into processes that the air between the blades goes through (see Fig. 5.17). From $\theta = 90^{\mathrm{o}}$ to θ_{s}; suction process happens. From θ_{s} to

θ_c the air goes through a polytropic expansion process then a polytropic compression process with γ_1=1.2. From θ_c to θ_d discharge process happens from θ_d to θ_{st} the air goes through a polytropic expansion process with γ_2=1.1. From θ_{st} to 90° development of suction happens. The equation for the processes are given below:

$$90^o \leq \theta_n \leq \theta_s : P_a(\theta_n) = P_{in} \tag{5.95}$$

$$\theta_s \leq \theta_n \leq \theta_c : P_a(\theta_n) = P_a(\theta_{n-1})\left(\frac{V_a(\theta_{n-1})}{V_a(\theta_n)}\right)^{\gamma_1} \tag{5.96}$$

$$\theta_c \leq \theta_n \leq \theta_d : P_a(\theta_n) = P_a^h + \frac{1}{2}((1-\beta)a_1 + (1+\beta)a_2)(\theta_n - \theta_{ah})^2 \tag{5.97}$$

$$\beta = \frac{|\theta_n - \theta_{ah}|}{\theta_n - \theta_{ah}};\ a_1 = \frac{P_a(\theta_c) - P_a^h}{(\theta_c - \theta_{ah})^2};\ a_2 = \frac{P_a^d - P_a^h}{(\theta_{ah} - \theta_d)^2} \tag{5.98}$$

$$\theta_d \leq \theta_n \leq \theta_{st} : P_a(\theta_n) = P_a(\theta_{n-1})\left(\frac{V_a(\theta_{n-1})}{V_a(\theta_n)}\right)^{\gamma_2} \tag{5.99}$$

$$\theta_{st} \leq \theta_n \leq 90^o : P_a(\theta_n) = a_3(\theta_n - \theta_{st}) + P_a(\theta_{st}) \tag{5.100}$$

$$a_3 = \frac{P_{in} - P_a(\theta_{st})}{40^o};\ here,\ if\ P_a(\theta_n) \geq P_{in};\ P_a(\theta_n) = P_{in} \tag{5.101}$$

	$f(F_{300}, F_{1750})$	$f(F_{300}, F_{1450})$	$f(F_{300}, F_{1150})$	$f(F_{600}, F_{1750})$	$f(F_{75}, F_{1750})$
P_a^h/P_{out}	1.529	1.332	1.184	1.490	1.411
P_a^d/P_{out}	0.888	0.730	0.681	0.987	0.789
θ_c	255	255	242	228	300

Fig. 5.16. CFD values for the $P_a{}^h$ and $P_a{}^d$ for the cases analyzed in the CFD study

Here $P_a{}^h$ is the maximum air pressure during the revolution and $P_a{}^d$ is the air pressure after the end of discharge process. Since the present approach models the air pressure

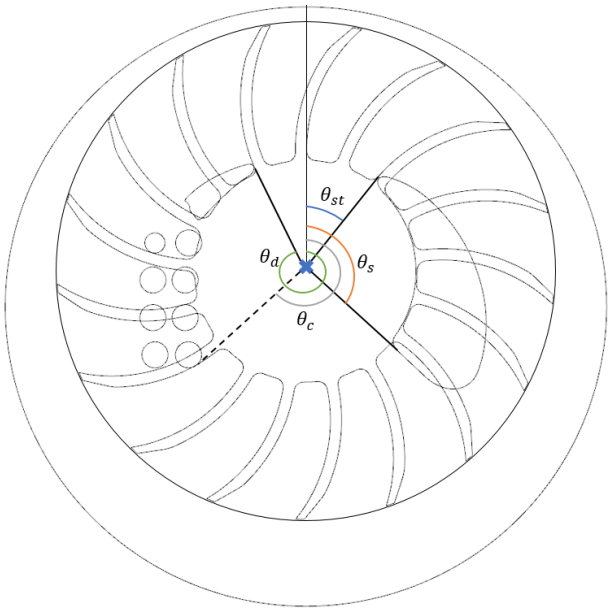

Fig. 5.17. Angles of interest for calculation of air pressure

during discharge process using $P_a{}^h$ and $P_a{}^d$, CFD data on $P_a{}^h$ and $P_a{}^d$ is required. Fig. 5.16 lists the CFD values for the $P_a{}^h$ and $P_a{}^d$ for the cases studied. With this information $P_a{}^h(F_{300},F_\omega)$, $P_a{}^h(F_{P_{in}},F_{1750})$ as well as $P_a{}^d(F_{300},F_\omega)$, $P_a{}^d(F_{P_{in}},F_{1750})$ can be derived and these function are of the following form:

$$P_a^h(F_{300}, F_\omega) = 0.05487^2\ a_1F_\omega^2 + 0.05487\ b_1F_\omega + c_1 \tag{5.102}$$

$$P_a^h(F_{P_{\text{in}}}, F_{1750}) = a_2F_{P_{\text{in}}}^2 + b_2F_{P_{\text{in}}} + c_2 \tag{5.103}$$

Similarly,

$$P_a^d(F_{300}, F_\omega) = 0.05487^2\ a_1F_\omega^2 + 0.05487\ b_1F_\omega + c_1 \tag{5.104}$$

$$P_a^d(F_{P_{\text{in}}}, F_{1750}) = a_2F_{P_{\text{in}}}^2 + b_2F_{P_{\text{in}}} + c_2 \tag{5.105}$$

The air pressure calculation has the capability to calculate θ_c based on the condition that the discharge ports open when pressure of air between becomes slightly higher than P_{out}. But for due to the discrete distribution of discharge ports, this condition couldn't be used to fit the CFD data since the discharge ports could open only at discrete angles. So, the CFD data for θ_c is used (see Fig. 5.16). Again, With this information $\theta_c(F_{300},F_\omega)$, $\theta_c(F_{P_{in}},F_{1750})$ can be derived and these functions are of the form:

$$\theta_c(F_{300}, F_\omega) = 0.05487^2\ a_1 F_\omega^2 + 0.05487\ b_1 F_\omega + c_1 \tag{5.106}$$

$$\theta_c(F_{P_{\text{in}}}, F_{1750}) = a_2 F_{P_{\text{in}}}^2 + b_2 F_{P_{\text{in}}} + c_2 \tag{5.107}$$

The coefficients (a_1,b_1,c_1) and (a_2,b_2,c_2) for all eight points are given in the Fig. 5.18. With this, the air pressure calculation becomes closed form.Fig. 5.19 show the comparison of calculated pressure with the CFD data.

	a_1	b_1	c_1
θ_c	0	138.06	142.12
P_a^h/P_{atm}	3.1040	2.9320	0.9586
P_a^d/P_{atm}	19.866	-2.5129	0.7591

	a_2	b_2	c_2
θ_c	116.13	-205.92	228.19
P_a^h/P_{atm}	-0.7239	0.7572	1.3436
P_a^d/P_{atm}	-0.1206	0.3929	0.7519

Fig. 5.18. Coefficients for Equations 6.104 and 6.105

General Relations for P_a^h, P_a^d and θ_c

To get general relations for P_a^h, P_a^d and θ_c, the hypothesis employed in deriving general relations for ϕ. Using the hypothesis:

$$P_a^h(F_{P_{\text{in}}}, F_\omega) = \frac{P_a^h(F_{300}, F_\omega)\ P_a^h(F_{P_{\text{in}}}, F_{1750})}{P_a^h(F_{300}, F_{1750})} \tag{5.108}$$

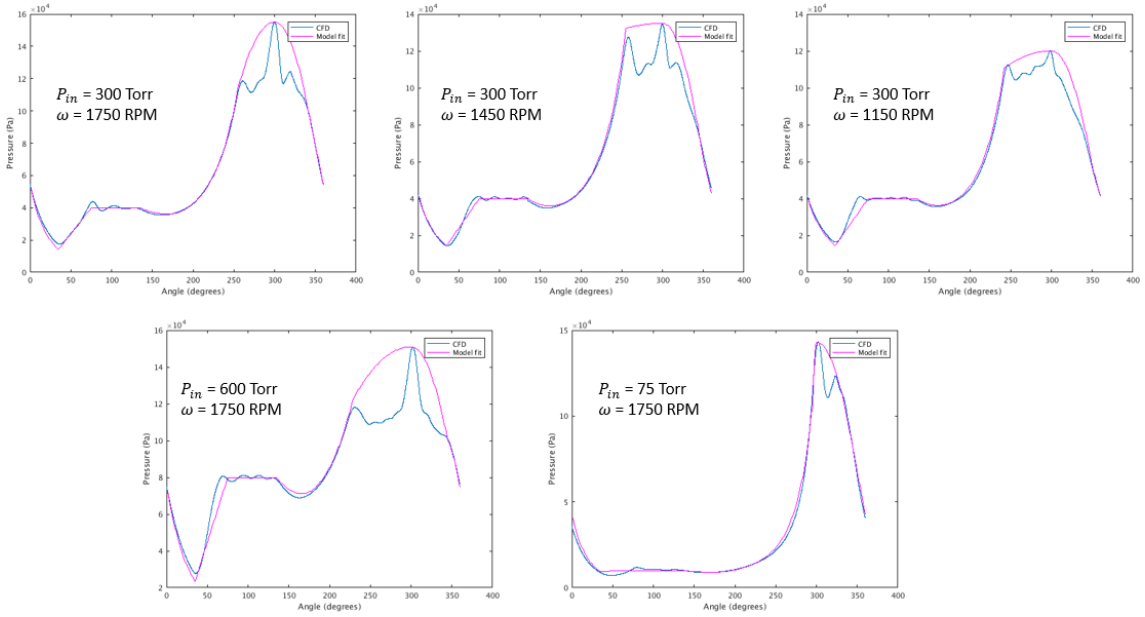

Fig. 5.19. Comparison of model and CFD for pressure of air between the blades for the cases analyzed in the CFD study

Similarly,

$$P_a^d(F_{\mathrm{P_{in}}}, F_\omega) = \frac{P_a^d(F_{300}, F_\omega)\ P_a^d(F_{\mathrm{P_{in}}}, F_{1750})}{P_a^d(F_{300}, F_{1750})} \tag{5.109}$$

Similarly,

$$\theta_c(F_{\mathrm{P_{in}}}, F_\omega) = \frac{\theta_c(F_{300}, F_\omega)\ \theta_c(F_{\mathrm{P_{in}}}, F_{1750})}{\theta_c(F_{300}, F_{1750})} \tag{5.110}$$

5.3.6 Water Flow in the Ring

The pump geometry with the liquid ring is is given in Fig. 5.20. The location A consists of two regions as far as velocity profiles are concerned. One inside the impeller region which is small (region 2) and another outside the impeller region (region 1). In region 1, CFD suggests approximate linear velocity profiles (see Fig. 5.21 and 5.22). Using this, the velocity profile in region 1 can be written as:

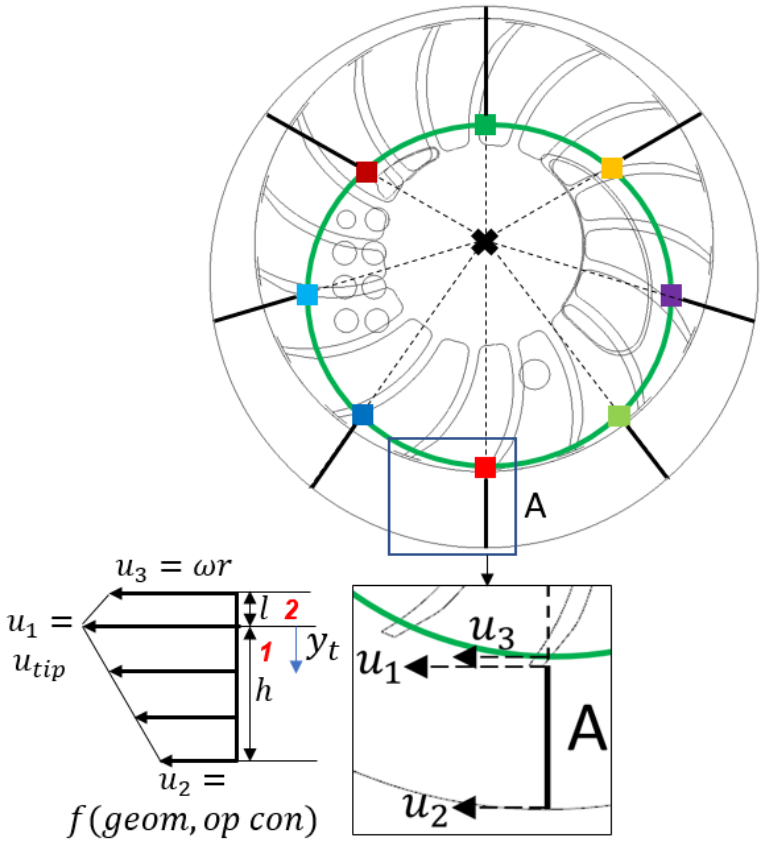

Fig. 5.20. Region of interest (location A) for calculation of volume flow rate of water in the liquid ring

$$u = \frac{u_2 - u_1}{h} y_t + u_1 \tag{5.111}$$

So the volume flow rate through an infinitesimal area is:

$$dQ_{w1} = s_b\ u\ dy_t = s_b \Big(\frac{u_2 - u_1}{h} y_t + u_1 \Big) dy_t \tag{5.112}$$

So the total flow rate in the region 1 is:

$$Q_{w1} = \int dQ_{w1} = \int_0^h s_b \Big(\frac{u_2 - u_1}{h} y_t + u_1 \Big) dy_t = \frac{1}{2}(u_1 + u_2) s_b h \tag{5.113}$$

In region 2:

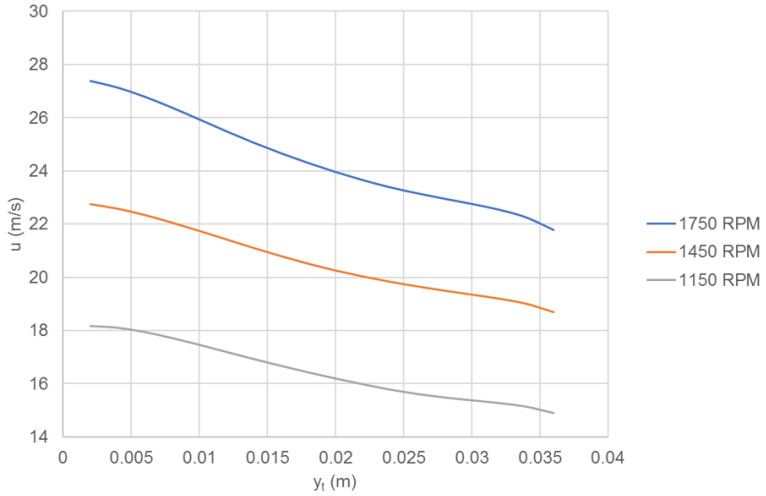

Fig. 5.21. Velocity profile in region 1 for the cases with varying impeller rotational speed analyzed in CFD study

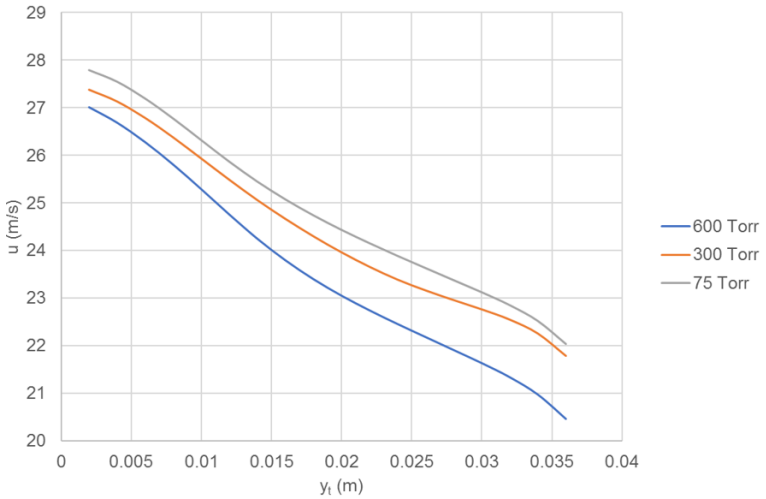

Fig. 5.22. Velocity profile in region 1 for the cases with varying suction pressure analyzed in CFD study

$$u = \frac{u_1 - u_3}{l} y_t + u_1 \tag{5.114}$$

So the volume flow rate through an infinitesimal area is:

$$dQ_{w2} = s_b \; u \; dy_t = s_b\Big(\frac{u_1 - u_3}{l} y_t + u_1\Big) dy_t \tag{5.115}$$

So the total flow rate in the region 1 is:

$$Q_{w2} = \int dQ_{w2} = \int_{-l}^{0} s_b\Big(\frac{u_1 - u_3}{l} y_t + u_1\Big) dy_t = \frac{1}{2}(u_1 + u_3) s_b l \tag{5.116}$$

So the total volume flow rate of water becomes:

$$Q_w = Q_{w1} + Q_{w2} = \frac{1}{2}(u_1 + u_2) s_b h + \frac{1}{2}(u_1 + u_3) s_b l \tag{5.117}$$

It can be noted that u_2 is needed to define the volume flow rate. u_2 is modelled through CFD data at the same location. The modelling of u_2 is again broken up into two parts: 1. contribution from geometry 2. contribution from operating conditions.

$$\frac{u_2}{u_{tip}} = \psi * \epsilon \tag{5.118}$$

where ψ is the contribution from geometry and ϵ is the contribution form operating conditions. The equations for ψ and ϵ are as follows:

$$\epsilon = a_3 F_\omega^2 + b_3 F_\omega + c_3 \tag{5.119}$$

where,

$$a_3 = -5.8972; \; b_3 = 2.5145; \; c_3 = 0.6103 \tag{5.120}$$

$$\psi = a_4 \lambda^3 + b_4 \lambda^2 + c_3 \lambda + d_4 \tag{5.121}$$

where,

$$\lambda = \frac{r_i - r_h}{r_{oc} - r_i + e_y}\Big(\frac{r_i - r_h}{r_{oc}}\Big)^2 \tag{5.122}$$

$$a_4 = 183.34; \; b_4 = -163.13; \; c_4 = 47.758; \; d_4 = 3.6354 \tag{5.123}$$

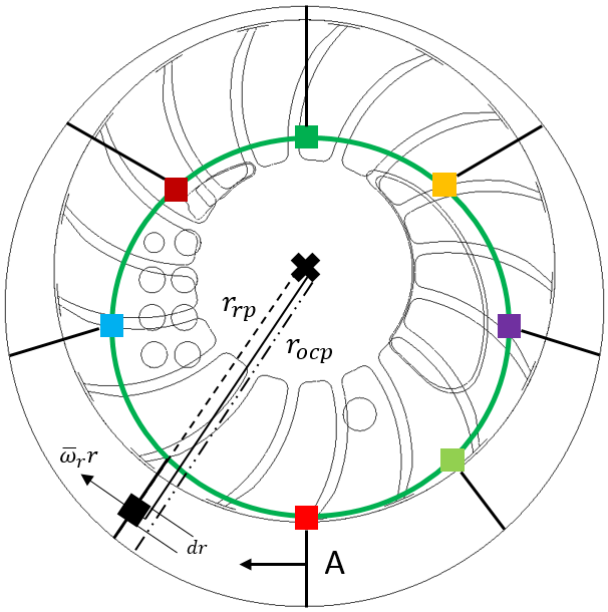

Fig. 5.23. Schematic for calculation of rotational speed distribution in the liquid ring

5.3.7 Rotational Speed Distribution in the Ring

In the previous section the total volume flow rate of water in the ring was calculated. This will be used to calculate the rotational speed distribution in the ring. In the Fig. 5.23 at a certain angular position, at a radial distance r, an element in the liquid part of the ring was chosen. This element has a thickness of dr and velocity of ωr. So the volume flow through this element is:

$$dQ_{ws} = s_b \; \omega_r(r, \theta) \; r \; dr \tag{5.124}$$

So the total volume flow at this angular position will be:

$$Q_{ws} = \int dQ_{ws} = \int_{r_{rp}}^{r_{ocp}} s_b \; \omega_r(r, \theta) \; r \; dr \tag{5.125}$$

At this angular position, the radial position of the ring is r_{rp} and radial position of the casing is r_{ocp}. For the purposes of this analysis, an average ω along the radial direction for all the angular positions will be calculated:

$$\omega_r(r,\theta) = \omega_r(\theta) = \overline{\omega}_r \tag{5.126}$$

Putting, the equation for total flow becomes:

$$Q_{ws} = \int_{r_{rp}}^{r_{ocp}} s_b\ \omega_r(r,\theta) r dr = \int_{r_{rp}}^{r_{ocp}} s_b\ \overline{\omega}_r r dr \tag{5.127}$$

After integrating the total flow is given as:

$$Q_{ws} = \int_{r_{rp}}^{r_{ocp}} s_b\ \overline{\omega}_r r dr = s_b\ \overline{\omega}_r \int_{r_{rp}}^{r_{ocp}} r dr = \frac{1}{2} s_b\ \overline{\omega}_r (r_{ocp}^2 - r_{rp}^2) \tag{5.128}$$

Now, mass conservation in the azimuthal direction is applied. The total flow at location A was calculated in the previous section. The volume flow at location A and for any location should be equal for mass conservation to hold. Applying, the equation becomes:

$$Q_w = Q_{ws} = \frac{1}{2} s_b\ \overline{\omega}_r (r_{ocp}^2 - r_{rp}^2) \tag{5.129}$$

So the final expression for omega becomes:

$$\overline{\omega}_r = \frac{2Q_w}{s_b (r_{ocp}^2 - r_{rp}^2)} \tag{5.130}$$

5.3.8 Pressure Distribution in the Ring

In the previous section, the rotational speed distribution for the ring was found. Now, we need to find the pressure distribution in the ring. To do that, solid body rotation theory is employed. According to the theory, the radial pressure variation for a given ω at particular radial (r) location and for a given fluid is given as:

$$\frac{dP_r}{dr} = \rho \overline{\omega}_r^2 r \tag{5.131}$$

To calculate the pressure variation the above relation needs to be integrated. Rearranging, we get:

$$dP_r = \rho\overline{\omega}_r^2 r dr \tag{5.132}$$

Integrating both sides with appropriate limits:

$$\int_{P_{r1}}^{P_r} dP_r = \int_{r_1}^{r} \rho\overline{\omega}_r^2 r dr \tag{5.133}$$

So the equation becomes:

$$P_r = P_{r_1} + \frac{1}{2}\rho\overline{\omega}_r^2(r^2 - r_1^2) \tag{5.134}$$

In the air region with appropriate P_{r_1} and r_1 we have:

$$P_r = P_a + \frac{1}{2}\rho_a\omega^2(r^2 - r_h^2) \tag{5.135}$$

In the water region with appropriate P_{r_1} and r_1 we have:

$$P_r = P_a + \frac{1}{2}\rho_a\omega^2(r_{rp}^2 - r_h^2) + \frac{1}{2}\rho_w\overline{\omega}_r^2(r^2 - r_{rp}^2) \tag{5.136}$$

5.3.9 Pressure on a Blade Element

In the previous section, rotational speed distribution and pressure distribution in the ring was calculated. With this information, the pressure distribution on the blades can be calculated. To proceed, the impeller blades are broken into small elements and the flow around the blades is observed through the frame of the elements. In the air region, since the air is trapped between the blades, the relative velocity of air with respect to blades is almost zero in the azimuthal direction. So the pressure on the approaching side of the blade in the air region becomes:

$$P_i = P_r^c \tag{5.137}$$

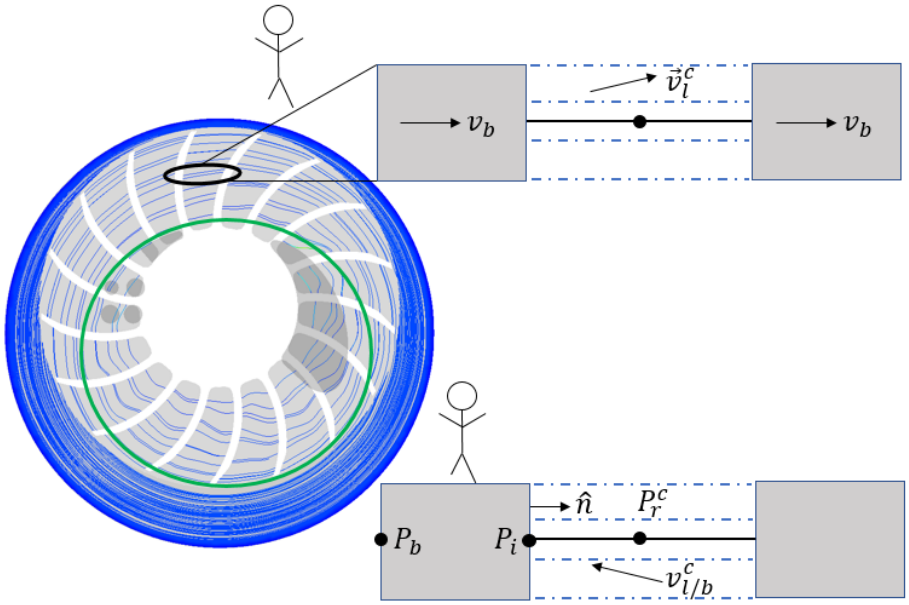

Fig. 5.24. Schematic for pressures P_i and P_b

For the water region, Fig. 5.24 shows the velocity vector of the blade element and liquid around it from an inertial reference frame. Figure shows the velocity vector of the blade element and liquid around it from an non-inertial reference frame. The relative velocity $v_{l/b}$ can calculated as:

$$\vec{v}_{l/b}^c = \vec{v}_l^c - \vec{v}_b = (\vec{\omega}_r - \vec{\omega}) \times \vec{r} \tag{5.138}$$

To get the pressure on the blade element, the normal component of the relative velocity is required, which can be calculated as:

$$\vec{v}_{nl/b}^c = \vec{v}_{l/b}^c \cdot \hat{n} \tag{5.139}$$

And pressure on the approaching side in the water region, using the Bernoulli's equation along the black line between the elements in Fig. 5.24, becomes:

$$P_i = P_r^c + \frac{1}{2}\rho_w {v_{nl/b}^c}^2 \tag{5.140}$$

The pressure on the trailing side is calculated as follows:

$$P_b = P_r^b \tag{5.141}$$

5.4 Performance and Validation of the Model

The experimental data from configuration 1 [25], 2 [20], 3, 4 and 5 [24] has been used to evaluate the performance of reduced order model developed. Fig. 5.25-5.29 describe comparison of rate of air ingested by the pump predicted by the model developed and those measured by the experiments. It can be seen that the rate of air ingested by the pump can be predicted with maximum relative errors less than 12%. Fig. 5.30-5.34 describe comparison of torque predicted by the model developed and those measured by the experiments. It can be seen that the torque can be predicted with maximum relative errors less than 17%. It should be noted that the model developed demonstrates generality since the configurations 1, 2, 3, 4 and 5 are significantly different from each other.

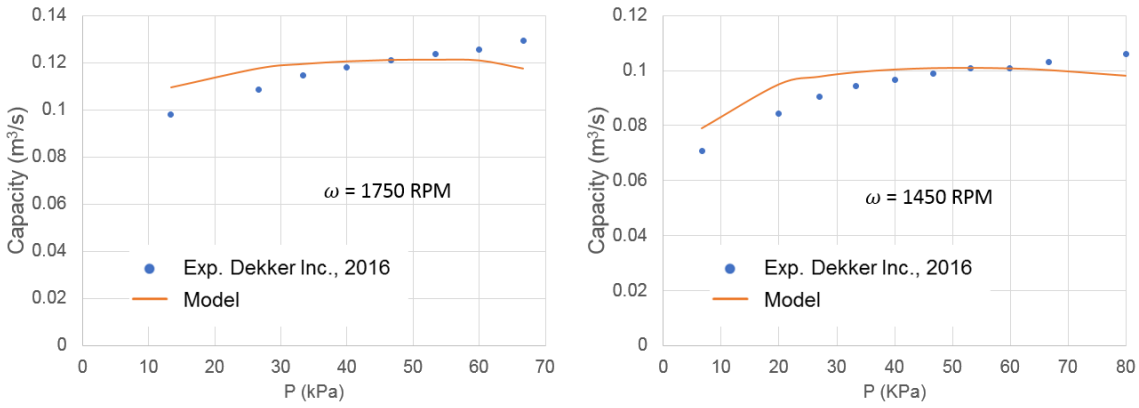

Fig. 5.25. Rate of air ingested by the pump comparison between model and experiments for configuration 1

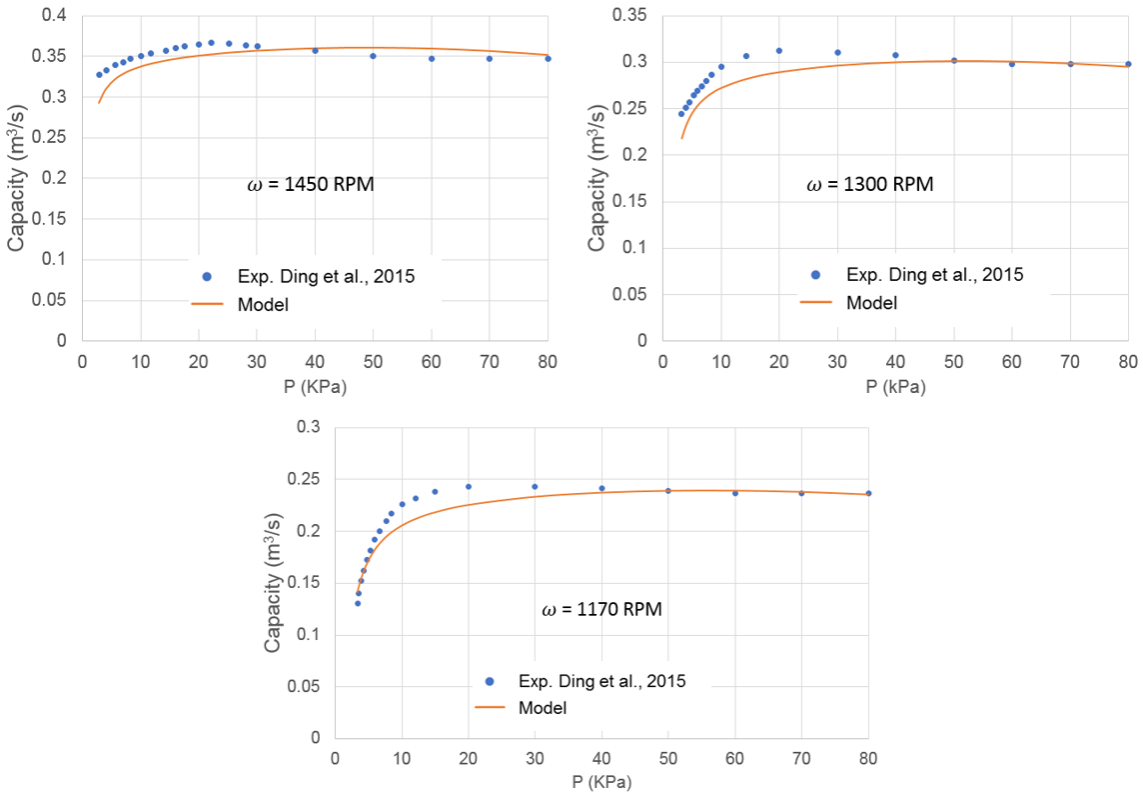

Fig. 5.26. Rate of air ingested by the pump comparison between model and experiments for configuration 2

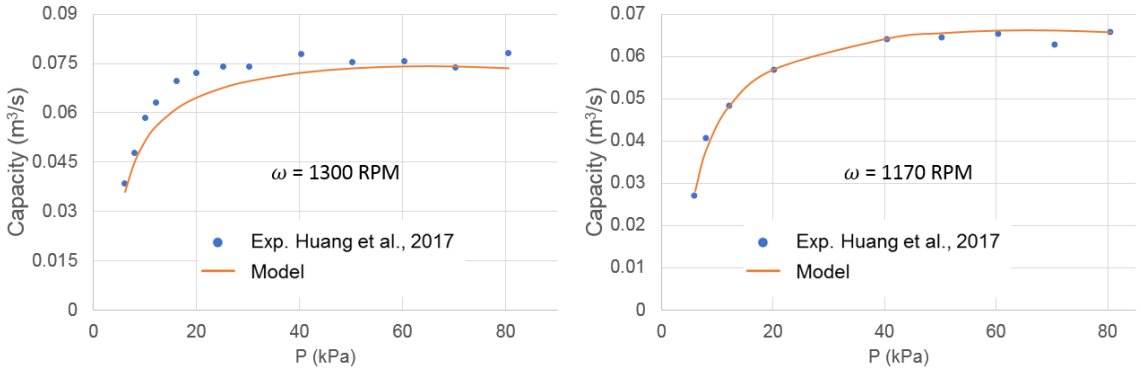

Fig. 5.27. Rate of air ingested by the pump comparison between model and experiments for configuration 3

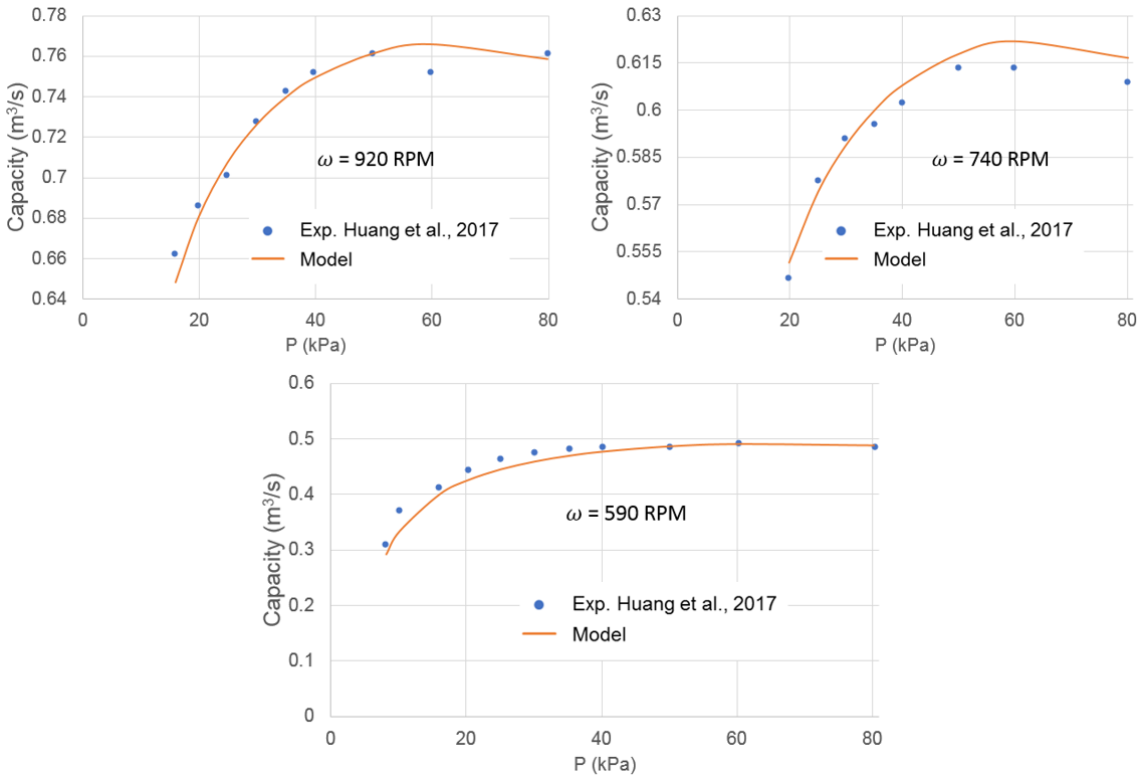

Fig. 5.28. Rate of air ingested by the pump comparison between model and experiments for configuration 4

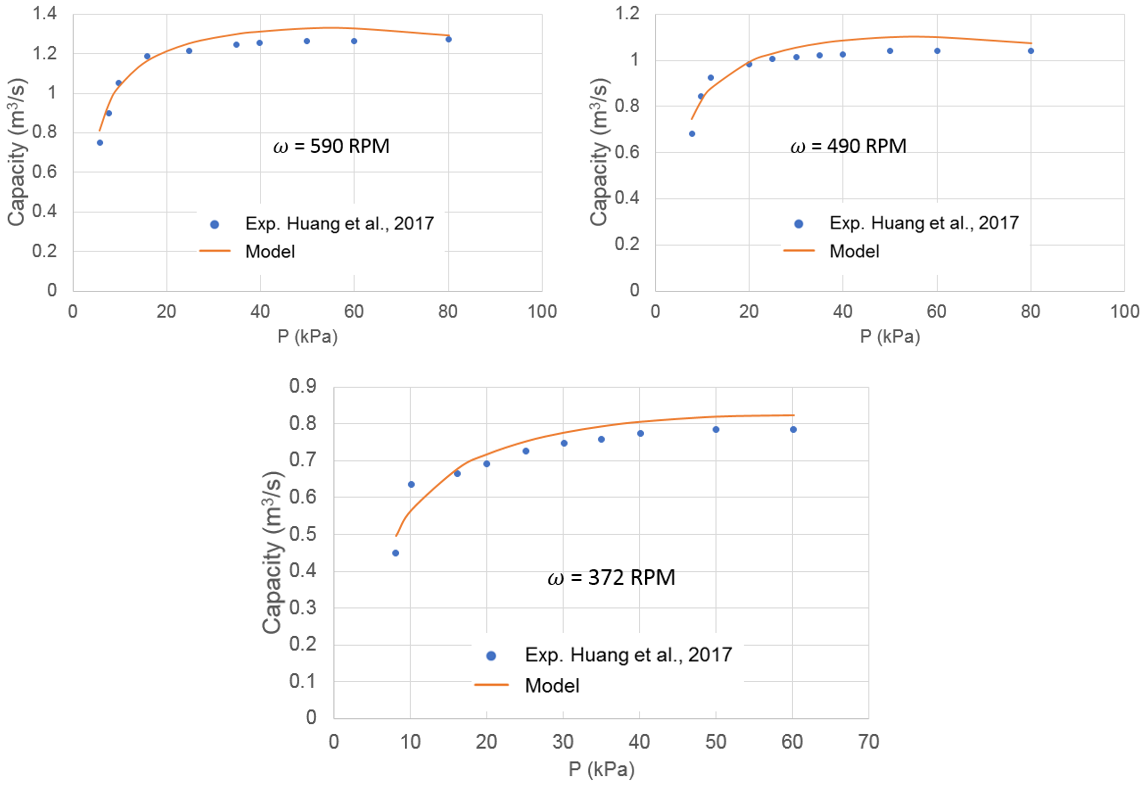

Fig. 5.29. Rate of air ingested by the pump comparison between model and experiments for configuration 5

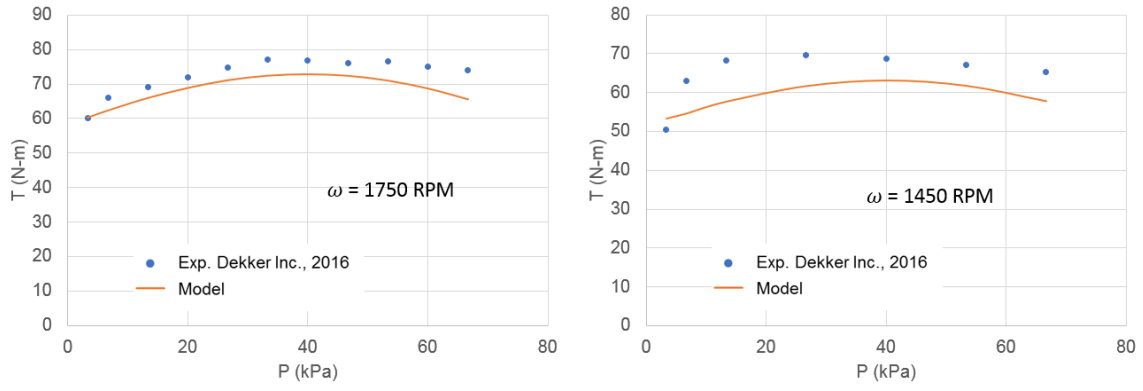

Fig. 5.30. Torque comparison between model and experiments for configuration 1

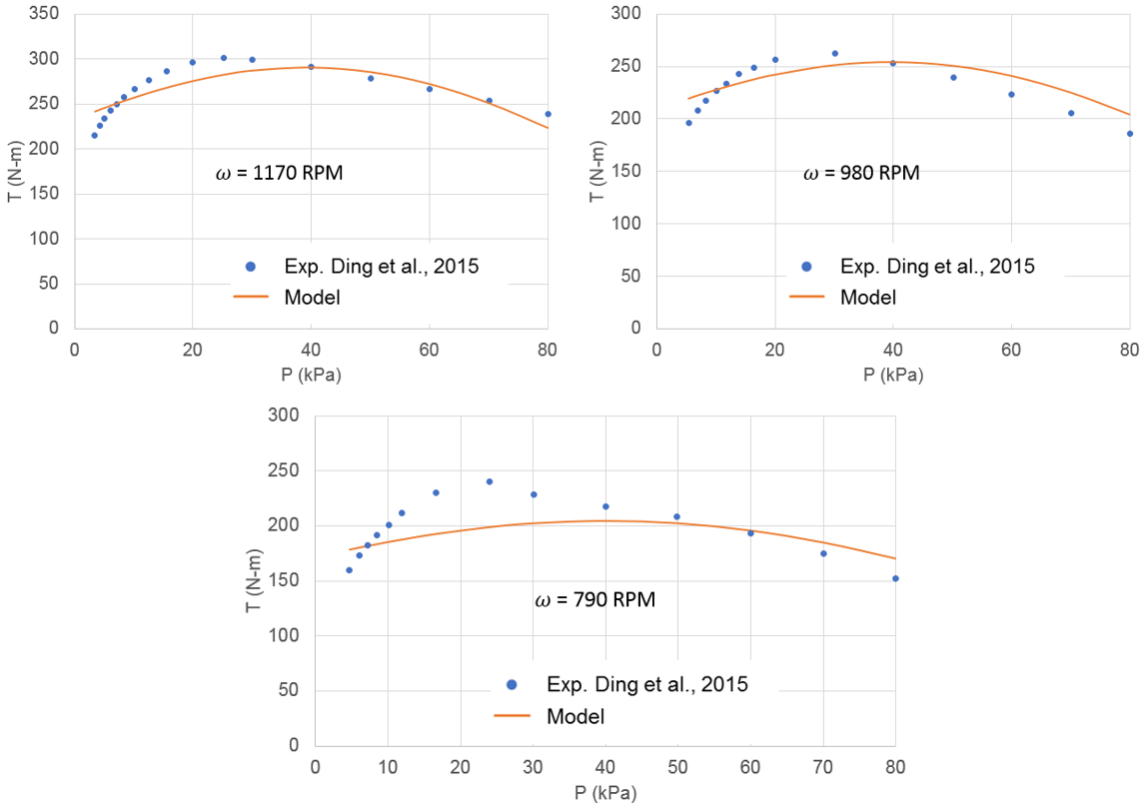

Fig. 5.31. Torque comparison between model and experiments for configuration 2

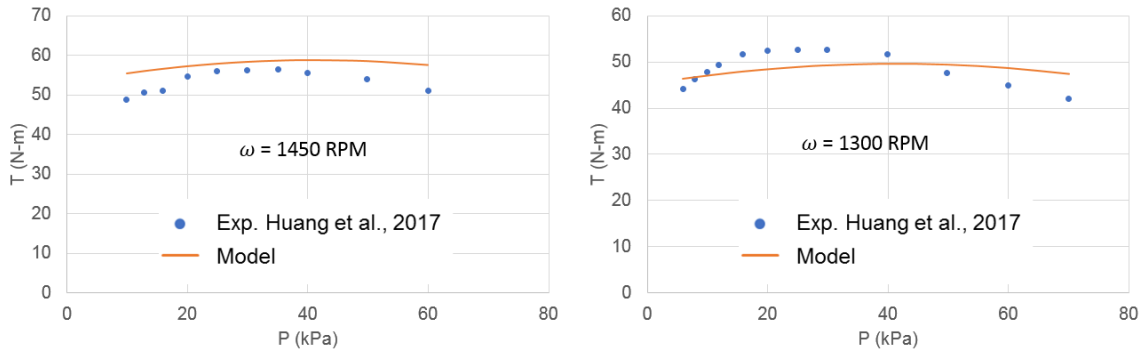

Fig. 5.32. Torque comparison between model and experiments for configuration 3

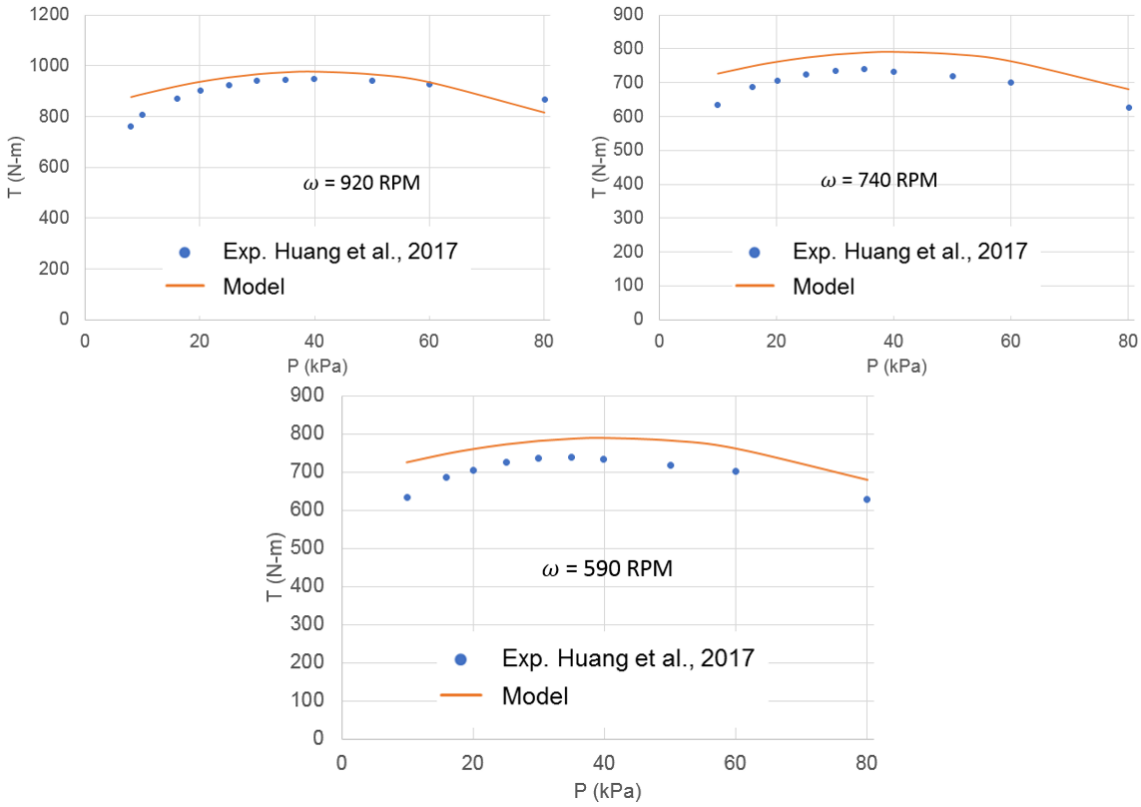

Fig. 5.33. Torque comparison between model and experiments for configuration 4

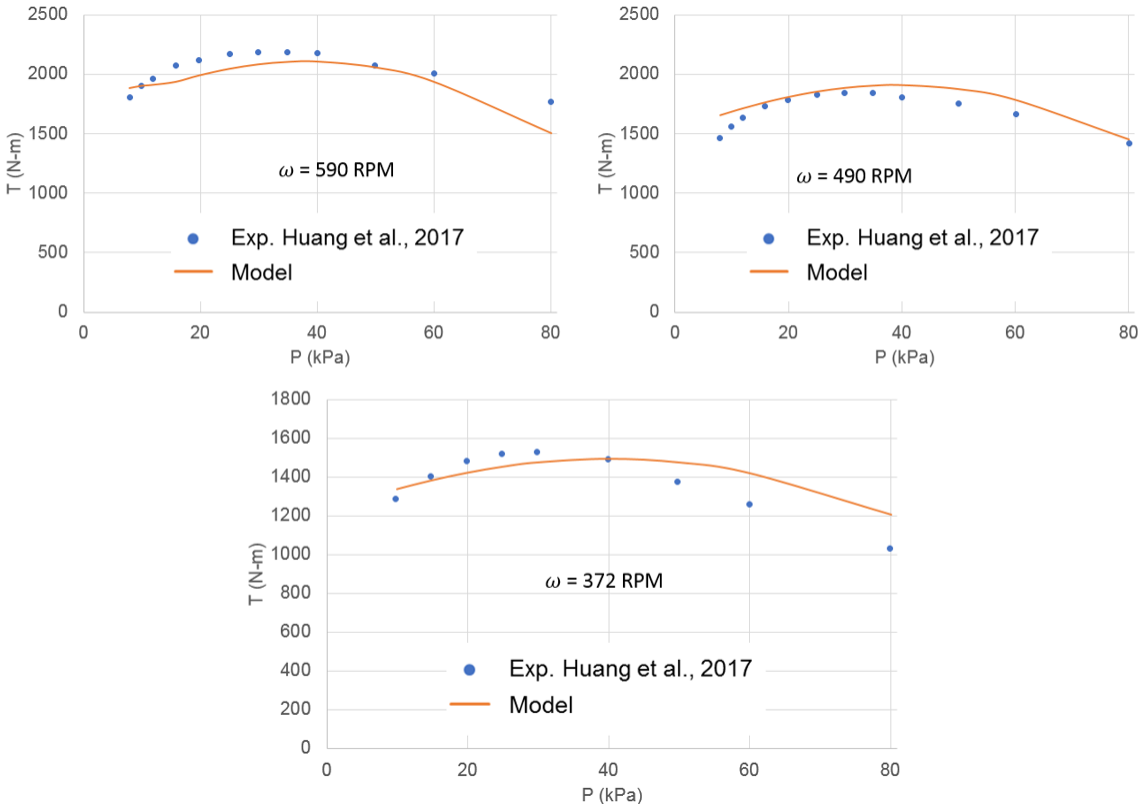

Fig. 5.34. Torque comparison between model and experiments for configuration 5

6. SUMMARY

Vacuum is needed in many applications, and there are many types of pumps that can provide the vacuum levels needed. One widely used pump is the liquid-ring vacuum pump, which does not involve any solid-solid contacts at interfaces where moving and stationary parts meet. Though liquid-ring vacuum pumps are efficient and robust, manufacturers have aggressive goals on improving efficiency, performance, and range of operations. In this research, time-accurate, three-dimensional CFD that resolve the air-water interface were performed to study the nature of the flow in a liquid-ring vacuum pump. This study showed how the suction pressure, discharge pressure, rotational speed and eccentricity of the impeller, and the location of the discharge and suction ports affect the formation and the shape of the liquid ring which in turn enables the suction process to create a vacuum. This study also showed that if the suction pressure is below some critical value, then two adverse effects can occur. During the suction process, a portion of the process has discharge instead of suction. Similarly, during the discharge process, a portion of the process has suction instead of discharge. These adverse effects can be removed by shifting the location of the suction and discharge ports. It can also be eliminated by decreasing the rotational speed of the impeller. This is because for a given pump design, the compression and expansion ratios that enables suction and discharge are increased by decreasing the rotational speed of the impeller.

The CFD study conducted also showed that the shape of the liquid ring decides how much gas the pump can ingest since that shape was found to play a dominant role in creating the expansion ratio or the vacuum needed to draw gas into the pump through the suction port and the compression ratio needed to expel the gas through the discharge ports. In addition, the CFD study showed that the shape of the liquid ring decides on the power consumption since that shape is in direct correlation with

the amount of liquid the impeller has to rotate inside the pump chamber and the resistance offered by the liquid to the impeller in its rotation is a predominant source of power consumption in a liquid ring vacuum pump. With this knowledge, a physics based reduced order model was developed to predict air ingested and power consumed by the pump as a function of design (impeller radius, hub radius, casing radius, eccentricity, blade span, blade angle, blade thickness, number of blades) and operating (suction pressure, rotational speed of the impeller) parameters. This model was developed by recognising and demonstrating that the amount of air ingested and power consumed by the pump is strongly dependent on the shape and location of the liquid ring surface. Results obtained for the flow rate of the gas drawn through the suction port by the pump were compared with experimentally measured values, and a reasonable match was found with relative error less than 12%. Results obtained for the power consumed by the pump were compared with experimentally measured values, and a reasonable match was found with relative error less than 17%. The model predicts pressure of air between the blades as a function of rotor angle which in turn can predict the location of first discharge port open. The model also predicts pressure of water as a function of radial and angular position in the pump which in turn can predict the location and magnitude of maximum pressure on the housing.

REFERENCES

REFERENCES

[1] S. Hashemi, R. Crotogino, and W. Douglas, *Effect of Papermaking Parameters on through Drying of Semi-Permeable Paper.* Drying technology, 15(2), 1997.

[2] L. Rey and J. May, *Freeze-Drying/Lyophilization Of Pharmaceutical and Biological Products.* CRC Press, 2004.

[3] Y. Ying and J. Qiuzhou, *Progress of Moulding Technology of Resin-matrix Composite/foam Plastic Sandwich[J].* Aerospace Materials and Technology, 1, 2004.

[4] S. Namba, *Ion implantation in Semiconductor Processing.* Nuclear Instruments and Methods in Physics Research, 189(1), pp. 175, 1981.

[5] M. Madou, *Manufacturing Techniques for Microfabrication and Nanotechnology.* CRC press, 2011.

[6] D. Baldwin and G. Rowe, *Lubrication at High Temperatures With Vapor-Deposited Surface Coatings.* Journal of Basic Engineering, 83(2), pp. 133, 1961.

[7] E. V. Halle, H. W. III, and R. Lowry, *The effect of vacuum core boundary conditions on separation in the gas centrifuge.* Nuclear Technology, 62(3), pp. 325, 1983.

[8] M. Havet and F. Hennequin, *Experimental characterization of the ambience in a food-processing clean room.* Journal of food engineering, 39(3), pp. 329, 1999.

[9] H. Behnsen, *Underground repositories for chemically toxic waste in German salt and potash mines.* Reviews in Engineering Geology, 29, pp. 31, 2008.

[10] S. Hong and G. Son, *Numerical study of a vane vacuum pump with two-phase flows.* Journal of Mechanical Science and Technology, 31(7), pp. 3329, 2017.

[11] R. Harris, K. Edge, and D. Tilley, *The suction dynamics of positive displacement axial piston pumps.* Journal of dynamic systems, measurement, and control, 116(2), pp. 281, 1994.

[12] A. Kovacevic, N. Stosic, E. Mujic, and I. Smith, *CFD integrated design of screw compressors.* Engineering Applications of Computational Fluid Mechanics, 1(2), pp. 96, 2007.

[13] J. Wang, J. McDonough, and D. Zhang, *Analysis and numerical simulation of a novel gasliquid multiphase scroll pump.* Journal of Heat and Mass Transfer, 91, pp. 27, 2015.

[14] M. Cui, *Numerical study of unsteady flows in a scroll compressor.* Journal of fluids engineering, 128(5), pp. 947, 2006.

[15] I. Grunow, U. Salecker, P. Bartsch, and T. Grohmann, *Analysis of Cavitating Flow in a Liquid Ring Vacuum Pump.* Technical Study by CFX-Berlin, 2011.

[16] K. Kakuda, Y. Ushiyama, S. Obara, J. Toyotani, S. Matsuda, H. Tanaka, and K. Katagiri, *Flow Simulations in a Liquid Ring Pump using a Particle Method.* Reading Massachusetts: Computer Modeling in Engineering and Sciences 66, 215, 2010.

[17] M. Radle and B. Shome, *Cavitation Prediction in Liquid Ring Pump for Aircraft Fuel Systems by CFD Approach.* SAE Technical Paper, 2013-01-2238, 2013.

[18] S. Huang, Z. Y. Ruan, Q. Deng, T. Z. Wu, and Z. H. Tan, *Numerical Analysis of Gas-Liquid Two-Phase Flow in Liquid Ring Vacuum Pump.* Vacuum 2, 26, 2009.

[19] J. Guan and S. Huang, *Property Analysis of the Two-Phase Flow of Liquid-Ring Vacuum Pumps Based on Computational Fluid Dynamics (CFD).* Chemical Engineering and Machinery 6, 21, 2010.

[20] H. Ding, Y. Jiang, H. Wu, and J. Wang, *Two Phase Flow Simulation of Water Ring Vacuum Pump Using VOF Model.* ASME/JSME/KSME 2015 Joint Fluids Engineering Conference, V001T33A019-V001T33A019, 2015.

[21] F. R. Menter, M. Kuntz, and R. Langtry, *Ten Years of Industrial Experience with the SST Turbulence Model.* Turbulence, Heat and Mass Transfer 4, 625, 2003.

[22] C. Hirt and B. Nichols, *Volume of fluid (VOF) method for the dynamics of free boundaries.* Journal of computational physics, 39(1), pp. 201., 1981.

[23] I. Pardeshi, A. Pandey, and T. I. Shih, *A Reduced-Order Model for Predicting the Performance of a Liquid-Ring Vacuum Pump.* ASME 2018 International Mechanical Engineering Congress and Exposition, 2018.

[24] H. Si, J. He, X. Wang, and G. Qiu, *Theoretical Model for the Performance of Liquid Ring Pump Based on the Actual Operating Cycle.* International Journal of Rotating Machinery 2017, 2017.

[25] D. V. T. Inc., *Experimental Studies on DV0300B-KA Liquid Ring Vacuum Pump.* Personal Communication, 2015.